

## Abstract

Numerous pathologies including tumor metastasis, diabetic retinopathy, age-related macular degeneration and edema are induced or exacerbated by malfunction and aberrant growth of blood or lymphatic vessels. Therefore, attempts in medical and pharmacological researches have been made to treat these disorders by modulating formation and function of blood and lymphatic vessels, which necessarily requires cell-culture-based *in vitro* models. The microenvironments of endothelial cells are constructed by integration of key constituents such as multiple cell types in close interactions, 3-dimensional extracellular matrix (ECM), biochemical cues and flow-induced mechanical stresses. These factors not only modulate formation of blood/lymphatic vessels, but also influence characteristic functions and homeostasis. However, current *in vitro* models of blood/lymphatic vessels usually do not integrate these key elements in a single platform or lack precise spatiotemporal control over relevant parameters, thus cellular behaviors observed in these systems only provide limited information and predictions of *in vivo* phenomena.

In this thesis, we present a novel *in vitro* model which provides close reconstitution of complex cellular dynamics observed during processes of *in vivo* angiogenesis and lymphangiogenesis by integrating important elements of endothelial microenvironments including endothelial-stromal cell interactions, cell-ECM interactions, biochemical and mechanical stimulants in controlled 3D cell culture environments. For development of blood vessel and angiogenesis model, we used surface-tension-assisted cell and ECM patterning technique to precisely control relative location and distribution of endothelial and fibroblast cell types so that paracrine interactions between these two cell types

induce endothelial cells to undergo natural programs of vessel morphogenesis, vasculogenesis and angiogenesis in our chip. One of major attributes of our model is that endothelial cells forming vascular networks spontaneously established perfusable accesses into the lumens allowing introduction of fluid flow through the vasculatures, which overcomes the technical hurdle that suffered by conventional models of blood vessel usually lacking either one of two essential factors, cell-autonomously established 3D vasculatures and flow-induced mechanical shear stress. The resulting vascular networks exhibited close resemblance of *in vivo* capillary networks in biochemical marker expression and structural aspects, as well as fluid-flow induced endothelial specific morphologies and characteristic functions.

Next, we demonstrated that the developed system can provide novel experimental opportunities in the investigation of lymphangiogenesis, new lymphatic vessel formation via sprouting morphogenesis from pre-existing lymphatics. Of particular note, this model is optimally suited for co-stimulation of biochemical and mechanical stimuli, both of which are proven to be important for lymphatic morphogenesis in our chip. While static condition, where lymphatic endothelial cells are exposed to increasing concentration gradients of pro-lymphangiogenic factors, induced lymphatic sprouts in 3D fibrin matrix, combination of these factors and interstitial flow with direction reminiscent of lymph flow, significantly promoted lymphatic sprouting with direction against the fluid flow. Not only presence of interstitial flow, but also magnitudes and directions of interstitial flow resulted in sensitive responses of LECs toward these mechanical stimuli. The condition most actively promoted lymphatic sprouting corresponds to the tumor microenvironments where characterized by overexpression of

plethora of cytokines and growth factors and elevated lymph flow, explaining how these altered microenvironments exacerbate peritumor lymphangiogenesis and metastatic dissemination of tumor cells through lymph nodes. Furthermore, the lymphatic sprouts grown in our model displayed similar characteristics with *in vivo* lymphatic capillaries in biochemical and morphological features. We also demonstrated the potential utility of our model in testing pharmacological modulators of lymphangiogenesis with quantitative evaluations and phenotypic changes with enhanced predictive potential.

The microscale system presented in this thesis provides a novel *in vitro* model of blood/lymphatic formation and function with improved physiological relevance and reliability, and expected to have wide range of applications across pharmaceutical and biomedical researches.

Keywords: blood vessels, lymphatic vessels, angiogenesis, lymphangiogenesis, endothelial cells, fluid shear stress, microfluidic device

Student number: 2009-30161

<b>Abstract</b>	<b>i</b>
<b>Contents</b>	<b>iv</b>
<b>List of Tables</b>	<b>viii</b>
<b>List of Tables</b>	<b>ix</b>
<b>Chapter</b>	
<b>1 Introduction</b>	<b>1</b>
<b>2 Engineering of functional, perfusable 3D microvascular networks through reconstitution of vasculogenesis and angiogenesis on a chip</b>	<b>6</b>
<b>2.1 Introduction</b>	<b>6</b>
<b>2.2 Materials and methods</b>	<b>8</b>
<b>2.2.1 Device fabrication</b>	<b>8</b>
<b>2.2.2 Cell culture</b>	<b>9</b>
<b>2.2.3 Vasculogenesis cell seeding</b>	<b>10</b>
<b>2.2.4 Angiogenesis cell seeding</b>	<b>10</b>
<b>2.2.5 Measuring the success rate of vessel perfusion</b>	<b>11</b>
<b>2.2.6 Immunostaining</b>	<b>12</b>
<b>2.2.7 Imaging</b>	<b>13</b>

2.2.8	Measurement of vessel permeability -----	13
2.2.9	Inflammatory response and HL-60 adhesion experiments -----	14
2.2.10	Fluid perfusion experiments and statistical analysis of endothelial NO synthesis -----	15
2.2.11	Quantification of vessel area and length of sprouts ----	17
2.3	Results -----	18
2.3.1	Microfluidic chip and experimental design -----	18
2.3.2	Formation of vasculogenesis- and angiogenesis-derived microvascular networks -----	19
2.3.3	Morphological and biochemical characterization of the vessels -----	21
2.3.4	Perfusable and intact lumina of the engineered microvascular networks -----	22
2.3.5	Flow-induced endothelial responses -----	24
2.3.6	In vitro modeling of endothelial interactions with pericytes, cancer cells and leukocytes -----	26
2.4	Discussion -----	28
2.5	Conclusions -----	30

<b>3</b>	<b>Reconstitution of sprouting morphogenesis of lymphatics under combined stimulation of pro-lymphangiogenic factors and interstitial flow</b>	<b>52</b>
	<b>3.1 Introduction</b>	<b>52</b>
	<b>3.2 Materials and methods</b>	<b>55</b>
	<b>3.2.1 Device fabrication</b>	<b>55</b>
	<b>3.2.2 Cell culture and seeding in microfluidic devices</b>	<b>55</b>
	<b>3.2.3 Immunostaining and confocal imaging</b>	<b>58</b>
	<b>3.2.4 Quantitative validation of interstitial flow across 3D ECM</b>	<b>58</b>
	<b>3.2.5 Treatment of anti-lymphangiogenic factors</b>	<b>59</b>
	<b>3.2.6 Quantification and statistical analysis</b>	<b>60</b>
	<b>3.3 Results</b>	<b>60</b>
	<b>3.3.1 Microfluidic platform for lymphatic sprouting under stimulation of pro-lymphangiogenic factors and interstitial flow</b>	<b>60</b>
	<b>3.3.2 Sprouting of lymphatic endothelial cells in response to gradients of pro-lymphangiogenic factor</b>	<b>61</b>
	<b>3.3.3 Presence, direction and magnitude of interstitial flow</b>	

	determin activity of lymphatic sprouting -----	62
3.3.4	Interstitial flow regulates lymphatic capillary network formation and directional expansion -----	64
3.3.5	Interstitial flow drives directional sprouting growth and filopodia formation -----	66
3.3.6	Lymphatic sprouts exhibit structural and biochemical characteristics of <i>in vivo</i> lymphangiogenesis -----	67
3.3.7	Modulation of lymphangiogenesis by small molecule inhibitors and inflammatory cytokine -----	68
3.4	Discussion -----	70
4	Conclusions -----	92
	References -----	94
	Abstract (in Korean) -----	107

## List of tables

- Table 2.1** Comparison of engineering-based *in vitro* blood vessel models for permeability coefficient tested using 70 kDa FITC-dextran
- Table 3.1** Notation for gradient of pro-lymphangiogenic factors and interstitial flow
- Table 3.2** Small molecule inhibitors tested for anti-lymphangiogenic activity

## List of figures

**Fig 2.1** Microfluidic chip design and cell seeding configurations for microvascular network and angiogenic sprout formation. (A) Photograph of the microfluidic chip, filled with colored fibrin matrix. (B) Schematic of the microfluidic channels partitioned by microposts. The central channel (C, blue) is flanked by two fluidic channels (Left Inside, LI, and Right Inside, RI, both colored purple) and two outside stromal cell culture channels (Left Outside, LO, and Right Outside, RO, both colored green). (C, D) Cell-seeding configuration for the vasculogenesis experiment. (E, F) Cell-seeding configuration for the angiogenesis experiment.

**Fig 2.2** Microfluidic chip channel configurations for vasculogenesis, angiogenesis and fluid perfusion experiments on a chip. (A) Channel configuration for vasculogenesis on a chip involves 1,000  $\mu\text{m}$  wide and 250  $\mu\text{m}$  high channel, which is partitioned with 300  $\mu\text{m}$  long hexagonal microposts spaced every 100  $\mu\text{m}$ . (B) For angiogenic sprout formation, narrower central channels, having widths of 700  $\mu\text{m}$ , were fabricated. Hexagonal microposts with 100  $\mu\text{m}$  diameter were placed to have 100  $\mu\text{m}$  interpost gaps between them. We fabricated a master with structures of 100  $\mu\text{m}$  height. (C) Modification of chip design for fluid perfusion experiment, which adds inlet for syringe pump-driven fluid flow into the angiogenesis-derived vascular networks.

**Fig 2.3** Time-series micrographs of vasculogenic and angiogenic vessel

formation in the fibrin matrix. Vasculogenesis: (A) day 1, HUVECs elongate and start to connect to each other. (B) Day 2, HUVECs start to form a network *via* a dynamic remodeling process, while nascent lumen structures appear. (C) By day 3, hollow lumina of HUVECs grow larger and merge to form well-interconnected tubular structures. (D) By day 4, a perfusable microvascular network is established as the luminal sides of the vessels are connected to the medium channels. Angiogenesis: (E) within 24 h after attaching HUVECs to fibrin walls in the central channel, endothelial sprouts with tip cells appear along the central fibrin matrix. (F) By day 2, vacuole formation starts in stalk regions. The sprouts continue to extend across the middle channel. (G) By day 3, defined lumina can be observed within the sprouts. (H) By day 4, growing angiogenic sprouts traverse across the entire width of the 700  $\mu\text{m}$  central channel, establishing perfusion through luminal access with the RI medium channel. Cells were labeled with CellTracker green and fixed and stained for nuclei (blue). (I) Quantification of vasculogenic vessel network growth by total vascular covered area in *z*-projected image ( $n = 6$  chips per day per condition). (J) Quantification of angiogenic sprout growth by tip cell distance from the left side of fibrin matrix ( $n = 5$  chips for day 1, 2, 3 and  $n = 4$  chips for day 4). Scale bar, 100  $\mu\text{m}$ ; error bars represent SEM.

**Fig 2.4** Requirement for patterned co-culture of HUVECs and LFs in vasculogenesis on a chip. (A) HUVECs cultured for 4 days without

LFs at the stromal cell culture channels(LO and RO) (B) HUVECs and LFs co-cultured within central channel forming interconnected vascular networks at day 5 with a ratio of 5 to 1 ( $3 \times 10^5$  cells/mL of HUVECs and  $6 \times 10^4$  cells/mL of LFs). (C) In a patterned co-culture condition at day 4, tubules near the interpost openings developed perfusable openings (white arrowheads) at the fibrin matrix/media interfaces (denoted as dashed line). (D) Tubules observed in a mixed co-culture condition, grown for 5 days, rarely extended toward the interfaces, and displayed closed, non-perfusable lumens (yellow arrowheads) within fibrin matrix. Scale bars, 100  $\mu\text{m}$ .

**Fig 2.5** (A) EDU proliferation assay performed for growing angiogenic sprouts revealed that most endothelial proliferation (purple nuclei) occurred at the stalk regions of sprouts, and tip cells at the fronts were characterized by non-proliferating phenotype (blue nuclei). Scale bar, 50  $\mu\text{m}$ . (B, C) HUVECs cultured without LFs or with ipsilateral LF-seeding exhibited little or no sprout formation after 3 days of culture. Scale bar, 100  $\mu\text{m}$ . (D) Angiogenic sprouts, grown for 3 days induced by VEGF gradient (0 – 50 ng/mL) exhibited relatively inefficient length extension and lumenization compared to the LF-induced sprouts.

**Fig 2.6** Morphological features of engineered 3D microvessels and growing angiogenic sprouts. (A–B) Confocal micrographs showing the overall architectures of vascular networks established by (A) vasculogenic and (B) angiogenic processes at day 4. Scale bars, 100  $\mu\text{m}$ . (C) Angiogenic

sprouts grown for 2 days. Scale bar, 50  $\mu\text{m}$ . (D) Higher magnification image shows the F-actin-rich filopodia extensions of angiogenic tip cells. Scale bar, 20  $\mu\text{m}$ .

**Fig 2.7** Patency of 3D hollow lumens and biochemical characteristics of microvessels. Confocal sections of the vasculatures formed via vasculogenesis (A) and angiogenesis (B) exhibited presence of hollow lumens, forming well-interconnected networks. Scale bars, 100  $\mu\text{m}$ . (C) Cross-sectional images of a blood vessel showing a hollow lumen enclosed by ECs. Scale bar, 10  $\mu\text{m}$ . (D) Microvascular network immunostained against adherens junction proteins, VE-cadherin (green) and  $\beta$ -catenin (red). Scale bar, 30  $\mu\text{m}$ . (E) Expression of tight junction protein ZO-1 at cell-cell contacts, displaying localization of continuous and intact intercellular connections. Scale bar, 20  $\mu\text{m}$ . (F) Longitudinal cross-section of a TNF- $\alpha$ -stimulated blood vessel stained for ICAM-1 (green) and collagen IV (red). Scale bar, 10  $\mu\text{m}$ . (G, H) Confocal micrographs of vessels stained for the major components of basement membrane, laminin (purple) or collagen IV (red). Scale bars, 20  $\mu\text{m}$ .

**Fig 2.8** Introduction of solutions containing microbeads or fluorescent dye into the perfusable microvessels. (A) Red fluorescent microbeads (7  $\mu\text{m}$ , red) introduced into the microvascular network exclusively localize within the luminal space of F-actin-labeled endothelium (green). (B) Intravascular introduction of FITC-dextran (70 kDa, green) into the blood vessel labeled with CellTracker red. Scale bar, 20  $\mu\text{m}$ . Inset scale

bar, 200  $\mu\text{m}$ .

**Fig 2.9** Long-term stability of patent and perfusable lumens. Microvascular networks formed both by vasculogenesis (A) and angiogenesis (B) maintained perfusable and patent lumen for more than 7 days after perfusion had established, without discernible vessel regression or endothelial apoptosis. Scale bars, 50  $\mu\text{m}$ .

**Fig 2.10** Distribution of vessel diameter constituting perfusable microvascular network formed via angiogenic process.

**Fig 2.11** F-actin cytoskeleton reorganization in response to luminal flow (a) F-actin (green) distribution of ECs under static conditions. Scale bar, 20  $\mu\text{m}$ . (b) Changes in F-actin distribution in response to luminal flow for 2 h. Scale bar, 20  $\mu\text{m}$ .

**Fig 2.12** Endothelial nitric oxide synthesis stimulated by presence of luminal flow. (A-C) Endothelial NO synthesis in the absence of L-arginine supplement in perfusate. Without L-arginine, NO synthesis quantitatively assessed by DAF-FM DA (green) fluorescence intensity showed only insignificant increase in response to luminal fluid flow ( $n=5$  for static,  $n=6$  for flow condition). (D-F) Significant increase in fluorescent intensity of DAF-FM DA after exposure to 1 h of luminal flow, with L-arginine supplement in perfusate. Quantitative analysis of the fluorescence intensity showing a 14-fold increase after flow exposure, compared to static conditions ( $n = 9$  for static,  $n = 7$  for flow condition,  $***p < 0.005$ ). For quantification of NO synthesis based on

fluorescent intensity, images were obtained under identical conditions. Scale bar, 50  $\mu\text{m}$ . Error bars represent SEM.

**Fig 2.13**

Endothelial cell interactions with pericytes, cancer cells and leukocytes. (a) Microvascular network (CD31, red) covered with pericytes ( $\alpha$ -SMA, green). Scale bar, 50  $\mu\text{m}$ . (b) Higher magnification image and corresponding confocal sections of a pericyte-decorated blood vessel. Scale bar, 20  $\mu\text{m}$ . (c, d) Confocal micrographs of angiogenic sprouts grown for 2 and 4 days under co-culture with U87MG cancer cells, characterized by the sprouts with branching tip cells (white arrowhead) and convoluted and aberrantly fused tubules (yellow arrowhead). Scale bars, 20  $\mu\text{m}$ . (e) Expression of ICAM-1 (green) on the apical surface of blood vessels in response to inflammatory cytokines TNF- $\alpha$  (50 ng/mL) or IL-1 $\alpha$  (2 ng/mL). Scale bar, 50  $\mu\text{m}$ . (f) Adhesion of activated HL-60 neutrophils (green) on the inner surface of endothelium (red) promoted by endothelial stimulation with TNF- $\alpha$ . Scale bar, 20  $\mu\text{m}$ .

**Fig 3.1**

Microfluidic chip for investigation of lymphatic sprouting under combined stimulation biochemical stimulants and interstitial flow. (A) A schematic diagram of microfluidic chip comprised of three independent hydrogel channels and two fluidic channels. (B, C) Schematics of experimental configuration for pro-lymphangiogenic factor gradient formation and application of interstitial flow. Addition of pro-lymphangiogenic factors either to LF or RF channel (RF channel in the figure) develops diffusion based concentration gradient over time.

Applying defined volume difference to the reservoirs connected to RF and LF channel resulted in pressure gradient that drives interstitial flow. (D) Quantitative validation of interstitial flow with direction from RF to LF channel with varying hydrostatic differential applied via defined volume differences, showing interstitial flow level proportional to the applied volume differences.

**Fig 3.2** Pro-lymphangiogenic factors and interstitial flow synergistically induced lymphatic sprout formation and growth. (A) With no pro-lymphangiogenic factors, LECs showed no invasion into the fibrin matrix. (B, C) LECs stimulated with cocktail of pro-lymphangiogenic factors (VEGF-A, VEGF-C, bFGF and S1P) invaded into the fibrin matrix to form sprout-like multicellular structures during 2 days of culture. (D) Application of interstitial flow with no pro-lymphangiogenic factors, invasion of LECs were rarely observed. (E, F) In the presence of the cocktail and interstitial flow, LECs exhibited greater sprout formation and growth against the direction of flow, showing multicellular collective migration forming well-defined lumens. (G, H) Quantification of LEC invasion into fibrin matrix. \*P < 0.05, \*\*\*P < 0.0005. n = 4 chips per each condition for Fig 3.2G, and at least 10 chips for Fig 3.2H.

**Fig 3.3** LECs tested with negative concentration gradient (A), and higher hydrostatic pressure at the LF channel (B) resulted in inactive lymphatic sprout formation and growth.

- Fig 3.4** LECs stimulated with cocktail of pro-lymphangiogenic factors comprised of VEGF-D, HGF, IGF-1 and PDGF-BB either in static (A) or interstitial flow condition (B), also revealing flow-enhanced sprouting activity.
- Fig 3.5** Comparison of presence and absence of co-culturing stromal fibroblasts. Scale bar, 100  $\mu\text{m}$ .
- Fig 3.6** Magnitude of interstitial flow modulates morphology of cellular protrusions and cellular invasion. (A) LECs tested with varying magnitudes of interstitial flow for 6 and 12 h. Insets display enlarged image of protrusions. Scale bar, 100  $\mu\text{m}$  (20  $\mu\text{m}$  for insets). (B) Quantification of the length of protrusions and (C) Quantification of cell nuclei invaded into fibrin matrix. Error bars represent SEM. For quantifications, at least 3 chips (~ 200 cellular protrusions and 9 apertures) per each condition were analyzed.
- Fig 3.7** Interstitial flow regulates lymphatic capillary network formation and directional expansion of network. (A-C) images showing lymphatic network formation at channel A and subsequent expansion into the adjacent acellular fibrin matrix in channel B in the presence of pro-lymphangiogenic factors and either static (A) or different flow conditions with directional indicated with arrows (B, C). Presence of interstitial flow, regardless of the direction, significantly enhanced organization of LECs into the interconnected capillary networks in the channel A as quantified in the graph (D). In the static condition, LECs

moderately migrated into the channel B, while the migration can be either greatly enhanced or largely suppressed depending on the presence and direction of interstitial flow as quantified in the graph (E). n = 6 chips per condition. \*P < 0.05, \*\*P < 0.005, \*\*\*P < 0.0005. (F) A schematic of the chip having two central channels, allowing investigation of interstitial flow-driven lymphatic capillary network formation and expansion. Scale bar, 100  $\mu$ m.

**Fig 3.8** Interstitial flow regulates filopodia formation and directional alignment of lymphatic sprouts. (A) Under static conditions (G+F0 and G=F0), the lymphatic sprouts exhibited relatively smooth outlines with rare filopodia projections. (B) In the presence of interstitial flow (G=F+), numerous filopodia protrusions were observed at the LECs of distal tip positions as well as behind following positions, with marked difference with static condition. (C) A representative of characteristic morphological figure of lymphatic sprouts under combined stimulations (G=F+), displaying numerous filopodia protrusions along the entire length of sprouts as indicated with yellow arrowheads. (D-F) Semicircular polar histograms demonstrating distribution of angles of lymphatic sprouts relative to the horizontal axis n = 9 chips per condition. Length of each bar indicates percentage of sprouts aligned to the corresponding angle; (D, E) Lymphatic sprouts formed under G+F0 condition displayed relatively narrower distribution compared to the lymphatic sprouts formed G=F0 condition. (F) In the presence of

interstitial flow, lymphatic sprouts were well-aligned along the streamline of flow. Scale bars, 50  $\mu\text{m}$ .

**Fig 3.9** Patency of hollow lumens and lymphatic-specific marker expression. (A) Confocal sections of lymphatic sprouts showing continuous and hollow lumens enclosed by LECs. (B-D) Expression of lymphatic specific markers confirmed via immunofluorescence analysis against LYVE-1 (B), VEGFR-3 (C) and Prox-1 (D). Scale bars, 50  $\mu\text{m}$ .

**Fig 3.10** Immunofluorescent images for characteristic basement membrane and adherens junction expression. A part of lymphatic sprouts stained against collagen IV (A) and laminin (B) confirm presence of perforated, discontinuous basement membrane around the lymphatic vessels. (C) Growing lymphatic sprouts display “zipper-like” VE-cadherin pattern. Scale bars, 20  $\mu\text{m}$ .

**Fig 3.11** Lymphatic sprouts grown with small molecule inhibitors. (A) Quantification of invasion area of lymphatic sprouts.  $n = 9$  chips per each dose of small molecule inhibitor. (B-J) Representative images of lymphatic sprouts showing dose-dependent inhibition of lymphatic sprout growth. Scale bars, 50  $\mu\text{m}$ .

# Chapter 1

## Introduction

Blood and lymphatic vessels form an intricate system of hierarchically branched networks throughout the body, while retaining considerable plasticity to accommodate demands of surrounding tissues. In the adults, the vessels acquire quiescent, stable states, and are responsible for circulation and homeostasis of fluid components. In certain physiological or pathological situations, endothelial cells become activated and then undergo dynamic remodeling predominantly via neovessel sprouting from pre-existing vessels, termed angiogenesis (sometimes referred as hemangiogenesis to clearly separate it from the process of lymphangiogenesis) for blood vessels and lymphangiogenesis for lymphatic vessels respectively [1]. Given the importance of these vessels in human physiology, it is not surprising that more than a hundred of pathologies, including tumor metastasis, diabetic retinopathy, age-related macular degeneration and autoimmune diseases, are associated with functional abnormalities and aberrant growth of blood and lymphatic vessels [2, 3].

Research efforts aimed to gain knowledge in vascular biology can be greatly benefited from accurate cell culture-based model system which closely mimics cellular dynamics of endothelial cells or characteristic functional, structural feature of vessels as observed *in vivo*, while allowing precise control over the parameters of interests and simple experimental procedure with minimal manipulations. While use of *in vivo* animal models allows physiologically relevant interrogations, but they are inherently complex, difficult to manipulate certain parameters of interest and results are usually

compounded by coupling of examining parameters. Although conventional cell culture-based models have contributed greatly to the current knowledge in the field of vascular biology, they usually suffer from severe discrepancies between cellular behaviors observed *in vitro* and their natural *in vivo* counterparts [4, 5]. These discrepancies found in these models mainly stem from the fact that they usually rely on artificial cell-culture environments where some of key constituents of *in vivo* vascularized tissues are missing, leading to compromised functions and partial mimicry of complex morphogenesis processes. *In vitro* examination of cells in the artificial culture environments may lead to misunderstandings in physiology and pathology of endothelial cells, which has been indicated as a major bottleneck in developments of clinically useful therapies and effective drugs aimed to target angiogenesis and lymphangiogenesis-related disorders.

Among the factors contributing characteristic functions and cellular behaviors of ECs *in vivo*, three-dimensional cellular supports by extracellular matrices, fluid-shear induced mechanical stimuli, communications between endothelial and stromal cell types and biochemical cues are indispensable components not only for proper function of quiescent vessels but also for the processes of neovessel formation. Thus, a main breakthrough should be made to address the problems found in conventional system is smart integration of key environmental constituents of endothelial cells in a single *in vitro* model. The studies performed in this thesis motivated by this technically challenging, unmet demand.

Application of technologies developed in micr/nano-scale engineering to biological studies has been creating novel experimental opportunities by providing exquisite spatiotemporal manipulation of biochemical and mechanical stimulants in reproducible,

cell-type relevant manners [6, 7]. A decade of advances in engineering-based *in vitro* model developments have brought emergence of ‘organ-on-a-chip’ concept [8], replicating organ-level of cellular structures and functions using sophisticated *in vitro* models. In these platforms where enhanced cellular phenotypes mimicking organ-level lung, kidney and gut functions *in vitro* [9-11], researchers used engineering based-approach to reconstitute organ-specific cellular structures, interactions between multiple cell types and adequate biochemical and mechanical stimuli in a single platform. Along with the developments of microfluidic-based cell culture systems, developments of microfluidic-based model of reconstituting *in vivo* blood vessels and angiogenesis have been sought to be fulfilled by numerous research groups [12-15] owing to their expected benefits, but still remained as a task that still remains much to be improved [16].

In this thesis, we developed a novel microfluidic-based cell culture platform which allows 3-dimensional co-culture of endothelial cells and stromal cells in a controlled biochemical and mechanical stimulants. Based on the flexible configurations and spatiotemporal manipulations of cells, extracellular matrices, biochemical gradients and fluid flow within the cell culture system, we demonstrated that blood endothelial cells (BECs) and lymphatic endothelial cells (LECs) undergo coordinated morphogenesis processes in close resemblances with the corresponding processes observed *in vivo*. Of noted, incorporation of flow-induced mechanical stimuli in 3D cellular environments enabled us to create unprecedented functionality of blood vessels and investigate unexplored roles of lymphatic drainage in the process of lymphangiogenesis.

Chapter 2 describes the development of a microfabricated, multichannel microfluidic chip which provide robust and sophisticated methods to engineer cellular

microenvironments of endothelial cells in 3D, enabling us to reconstitute morphogenesis and characteristic functions of blood endothelial cells (BECs). The microfluidic chip is optimally suitable for multicellular co-culture of endothelial and stromal cell types in 3D extracellular matrix with precisely controlled spatial patterns, allowing paracrine intercellular signaling between them. We used this microfluidic chip to create functional and perfusable 3D microvascular networks from human primary endothelial cells via two distinct processes, vasculogenesis and angiogenesis. To closely simulate these two processes in our chip, we used surface tension-assisted 3D ECM patterning technique, culturing human endothelial cells and stromal fibroblasts in defined relative location and seeding conditions. Interactions between these two cell types lead to formation of complexly interconnected networks of microvessels through the intrinsic processes of developmental vascular patterning (vasculogenesis) and neovessel sprouting from pre-existing networks (angiogenesis). In structural aspects, the blood vessels formed in the model demonstrate with well-defined lumens with apical-basal polarity, continuous basement membrane and intact interendothelial junctions, which resemble characteristic features of *in vivo* endothelium. Of particular note, endothelial cells participating in the microvascular network formation spontaneously develop perfusable lumens allowing intraluminal flow to be applied across the vascular networks, which has not been demonstrated previously. Notably, this unique feature of our microvascular networks recreates blood vessel-specific mechanical stimuli on the inner side of endothelium, thus directs expression of unique functional characteristics such as strong barrier function, nitric oxide synthesis and cytoskeletal rearranges of ECs.

In Chapter 3, we expand the usage of our microfluidic chip for investigation of

lymphangiogenesis, a process of sprouting morphogenesis of lymphatic endothelial cells, motivated by the lack of robust and physiologically relevant *in vitro* lymphangiogenesis assay. We describe the use of reliable microscale platform to reconstitute lymphatic sprouting in 3D extracellular matrix under combined stimulation of pro-lymphangiogenic factors and interstitial flow, which correspond to key constituents of tumor and inflammatory microenvironments. With flexibly configured cellular microenvironments of LECs, we found that sprouting morphogenesis of human lymphatic endothelial cells (LECs) in response to pro-lymphangiogenic factors can be either abrogated or further augmented by the presence of interstitial flow, and that the direction and the magnitude of interstitial flow dictate extents of lymphatic sprouting as well as morphological characteristics. In a combined stimulation of growth factors and interstitial flow, human LECs actively formed multicellular sprouts with characteristic morphological features, biochemical markers and perforated basement membrane, which are in a reminiscence of *in vivo* lymphatic capillaries. Based on the robust and reproducible feature of our model, we investigated the effects of small molecule inhibitors on morphology and growth of lymphatic sprouts. Together, these results demonstrate that biomolecular stimuli and interstitial flow cooperate to coordinate lymphatic sprouting, suggesting that increased lymphatic drainage by high interstitial pressure in tumors, combined with the tumor-secreted growth factors, could exacerbate peritumor lymphangiogenesis.

## Chapter 2

# Engineering of functional, perfusable 3D micro-vascular networks

### 2.1. Introduction

The circulatory system is constructed from a network of blood vessels, which mediate a wide range of functions including cellular and biochemical transport, nutrient and oxygen exchange, and temperature regulation, while maintaining a high degree of plasticity throughout the life of an organism. The foundation of this system is vascular endothelial cells (ECs), the building blocks which regulate transvascular transport, vasodilation, and vessel formation and regression. As with any system of such complexity, malfunction and dysregulation can lead to a multitude of pathologies [17], thus engineering blood vessels *in vitro* is an important tool for the discovery of drugs and therapeutics to treat such pathologies.

Toward this goal, there are numerous reports of *in vitro* experimental systems developed to investigate vessel dynamics and function. For example, ECs cultured on 2D glass substrates or porous membranes are widely used for the investigation of barrier function [18], mechanosensitive response of the endothelium [19], and transendothelial migration of blood-borne cells including leukocytes [20] and circulating tumor cells (CTCs) [21]. However, such 2D monolayer-based systems lack three-dimensional

contexts important for the native architectures and functions of blood vessels [22, 23], thus failing to reflect biological complexities found in real organisms.

In contrast, three-dimensional extracellular matrices (ECMs) can provide an enhanced environment for multicellular organization of ECs as well as cell–cell and cell–matrix interactions [24, 25], all of which have been shown to be critical in endothelial morphogenesis and function. However, conventional 3D *in vitro* models have not provided a robust experimental method to grow readily perfusable blood vessels, precluding their use in the experiments requiring selective delivery of small molecules, soluble proteins or cell suspensions to the luminal surface of the endothelium. Furthermore, the resulting cellular microenvironments in these models do not capture key mechanical cues defined by luminal flow which play central roles in the modulation of endothelial functions.

Recent reports, assisted by micro-technology, demonstrated *in vitro* perfusable vessel analogues made by endothelialization of channel-molded hydrogels or microfluidic channels to mimic endothelial cell migration, vascular barrier function, inflammatory response, thrombosis and tumor cell intravasation under defined biomolecular and mechanical stimulations [12, 26-30]. Unfortunately, as these vessels did not follow natural endothelial morphogenesis in making the lumenized structure, they were limited in their ability to reconstitute the characteristic features and responses of *in vivo* endothelia. Several microfluidic approaches have made important progress toward the formation of 3D endothelial tubes *via* physiologically relevant processes [13, 14, 31-34]. Nonetheless, these approaches still fail to provide a practical methodology that closely emulates complex endothelial dynamics to grow native 3D vascular

networks which encompass readily perfusable lumina, intact barrier properties, and physiological functions defined by biomechanical stimuli.

Here we report a novel microfluidic platform and robust approach to form perfusable and functional microvascular networks in 3D ECM constructs. The approach uses flexibly designed cellular co-cultures to facilitate controlled heterotypic cell–cell interactions, which reproduces the physiological morphogenesis of ECs to form interconnected networks of microvessels. We have successfully demonstrated that the formation of microvascular networks and the establishment of perfusable lumina are spontaneously directed by ECs and reproduced in a robust manner. The open, long-lasting microvascular networks replicate important features of living vasculatures including native 3D vascular architectures, characteristic biochemical markers, intact barrier function and patent lumina that support luminal flow. In particular, the application of physiological shear stress induced F-actin rearrangement and nitric oxide production in ECs, suggesting that our system efficiently combines important vessel-specific responses and functions in physiologically relevant 3D contexts.

## **2.2. Materials and methods**

### **2.2.1. Device fabrication**

Microfluidic devices were fabricated out of polydimethylsiloxane (PDMS, Sylgard 184, Dow Corning) using soft lithography and replica molding. A master with positive relief patterns of photoresist, SU-8 (MicroChem), on a silicon wafer was prepared by photolithography. A PDMS prepolymer made of a 10 : 1 (*w/w*) mixture of PDMS base and curing agent was cast against the master and thermally cured to obtain a negative

replica-molded piece. After separation from the master, hydrogel injection ports and the reservoirs for the cell culture medium were punched out of the molded PDMS with a sharpened 18 gauge blunt hypodermic needle and a 6 mm biopsy punch. The PDMS devices and glass coverslips were cleaned with residue-free tape and nitrogen gas air gun, and then treated with oxygen plasma for 45 s to form covalent bonding between them. To restore hydrophobicity to the PDMS after plasma treatment, the devices were kept in an 80 °C dry oven for at least 24 h and sterilized by UV irradiation before each experiment.

### **2.2.2. Cell culture**

Human umbilical vein endothelial cells (HUVEC, Lonza) were cultured in Endothelial Growth Medium (EGM-2, Lonza) and passages 3 to 5 used for experiments. Normal human lung fibroblasts (LF, Lonza) were cultured up to passage 10 in Fibroblast Growth Medium (FGM-2, Lonza). Cell cultures were grown to 80% confluence prior to passage or use in experiments. Human promyelocytic leukemia cells, HL-60 (a gift from Dr Sunghoon Kim at Seoul National University), were cultured in RPMI-1640 (Hyclone, USA) supplemented with 10% fetal bovine serum, penicillin (100 U/mL), streptomycin (100 U/mL) and HEPES (25 mM). For the investigation of inflammatory response-mediated HL-60 adhesion inside the vessels, HL-60 cells were differentiated over 5 to 7 days in a culture medium containing 1.3% DMSO (Sigma, USA), at an initial concentration of  $2 \times 10^5$  cells/mL. Human glioblastoma multiforme cells, U87MG (a gift from Dr Sun Ha Paek at Seoul National University), were cultured in DMEM supplemented with 10% FBS, penicillin (100 U/mL) and streptomycin (100 U/mL). All cells were maintained in a humidified incubator at 37 °C and 5% CO<sub>2</sub>.

### **2.2.3. Vasculogenesis cell seeding**

The fibrinogen solution was prepared by dissolving 2.5 mg mL<sup>-1</sup> bovine fibrinogen (Sigma) in DPBS (Gibco) and supplementing aprotinin (0.15 U/mL, Sigma) and collagen type I (0.2 mg/mL, BD bioscience) to the solution. Collagen type I was added to the pure fibrin matrix to enhance lumen formation of developing tubular structures [35]. After disassociation from culture dishes using 0.25% Trypsin-EDTA (Hyclone), HUVECs and LFs were suspended in the fibrinogen solution, at a concentration of 2 or 3 × 10<sup>6</sup> cells/mL for HUVECs and 5 × 10<sup>6</sup> cells/mL for LFs. The cell solutions were mixed with thrombin (0.5 U/mL, Sigma) and then immediately introduced into a central channel and stromal cell culture channels (LO, RO). The cell-suspended gel constructs were allowed to clot for 5 min at room temperature. The inlet reservoirs of the cell culture medium channels (LI, RI) were loaded with EGM-2 medium, and then vacuum was applied at the outlet reservoirs to fill the hydrophobic channels. Following loading all four reservoirs, the microfluidic platforms were incubated at 37 °C and 5% CO<sub>2</sub>. The cell culture medium was removed and refilled with fresh EGM-2 culture medium every 24 h.

### **2.2.4. Angiogenesis cell seeding**

LFs were dissociated from culture dishes and resuspended in a 2.5 mg/mL bovine fibrinogen solution (2.5 mg/mL fibrinogen, 0.15 U/mL aprotinin, 0.2 mg/mL collagen type I) at a cell concentration of 10<sup>7</sup> cells/mL, mixed with thrombin (0.5 U/mL) and immediately injected into a single stromal cell culture channel. The central channel and remaining stromal cell culture channel were filled with 2.5 mg/mL fibrin solution (0.15 U/mL aprotinin, 0.2 mg/mL collagen type I, 0.5 U/mL thrombin) and left to clot at room

temperature for 5 min. After polymerization of the fibrin gel, EGM-2 medium was loaded into cell culture reservoirs and vacuum applied to fill medium channels. The device was incubated for 24 h at 37 °C and 5% CO<sub>2</sub> to allow any air bubbles on the gel–medium interface to dissipate and fibroblasts to become established within the fibrin gel matrix. HUVECs suspended in EGM-2 at a concentration of  $5 \times 10^6$  cells/mL were introduced to the medium channel contralateral to the LF seeding, after removal of the medium from the corresponding medium reservoirs. The microfluidic chip was then tilted by 90 degrees and incubated for 30 min, allowing HUVECs to adhere on the fibrin gel surface. Then the reservoirs were filled with EGM-2 and the chip kept in an incubator. In order not to disturb the gradient of LF-secreted factors, cell culture media were replaced only once after 3 days of co-culture by aspiration and refilling with fresh EGM-2 culture medium.

To observe the incorporation of pericytes during angiogenic sprout growth, human placenta pericytes (PromoCell) were resuspended with 2.5 mg/mL of a fibrinogen solution at a concentration of  $5 \times 10^5$  cells/mL, and mixed with a thrombin solution to be injected into the central channel. For angiogenic sprouting in response to the cancer cells, U87MGs at a concentration of  $10^7$  cells/mL were used to be seeded contralaterally to the HUVECs in 2.5 mg/mL fibrin matrix. The rest of the experimental procedures were performed in the same way as in the angiogenesis experiments described above.

#### **2.2.5. Measuring the success rate of vessel perfusion**

To confirm whether the microvascular networks formed in our chip were perfusable, we used polystyrene beads of 7 µm diameter suspended in PBS solution. After 4 days of vasculogenic and angiogenic vessel formation, the reservoirs of each device were

aspirated and the bead-suspending PBS solution was added on one side, allowing hydrodynamic forces to induce fluid flow through the microvascular networks. We checked whether the lumina at the interpost openings allowed the advective transport of beads, and counted the number of openings that were perfusable. We set out the criteria so that the microvascular networks where at least half of the openings allowed the passage of beads were determined as perfusable networks.

### **2.2.6. Immunostaining**

Mouse monoclonal antibodies specific for human VE-cadherin (Alexa Fluor®488, clone 16B1) were purchased from eBioscience. Mouse monoclonal antibodies specific for ICAM-1 (Alexa Fluor®488, clone HCD54) and CD31 (Alexa Fluor®647, clone WM59) were purchased from BioLegend. Mouse monoclonal antibodies specific for human  $\alpha$ -smooth muscle actin ( $\alpha$ -SMA, Alexa Fluor®488, clone 1A4) and  $\beta$ -Catenin (Alexa Fluor®647, clone L54E2) were from R&D Systems and Cell Signaling, respectively. Rabbit polyclonal antibodies against human laminin and human collagen IV were purchased from Abcam. Mouse monoclonal antibody specific for human ZO-1 (Alexa Fluor®594, clone ZO1-1A12), Alexa Fluor®568 goat anti-rabbit IgG, Phalloidin (Alexa Fluor®488) and Hoechst 33342 were from Molecular Probes.

After washing cultures once with phosphate-buffered saline (PBS, Hyclone), cells were fixed in 4% (*w/v*) paraformaldehyde in PBS for 15 min, and then permeabilized using a 0.15% Triton X-100 (Sigma) in PBS solution for 15 min. After blocking using 3% bovine serum albumin (BSA, Sigma) in PBS for 1 h, samples were incubated overnight at 4 °C either with primary antibodies directly conjugated with fluorescent marker (VE-cadherin; 1 : 100, ICAM-1; 1 : 200, CD31; 1 : 200,  $\alpha$ -SMA; 1 : 200,  $\beta$ -Catenin; 1 : 200,

ZO-1; 1 : 100) or unconjugated antibodies (collagen IV; 1 : 100, laminin; 1 : 100), followed by incubation with fluorescence-conjugated secondary antibodies (1 : 1000, 4 h, 4 °C). For staining F-actin and DNA, Alexa Fluor®488-Phalloidin (66 nM) and Hoechst 33342 (1 : 1000) were added to the chip for 1 h of incubation at room temperature. The samples were washed three times and stored in PBS before imaging. The EdU cell proliferation assay kit was purchased from Molecular Probes, and used according to the manufacturer's instructions.

### **2.2.7. Imaging**

For cross-section and whole-construct imaging of 3D blood vessels, stained samples were examined using a FluoView FV1000 confocal laser scanning unit with the IX81 inverted microscope (Olympus) and images were captured with a confocal PMT detector. Lenses in use were x10, x20 and x40 (Olympus). Confocal images were processed by IMARIS software (Bitplane). A Phase-contrast (PhC) microscope (IX71; Olympus) or a differential interference contrast (DIC) microscope (IX81; Olympus) were used to perform visual microscopic observation and image acquisition of blood vessels.

### **2.2.8. Measurement of vessel permeability**

The permeability coefficient of the blood vessels was quantified by introducing FITC-dextran (70 kDa, 10 µM, Sigma) into the microvascular networks derived from angiogenesis experiments, capturing time-sequential images of FITC-dextran diffusing through the endothelial barrier. After aspiration of the cell culture medium from the reservoirs on the chip, FITC-dextran solution was briefly added (~5 µL) at one fluidic channel to perfuse the intraluminal space, which was soon followed by the equilibrium

of hydrostatic pressure between two fluidic channels. Fluorescence images were obtained every 5 s for 40 s with an IX81 inverted microscope (Olympus) and a CCD camera (Andor) using a 40× objective. To minimize the compounding influences of complexities and randomness in the microvascular networks, we chose the region of a network where the segment of a blood vessel with a clear boundary between the endothelial wall and the extravascular fibrin matrix could be monitored exclusively in an optical window.

We calculated the permeability coefficient by using a method described elsewhere [36]. In brief, the permeability coefficient can be calculated as below assuming that the cross-sectional shape of the blood vessels is circular:

$$P = \frac{V}{S} \times \frac{dI/dt}{I_0}$$

where  $V$  and  $S$  are the total volume and surface area of the microvessels that fluorescent molecules have to pass to reach the perivascular region.  $I_0$  is the intravascular intensity of FITC-dextran,  $dI/dt$  is the total fluorescence intensity change per unit time in the perivascular region. During the fluorescent imaging, the fluorescent intensity at the intravascular region ( $I_0$ ) was not changed. The fluorescent images were analyzed with ImageJ (NIH).

### **2.2.9. Inflammatory response and HL-60 adhesion experiments**

Microvascular networks derived from angiogenic sprouts at days 4–5 were stimulated for 4 h with 50 ng/mL of recombinant human TNF- $\alpha$  (PeproTech) or with 2 ng/mL of recombinant human IL-1 $\alpha$  (PeproTech). Then these networks were perfused with fresh EGM-2 medium, and labeled with CellTracker Red (5  $\mu$ M, Molecular Probes) according

to the manufacturer's instructions. Differentiated HL-60 cells were fluorescently labeled with CellTracker Green (5  $\mu$ M, Molecular Probes), and then resuspended in fresh EGM-2 medium at a concentration of  $1.5 \times 10^6$  cells/mL. To introduce the cells into the microvascular networks, all four reservoirs of the microfluidic chips were aspirated, and then 20  $\mu$ L of the cell suspension loaded into a single inlet reservoir allowing the cells to flow into and adhere onto the apical surface of endothelium. The vascular networks were washed once with fresh EGM-2 to remove non-adherent cells, followed by filling the reservoirs with fresh EGM-2 medium.

#### **2.2.10. Fluid perfusion experiments and statistical analysis of endothelial NO synthesis**

The microfluidic chips designed for angiogenesis experiments were modified to enable constant medium flow to be introduced into the microvascular networks formed within a chip, as schematically presented in Fig 2.1. Except for the flow-introducing serpentine channel network replacing the LO channel, the channel dimensions and experimental procedures for angiogenic sprouting were identical to those described in the above sections.

To estimate the flow rate that exerts a physiological level of shear stress, we assumed the microvascular networks as a multi-pipe system of parallel flow cases where each vessel has a circular cross-sectional shape and an identical length. According to our assumptions, the head loss of each vessel across the vascular network is identical, thus the flow rate at each blood vessel is calculated as follows:

$$h_f \propto \frac{Q_k}{A_k^2}$$

$$\frac{Q_1}{A_1^2} = \frac{Q_2}{A_2^2} = \dots = \frac{Q_n}{A_n^2} = \frac{\sum_{k=1}^{k=n} Q_k}{A_1^2 + A_2^2 + \dots + A_n^2} = \frac{Q_{total}}{A_1^2 + A_2^2 + \dots + A_n^2}$$

$$Q_k = Q_{total} \left( \frac{A_k^2}{A_1^2 + A_2^2 + \dots + A_n^2} \right)$$

where  $h_f$  is the head loss across the microvascular network,  $Q_k$  is the volume flow rate at the  $k$ -th vessel,  $A_k$  is the cross-sectional area of the  $k$ -th vessel, and  $Q_{total}$  is the total volume flow rate which is the sum of the individual flows.

For a blood vessel with a diameter  $r$  and a volume flow rate  $Q$ , the shear stress can be calculated according to the following equation:

$$\tau = \frac{4Q\mu}{\pi r^3}$$

where  $\mu$  is the viscosity of the perfusate, which is the cell culture medium having a viscosity value of 0.0008 Pa·s in our experiments.

From the confocal microscopic images of 7 microfluidic chips, we quantified the diameter of vessels along the centerline of the microvascular networks. To match the physiological level of wall shear stress observed in venular microvessels *in vivo* (<10 dyne cm<sup>-2</sup>), we determined the total volume flow rate for our microvascular networks (average vessel diameter of 35.7 ± 17.6 μm, s.d.) to be 300 μL h<sup>-1</sup>, which is estimated to exert 0.31–7.22 dyne cm<sup>-2</sup> (2.34 dyne cm<sup>-2</sup> in average) of shear stress for each vessel depending on its diameter.

At day 5 of the sprouting angiogenesis process, the microvascular networks were

perfused with the cell culture medium, EGM-2 via a syringe pump connected to an inlet of the microfluidic chip with the flow rate denoted above. Before each experiment, the microvascular networks were examined by microscopic observation to assess whether the vessel density and the diameter fit into the range of average values, and the vessels readily allowed fluid perfusion. In the experiments for quantifying the nitric oxide synthesis of the endothelial cells, the perfusates were supplemented with L-arginine (5 mM, Sigma) and DAF-FM DA (5  $\mu$ M, Molecular Probes), to support and detect the NO synthesis of ECs.

After the fluid perfusion, the cytoskeleton reorganization and NO synthesis of ECs were accessed via confocal micrographs, using fluorescence signals derived from Alexa Fluor®488-Phalloidin and DAF-FM DA. Captured images were further analyzed with IMARIS (Bitplane). To quantify and compare NO synthesis between static and flow conditions from the images, the background fluorescence of each image was eliminated by subtracting the average intensity per pixel obtained from the regions where the vessels are absent. Z-projections of each 3D stack were collected via IMARIS, and ImageJ was used to obtain average intensity values for each pixel from the Z-projections. A one-tailed, unpaired Student's t-test was used to test for statistical significance between the groups.

#### **2.2.11. Quantification of vessel area and length of sprouts**

To quantify the vascular area coverage during vasculogenic blood vessel formation, cells were fluorescently labeled with CellTracker green, and fixed with 4% paraformaldehyde to be imaged by confocal microscope. Z-projections of the 3D stacks of microvascular networks were obtained each day with IMARIS (Bitplane), and further

analyzed with ImageJ (NIH) to obtain binary images and calculate the proportion of the fluorescent pixels within the ROI of each image, deriving the vascular area coverage in the central channels for 4 days of vessel growth.

For the quantification of angiogenic sprout growth, DIC images of the central channel of each chip were obtained by Olympus IX81 microscope during 4 days of sprout growth. The lengths of the sprouts were determined by manually measuring distances between the original gel interface and the tip of each sprout.

## **2.3. Results**

### **2.3.1. Microfluidic chip and experimental design**

We fabricated the microfluidic chip using standard photolithography and soft lithography techniques. To complete the chip, a molded piece of PDMS (polydimethylsiloxane) with embedded channel structures was bonded to a glass coverslip (Fig 2.1A). The chip consists of five parallel channels: a central channel (C) and two stromal cell culture channels (LO, RO), separated by two fluidic channels (LI, RI) (Fig 2.1B). The channels are partitioned by microposts whose geometry and dimensions are configured to allow the surface-tension-assisted patterning of ECM [37], cells and culture medium into the designated microchannels. Spatially patterned co-culture of ECs (in C channel) and stromal cells (in LO or RO channels) supports diffusion-dependent, but contact-independent, heterotypic cell–cell communication, which allows the progression of two distinct processes of blood vessel formation, vasculogenesis and angiogenesis, to be replicated in a single versatile platform (Fig. 2.1C–F).

Using a common platform design, we optimized the dimensions of the central channel and the microposts for each blood vessel forming process (Fig 2.2A, B). Vasculogenesis experiments were performed in chips with 1000  $\mu\text{m}$  wide and 250  $\mu\text{m}$  high central channels. Angiogenesis experiments were performed in chips with 700  $\mu\text{m}$  wide and 100  $\mu\text{m}$  high central channels. The openings between posts at the interface of the central channel and the fluidic channel serve as a route for the paracrine interactions between ECs and stromal cells during the vessel formation. These can also be used to access the intraluminal side of microvascular networks after the perfusion was established.

### **2.3.2. Formation of vasculogenesis- and angiogenesis-derived microvascular networks**

We monitored the growth of the primary vessel network and angiogenic sprouts as it occurred over several days. We used human umbilical vein endothelial cells (HUVECs) as vascular precursor cells, and human normal lung fibroblasts (LFs) as stromal cells to support HUVEC morphogenesis via secretion of pro-angiogenic growth factors and extracellular matrix proteins [38, 39]. To recreate highly pro-angiogenic ECM environments as found in wound healing and solid tumors [40], we supplemented fibrin matrix with type I collagen (referred to simply as “fibrin matrix” hereafter) to form ECM constructs.

Vascular networks resembling primary plexus spontaneously emerged within the central channel (C) from HUVECs embedded in fibrin matrix, supported by soluble factors secreted by LFs cultured in separate flanking channels (LO, RO) (Fig. 1C). A day after seeding, HUVECs displayed elongated morphology with appearance of

intracellular vacuoles (Fig 2.3A). Assembly of HUVECs into tubule-like structures encompassing a nascent lumen was observed as early as day 2 (Fig 2.3B). Further development of the vasculature resulted in interconnected networks occupying extended areas of fibrin matrix after 3 days (Fig 2.3C). Perfusable microvascular networks that can be directly accessed via fluidic channels were established by day 4 to 5, followed by the enlargement of lumina (Fig 2.3D). Initial cell density of HUVECs influenced the resulting vessel density as quantified in Fig 2.3I.

We found that vasculogenic morphogenesis of HUVECs was dependent on the co-culture with LFs, since HUVECs without co-cultured LFs failed to form interconnected networks (Fig 2.4). A mixed co-culture of HUVECs and LFs in the central channel also formed well-interconnected vascular networks after 5 days (Fig 2.4B). However, these networks were not connected to the medium channels (LI and LO) and could not be perfused (Fig 2.4D). This result was in sharp contrast to open networks when LFs were cultured in separate flanking channels (Fig 2.4C).

To induce angiogenic sprouting, we seeded HUVECs on the left side-wall of the acellular fibrin matrix that filled the central channel. LFs were positioned on the opposite side in the RO channel, exposing HUVECs to a gradient of LF-secreted factors (Fig 2.1E). Within 24 h of co-culture, we observed robust formation of tip cells and angiogenic sprouts along the openings of the central channel (Fig 2.3E). Once the sprouting had been initiated, the tip cells guided the growth of sprouts across the fibrin matrix until they reached the opposite end of the channel, as quantified in Fig. 2.3J. The growth of sprouts was supported by the proliferating cells at the stalk region showing sharp contrast with the non-proliferating tip cells (Fig 2.5A), which is in concordance

with a previous study demonstrating distinct EC phenotypes during sprouting angiogenesis *in vivo* [41]. By day 2, endothelial cells comprising tubular structures were vacuolated (Fig 2.3F). Defined lumina around the stalk region appeared by day 3 (Fig 2.3G). The leading tip cells traversed the 700  $\mu\text{m}$  wide central channel by day 4, after which they lost their filopoidal structures, and formed lumenized vessels to establish fluidic connections with the flanking medium channels (Fig 2.3H). Culturing HUVECs without LFs or seeding LFs ipsilateral (LO channel) to HUVECs failed to induce robust angiogenic sprout formation and growth (Fig 2.5B, C), indicating that angiogenic sprouting requires an appropriate directional gradient of pro-angiogenic factors secreted by LFs.

To test whether soluble VEGF directs angiogenic sprouting in our chip, we applied gradients of VEGF (0–50 ng/mL) across the fibrin matrix. This treatment induced initial steps of angiogenic sprouting as shown by robust tip cell formation, but the sustained length extension and lumenization of sprouts was not as evident as with LF-induced sprouting (Fig 2.5D).

### **2.3.3. Morphological and biochemical characterization of the vessels**

To test whether the engineered blood vessels exhibit physiological characteristics, we tested the vessels for their 3D structural integrity and the presence of characteristic marker proteins of intact blood vessels. Immunofluorescence micrographs of the microvascular network formed through vasculogenesis (Fig 2.6A) and angiogenesis (Fig 2.6B) exhibited the complex inter-connectiveness and bifurcated architecture found in native vasculatures. Micrographs of angiogenic sprouts grown for 2 days (Fig 2.6C) with a high magnification image of angiogenic tip cells (Fig 2.6D) clearly display a

characteristic migratory morphology with multiple filopodia extensions at the sprouting fronts. Moreover, cross-sectional images of blood vessels (Fig 2.7A-C) showed the presence of a continuous, hollow lumen along the length of the vessels, enclosed by ECs. We also found continuous cell–cell junctions lining the intersection of the endothelial cells, as shown by the presence of the adherens junction proteins, VE-Cadherin and  $\beta$ -catenin, and tight junction protein, ZO-1 (Fig 2.7D, E). Notably, these endothelial cells display the morphological features of venular microvessels found *in vivo* [42], such as an elongated morphology aligned with the longitudinal direction of capillary-like structures. This is in sharp contrast to the randomly-aligned morphology exhibited by EC monolayers grown on 2D substrates, or ECs comprising endothelialized 3D hydrogel channels [12, 26, 28].

We then analyzed the cells for signs of vessel maturation. First, using immunofluorescence to detect the apical expression of TNF- $\alpha$ -induced ICAM-1 and the basal deposition of collagen IV, we confirmed the appropriate apical–basal polarity of the endothelium (Fig 2.7F). Through the vessels stained for laminin and collagen IV, we also observed the deposition of basement membrane by endothelial cells around the perivascular extracellular matrix, a sign of vessel maturation associated with mural cell association and vascular stabilization (Fig 2.7G, H) [43].

#### **2.3.4. Perfusable and intact lumina of the engineered microvascular networks**

We next tested whether the microvascular networks grown in the microfluidic chip provide 3D intact perfusable vessels with the practical potential to investigate flow-mediated endothelial mechanotransduction, vascular barrier function and endothelium–leukocyte interactions.

To demonstrate the direct fluid interconnection between the medium channels and the endothelial lumina, we introduced solutions containing fluorescent polystyrene microbeads into the microvascular networks along with the luminal flow induced by hydrostatic pressure differential. A minute volume difference in the reservoirs (~20  $\mu\text{L}$ ) established fluid flow through the vessels in the central channel, allowing the passage of 7  $\mu\text{m}$  polystyrene beads, whose dimension is comparable to the blood-borne cell types (Fig 2.8A). As visualized by the movement of the tracer beads, the microvascular networks allowed fluid flow through the lumina without bead infiltration into the abluminal fibrin matrix. Solutions containing FITC-dextran (70 kDa) were also introduced into the vessels that were labeled with CellTracker red (Fig 2.8B), exhibiting clear retention of FITC-dextran inside the vessels without uncontrolled leakage into perivascular space. Quantitative assessment of angiogenesis-derived blood vessels revealed that the permeability coefficient of 70 kDa FITC-dextran through the endothelial walls measured to be  $(1.70 \pm 0.36) \times 10^{-6} \text{ cm s}^{-1}$  ( $n = 3$ ) at 4–5 days. This permeability coefficient illustrated an intact, stronger barrier function of our vessels, which is closer to that of *in vivo* venular vessels [44], when compared to the other *in vitro* vessels reported previously [12, 26, 45].

To test the robustness of our method, we quantified the success rate of perfusable network formation by flowing microbeads through the lumina of blood vessels. We found that 88% ( $n = 36$  chips, 4 trials) and 91% ( $n = 36$  chips, 4 trials) chips successfully established perfusable networks via vasculogenic and angiogenic processes, respectively. Within the successful devices, the percentages of interpost regions encompassing the openings were 62% and 70% for the vasculogenic and angiogenic

process. These microvascular networks maintained patent and perfusable lumina for at least an additional 7 days without discernible regression or destabilization (Fig 2.9A, B).

### **2.3.5. Flow-induced endothelial responses**

As an innermost cellular layer of blood vessels, the endothelium is constantly exposed to mechanical stimuli exerted by blood flow. Rather than being passive pipelines, blood vessels faithfully respond to the mechanical stimuli, contributing to the structural integrity and normal functions of blood vessels, and in turn, abnormal blood flow or vessel occlusion leads to the pathogenesis of diverse diseases [46, 47].

To examine whether constant fluid flow through the *in vitro* 3D blood vessels evokes endothelial responses and functional upregulation, we examined the cytoskeleton reorganization of ECs and nitric oxide (NO) synthesis in response to fluid flow. To estimate the flow rate necessary to approximately match the physiological level of shear stress (1 to 10 dyne/cm<sup>2</sup> in venular microvessels [48]), we considered the range of diameters of blood vessels derived from the angiogenesis experiments ( $35.7 \pm 17.6 \mu\text{m}$ , s.d, 87 vessels from 7 chips, Fig 2.10). The volume flow rate for the entire vessel network was  $300 \mu\text{L h}^{-1}$ , which established the range of shear stress at approximately 0.31–7.22 dyne/cm<sup>2</sup>, depending on the size of each microvessel. For long-term perfusion of the microvessels with constant volumetric flow rate, the chip design was modified to have a fluidic inlet and serpentine channel network replacing the LO channel (Fig 2.2C).

We found that under such conditions, fluid flow induced cytoskeleton reorganization of the ECs comprising the microvascular networks which showed distinct distribution of F-actin microfilaments compared to static conditions. In the absence of fluid flow, dense

F-actin bundles preferentially localized at the periphery of endothelial cells where the cell–cell contacts were present (Fig 2.11A). In contrast, ECs exposed to fluid flow for 2 h displayed evenly distributed stress fibers that are parallel and aligned in the direction of the fluid flow. The peripheral band seen in static conditions was not discernible (Fig 2.11B).

We next examined the effect of fluid flow in the functional upregulation of blood vessels through the synthesis of nitric oxide, a crucial and multifunctional signaling molecule for vascular physiology. Flow-mediated shear stress is a key determinant of activation of endothelial NO synthesis [49], which exerts a wide range of effects including modulation of blood flow, anti-thrombotic, anti-inflammatory and anti-proliferative functions [50]. To examine the effect of fluid flow in activation of endothelial NO synthesis in our chip, we perfused angiogenesis-derived microvascular networks with cell culture medium adding L-arginine as a precursor for NO synthesis (5 mM), and the NO-reactive fluorescent dye DAF-FM DA (5  $\mu$ M). Under static conditions, the endothelial synthesis of nitric oxide induced only a low level fluorescence signal even in the presence of high concentrations of L-arginine (5 mM), a physiological precursor for the NO synthesis (Fig 2.12D). However, microvascular networks perfused for only one hour exhibited a significant increase in the NO-reactive fluorescence signal, sufficient to observe the outline of the endothelium (Fig. 2.12E, F). We also observed that flow-mediated upregulation of NO synthesis required exogenous L-arginine in the perfusate [51], as perfusion of the medium without a L-arginine supplement did not increase the endothelial NO synthesis compared with static conditions (Fig 2.12 A-C).

### **2.3.6. *In vitro* modeling of endothelial interactions with pericytes, cancer cells and leukocytes**

Endothelial cells receive and integrate diverse signals from nearby microenvironments and other cell types to accommodate tissue-specific functions or to control angiogenic switch [52-54]. To investigate whether our chip can reproduce vessel growth and responses via interactions with diverse cell types, we performed co-culture experiments with pericytes and cancer cells.

To simulate pericyte recruitment from interstitial tissue toward newly formed angiogenic sprouts, we incorporated human placenta pericytes in the fibrin matrix filling the central channel, whereby LF-induced angiogenic sprouts extended across the ECM embedding the pericytes. The presence of pericytes in the central channel did not disturb the growth of angiogenic sprouts to form perfusable microvascular networks, both in the timescale of sprout length extension and the establishment of perfusable lumina (~88%, n = 33 chips, 3 trials). By day 4, pericytes expressing  $\alpha$ -smooth muscle actin ( $\alpha$ -SMA) were frequently found adjacent to the blood vessels with stretched morphology to cover abluminal surface of the endothelium (Fig 2.13A). A high magnification image and the corresponding confocal sections showed pericytes attached to the endothelial-derived collagen IV basement membrane (Fig 2.13B).

We then explored whether, in our chip-based microvasculature, cancer cell-secreted factors support the initiation and growth of angiogenic sprouts. We co-cultured HUVECs with highly malignant human glioblastoma multiforme cells, U87MG, seeded in the stromal cell culture channel (RO). We found that within 24 h of co-culture, HUVECs invaded the fibrin matrix apparently in response to the U87MG-derived

factors. Whereas the sustained outgrowth of sprouts exhibited similar length extension (day 2:  $341.0 \pm 18.7 \mu\text{m}$ , day 4:  $620.3 \pm 5.2 \mu\text{m}$ , mean of average sprout length from 4 chips per day, error represents SEM) compared to LF-mediated sprouting experiments, these sprouts displayed aberrant morphology. At day 2, the angiogenic sprouts showed frequent branching of the immature tubules, as shown by multiple tip cells at the distal edges of sprouts (Fig 2.13C). And rather than growing directionally toward U87MG cells, some sprouts were convoluted and aberrantly fused with adjacent vessels resembling the vasculatures of corresponding *in vivo* scenarios [55]. When compared to LF-induced sprouts, U87MG-induced sprouts exhibit inefficient formation of perfusable vascular networks at day 4, frequently encompassing immature and poorly lumenized vessels (Fig 2.13D).

The interactions between the endothelium and white blood cells play a central role in immunity [56], which prompted us to examine whether the microvascular networks exhibit appropriate functions in the presence of pro-inflammatory cytokines. We therefore tested, in our system, endothelial responses and leukocyte adhesion after stimulation by inflammatory cytokines. The endothelium expressed a leukocyte adhesion protein, ICAM-1, on the apical surface in response to tumor necrosis factor- $\alpha$  (TNF- $\alpha$ , 50 ng/mL) or interleukin-1 $\alpha$  (IL-1 $\alpha$ , 2 ng/mL) (Fig 2.13E). The endothelium stimulated with TNF- $\alpha$  promoted the adhesion of differentiated HL-60 cells which were introduced along with the transient luminal flow. Upon arrest, the HL-60 cells adopted a flattened morphology and actively crawled on the apical surface of the endothelium (Fig 2.13F), simulating the adhesive interactions between leukocytes and the endothelium found in inflammatory responses.

## 2.4. Discussion

Despite the significant progress, it has not yet been possible to reconstitute the characteristic functions and responses of blood vessels with their natural 3D architectures. The artifacts shown in the previous studies mainly stem from their limited ability to combine physiological vessel forming processes and luminal flow which contribute typical structural and functional features of blood vessels. While recent studies have demonstrated the feasibility to achieve perfusable blood vessels by mimicking physiological angiogenic processes [31, 34], these methods still depend on the artificial structural guides in shaping outlines of the vasculatures. Furthermore the behaviors of endothelial cells observed in these methods were deviated from those shown in actual vasculogenesis and angiogenesis processes, leading to compromised vascular functions. In particular, the integrity of barrier function and mechanosensitive responses should be confirmed to further exploit 3D blood vessel models in the investigations of transendothelial migration or endothelial mechanotransduction which still rely on 2D endothelial monolayers. The method presented in this study conveys key advantages as it not only closely mimics endothelial morphogenesis processes to form intact, perfusable microvascular networks, but also recreates important vessel-specific functions defined by luminal flow.

Our spatially patterned co-culture approach provides a reliable mimicry of a living system, whereby tightly coordinated crosstalk between ECs and perivascular or stromal cell types precisely control the formation and function of blood vessels. In accordance with earlier *in vivo* and *in vitro* studies [35, 57], we demonstrated that the multistep cascade of the angiogenic process cannot be fully reproduced by addition of a potent

pro-angiogenic factor, such as VEGF, on the monoculture of endothelial cells, whereas EC–fibroblast interaction robustly induced lumenized vessel formation. Moreover, the versatile capabilities of our patterned co-culture approach allowed diverse types of cell–cell interactions to be modeled in a single platform, which effectively reproduced tumor-induced angiogenesis (in the co-culture of ECs and U87MG cells) as well as endothelial–pericyte interactions (in the tri-culture of ECs, fibroblasts and pericytes). The cellular compositions in the culture can be further flexibly configured to confer increased biological relevance as well as organ- and microenvironment-specific characteristics to the vessels.

The exact mechanisms by which growing tubules form accessible inlets at the ECM–fluid interface remain unclear and require further investigation. However, we speculate that the chemotactic gradient of fibroblast-secreted factors drives spontaneous anastomotic fusion observed in our chip. In our results, both vasculogenic and angiogenic processes require LF-secreted factors. In contrast to the angiogenic sprouting, vasculogenic processes do not necessarily require LF-secreted factors to be present in a form of concentration gradient. However, interestingly, a mixed co-culture of ECs and fibroblasts resulted in well-interconnected but non-perfusable (or poorly perfusable at best) vascular networks, where the tubules rarely extended toward the ECM-fluid interfaces at the apertures (Fig 2.4). Although we do not suggest mechanisms underlying this observation as well as relevant *in vivo* phenomenon, spontaneous formation of open lumina by growing endothelial tubules provide a novel methodology to establish perfusable vasculatures in a 3D cell culture system.

The processes of new blood vessel formation require the establishment of functional

vascular loop to prompt the survival and stabilization of newly formed vessels [58], as well as physiological function and homeostasis [59]. Not only were the microvascular networks formed in our chip patent and durable, they also responded faithfully to the fluid flow displaying cytoskeleton reorganization and activation of NO synthesis. Considering multifunctional vascular regulations of NO, enhanced NO production suggests that the mechanical forces exerted by the fluid flow contribute as determinants to the functional behaviors of our endothelium as in the coincidence with living vasculatures transmitting the fluid. Notably, flow-mediated F-actin reorganization of ECs was observed even briefly after 2 h of fluid perfusion. Whereas the reorientation of cell bodies into the fluid direction precedes the F-actin reorganization in endothelial monolayers on 2D substrates [60], ECs forming 3D microvessels in our chip displayed well-aligned cellular patterns along the longitudinal axis of the tubules, even in a static, pre-sheared condition, which might contribute to our observations.

The vasculatures formed in our chip displayed intact barrier function as well as long-term stability. These attributes provide benefits for the investigation of how vascular integrity can be either augmented or compromised in response to microenvironmental cues. Examples would include the presence of physiological flow and pericyte coverage for their regulations in the vascular physiology/homeostasis. Our system also allows the study of microvascular occlusion and hyper-permeability observed during diverse diseases such as cancer, infection with malaria and diabetic retinopathy, to name a few.

## **2.5. Conclusions**

Given the primary functions of blood vessels as mechanosensitive and selective barrier

between flowing blood compounds and interstitial tissues, there is a pressing need for a robust and practical approach that can combine physiological formation of 3D blood vessels with perfusable and stable lumina, whereby key microenvironmental factors can be integrated within an *in vitro* model that more closely resembles the *in vivo* state of tubular vessels transmitting fluid flow.

Here we report a robust experimental platform for studying the formation and function of 3D blood vessels in response to critical microenvironmental factors. Our microfluidic chip employs spatially controlled co-cultures of blood vessel-relevant cell types, which comes closer to reconstituting the heterotypic cell–cell interactions found in healthy and pathologic scenarios. A major advance of our approach is the ability to grow perfusable microvascular networks that are similar in 3D architectures, intact barrier function, long term stability and salient biochemical markers to their *in vivo* counterparts. This unique feature distinguishes our method from previously reported microtechnology-assisted perfusable blood vessel models, which are usually based on endothelialization of preformed hydrogel templates [12, 26, 61], or limited reconstitution of endothelial morphogenesis [14, 31, 34]. The perfusable microvessels allow further functional and structural modulations in response to biochemical and biophysical cues, and can be adapted to design unique *in vitro* models to investigate vascular barrier function, transendothelial migration of blood circulating cells, and endothelial mechanotransduction in close similarities with living systems. In addition, formation of blood vessels can involve a variety of other perivascular cell types or endothelial cells from different origins to recreate vascular microenvironments found in the blood–brain barrier, stem cell niches, and tumor metastases.

The robustness and reproducibility of our chip-based microvessels, combined with the feasibility for flexibly customizing the chip design, promise to make it a versatile platform for the fundamental study of vascular biology and vascularized micro-organs or human disease models for drug discovery.

	Reference	Measured permeability coefficient ( $10^{-6}$ cm/s)
<i>In vivo</i>	Yuan et al. <i>Microvasc. Res.</i> <b>77(2)</b> , 2009 [44]	0.15 ( $\pm$ 0.05)
<i>In vitro</i>	Kim et al. <i>Lab Chip</i> <b>13(8)</b> , 2013 [62]	1.70 ( $\pm$ 0.36)
	Zheng et al. <i>PNAS</i> <b>109(24)</b> , 2012 [12]	7 ( $\pm$ 1.5)
	Jeon et al. <i>PloS one</i> <b>8(2)</b> , 2013 [63]	3.7 ( $\pm$ 0.59)
	Zervantonakis et al. <i>PNAS</i> <b>109 (34)</b> , 2012 [30]	7.5 ( $\pm$ 0.093)
	Chrobak et al. <i>Microvasc. Res</i> <b>71(3)</b> , 2006 [26]	7.9 ( $\pm$ 3.5)

Table 2.1 Comparison of engineering-based *in vitro* blood vessel models for permeability coefficient tested using 70 kDa FITC-dextran

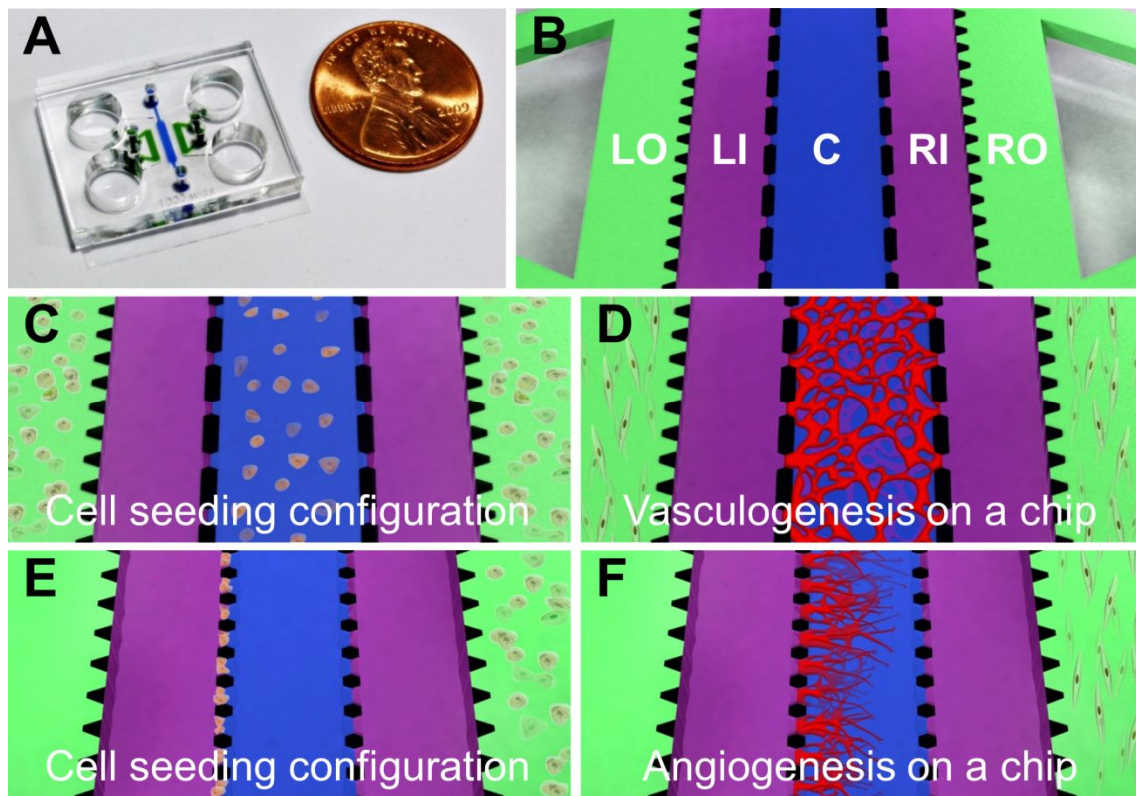


**Fig 2.1** Microfluidic chip design and cell seeding configurations for microvascular network and angiogenic sprout formation. (A) Photograph of the microfluidic chip, filled with colored fibrin matrix. (B) Schematic of the microfluidic channels partitioned by microposts. The central channel (C, blue) is flanked by two fluidic channels (Left Inside, LI, and Right Inside, RI, both colored purple) and two outside stromal cell culture channels (Left Outside, LO, and Right Outside, RO, both colored green). (C, D) Cell-seeding configuration for the vasculogenesis experiment. (E, F) Cell-seeding configuration for the angiogenesis experiment.

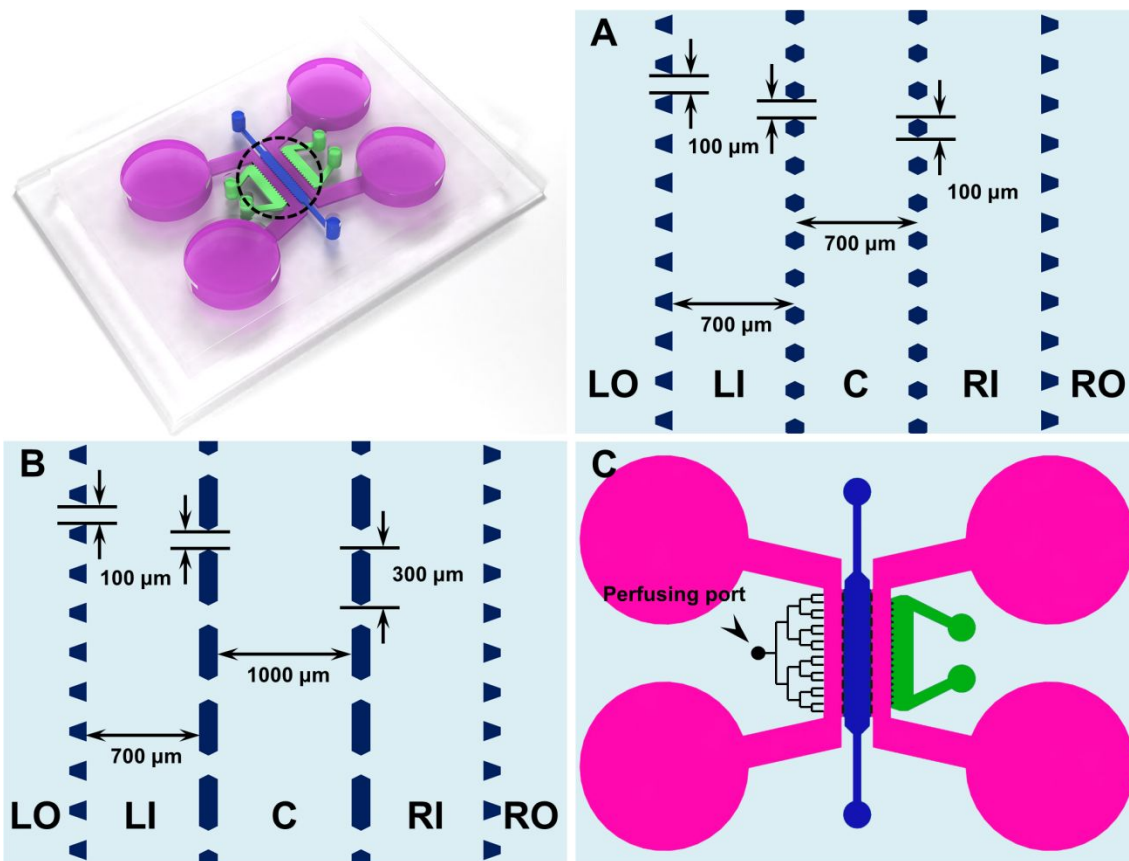


**Fig 2.2** Microfluidic chip channel configurations for vasculogenesis, angiogenesis and fluid perfusion experiments on a chip. (A) Channel configuration for vasculogenesis on a chip involves 1,000  $\mu\text{m}$  wide and 250  $\mu\text{m}$  high channel, which is partitioned with 300  $\mu\text{m}$  long hexagonal microposts spaced every 100  $\mu\text{m}$ . (B) For angiogenic sprout formation, narrower central channels, having widths of 700  $\mu\text{m}$ , were fabricated. Hexagonal microposts with 100  $\mu\text{m}$  diameter were placed to have 100  $\mu\text{m}$  interpost gaps between them. We fabricated a master with structures of 100  $\mu\text{m}$  height. (C) Modification of chip design for fluid perfusion experiment, which adds inlet for syringe pump-driven fluid flow into the angiogenesis-derived vascular networks.

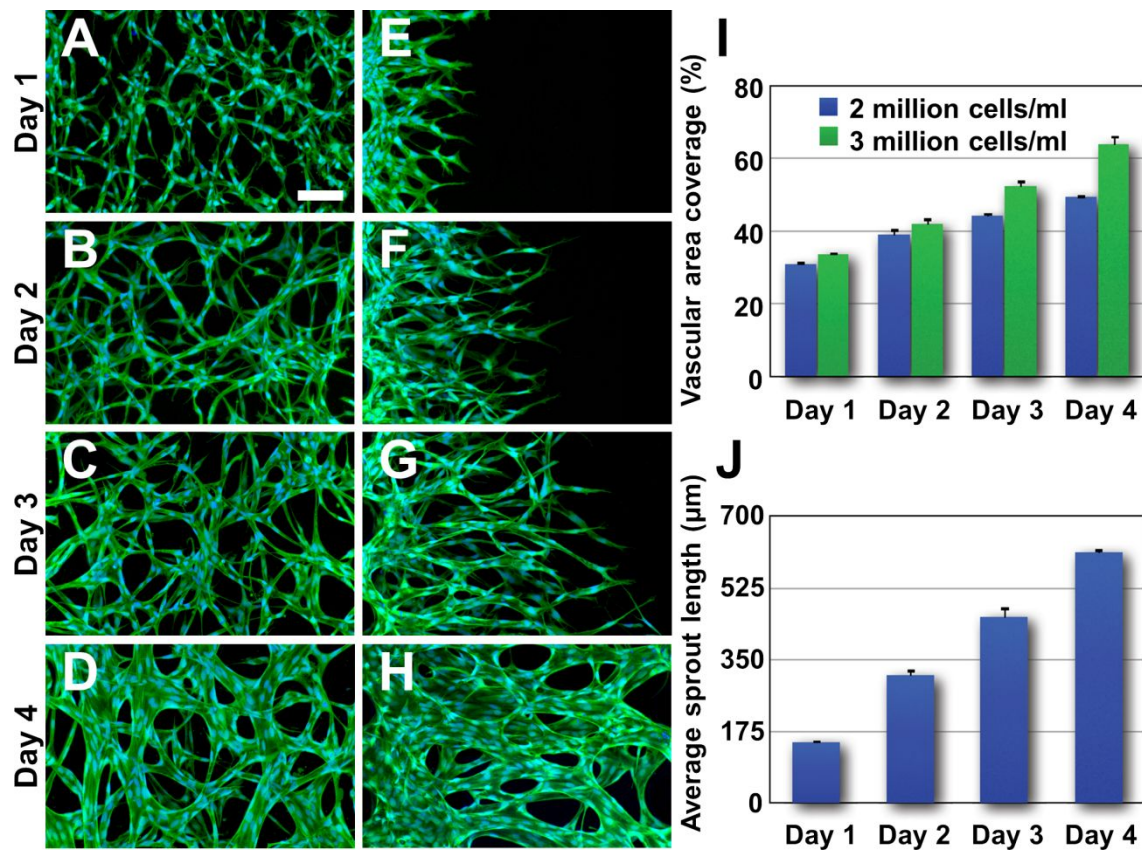


**Fig 2.3** Time-series micrographs of vasculogenic and angiogenic vessel formation in the fibrin matrix. Vasculogenesis: (A) day 1, HUVECs elongate and start to connect to each other. (B) Day 2, HUVECs start to form a network *via* a dynamic remodeling process, while nascent lumen structures appear. (C) By day 3, hollow lumina of HUVECs grow larger and merge to form well-interconnected tubular structures. (D) By day 4, a perfusable microvascular network is established as the luminal sides of the vessels are connected to the medium channels. Angiogenesis: (E) within 24 h after attaching HUVECs to fibrin walls in the central channel, endothelial sprouts with tip cells appear along the central fibrin matrix. (F) By day 2, vacuole formation starts in stalk regions. The sprouts continue to extend across the middle channel. (G) By day 3, defined lumina can be observed within the sprouts. (H) By day 4, growing angiogenic sprouts traverse

across the entire width of the 700  $\mu\text{m}$  central channel, establishing perfusion through luminal access with the RI medium channel. Cells were labeled with CellTracker green and fixed and stained for nuclei (blue). (I) Quantification of vasculogenic vessel network growth by total vascular covered area in  $z$ -projected image ( $n = 6$  chips per day per condition). (J) Quantification of angiogenic sprout growth by tip cell distance from the left side of fibrin matrix ( $n = 5$  chips for day 1, 2, 3 and  $n = 4$  chips for day 4). Scale bar, 100  $\mu\text{m}$ ; error bars represent SEM.

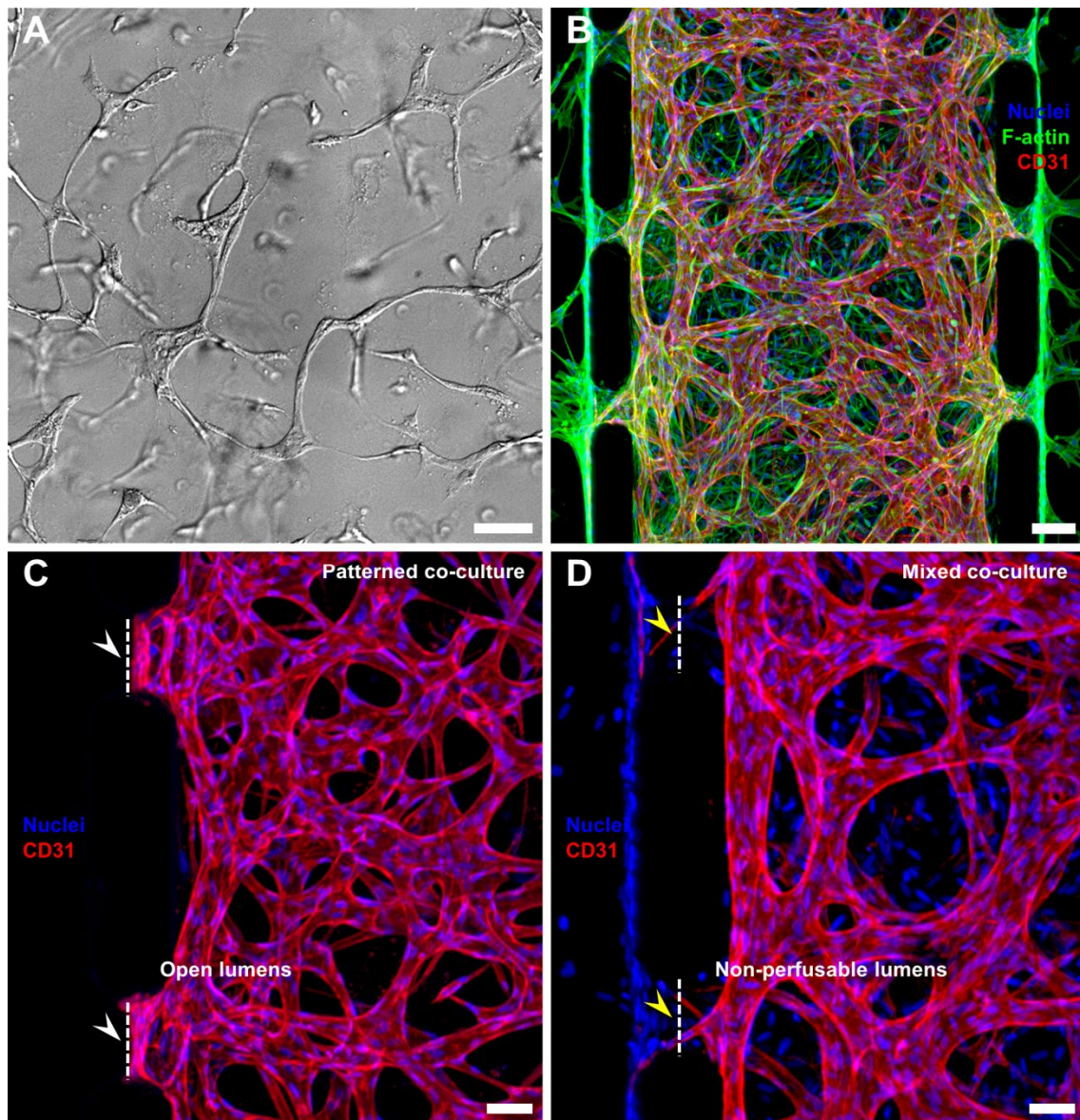


**Fig 2.4** Requirement for patterned co-culture of HUVECs and LFs in vasculogenesis on a chip. (A) HUVECs cultured for 4 days without LFs at the stromal cell culture channels(LO and RO) (B) HUVECs and LFs co-cultured within central channel forming interconnected vascular networks at day 5 with a ratio of 5 to 1 ( $3 \times 10^5$  cells/mL of HUVECs and  $6 \times 10^4$  cells/mL of LFs). (C) In a patterned co-culture condition at day 4, tubules near the interpost openings developed perfusable openings (white arrowheads) at the fibrin matrix/media interfaces (denoted as dashed line). (D) Tubules observed in a

mixed co-culture condition, grown for 5 days, rarely extended toward the interfaces, and displayed closed, non-perfusable lumens (yellow arrowheads) within fibrin matrix.

Scale bars, 100  $\mu\text{m}$ .

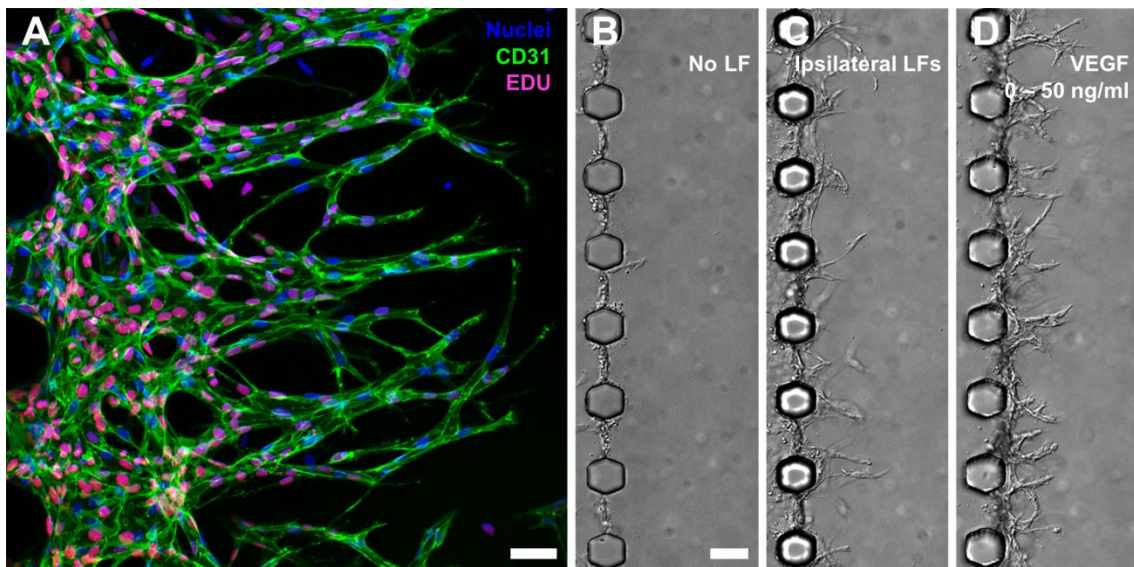


**Fig 2.5** (A) EDU proliferation assay performed for growing angiogenic sprouts revealed that most endothelial proliferation (purple nuclei) occurred at the stalk regions of sprouts, and tip cells at the fronts were characterized by non-proliferating phenotype (blue nuclei). Scale bar, 50  $\mu\text{m}$ . (B, C) HUVECs cultured without LFs or with ipsilateral LF-seeding exhibited little or no sprout formation after 3 days of culture. Scale bar, 100  $\mu\text{m}$ . (D) Angiogenic sprouts, grown for 3 days induced by VEGF gradient (0 – 50 ng/mL) exhibited relatively inefficient length extension and lumenization compared to the LF-induced sprouts.

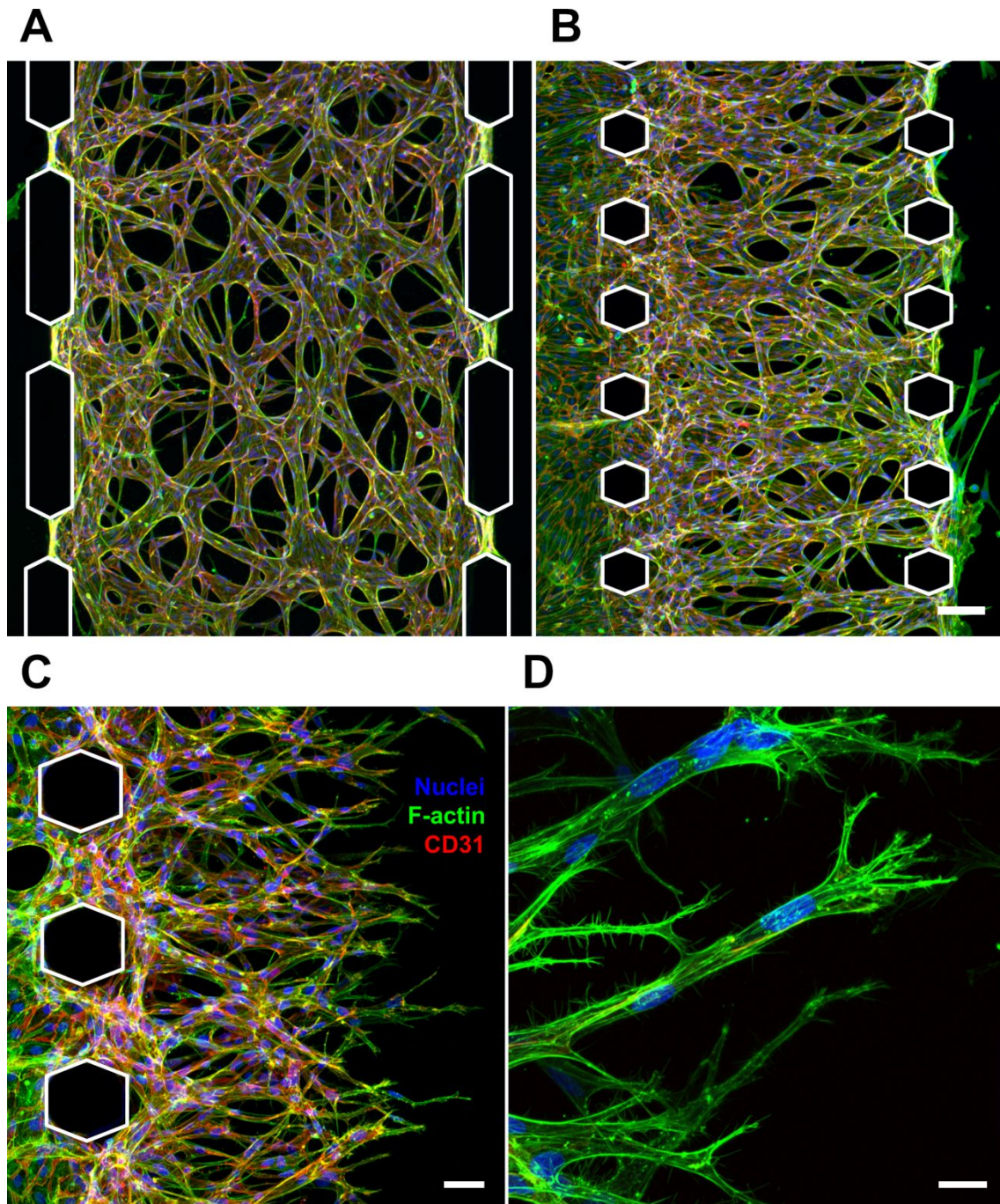


**Fig 2.6** Morphological features of engineered 3D microvessels and growing angiogenic sprouts. (A–B) Confocal micrographs showing the overall architectures of vascular networks established by (A) vasculogenic and (B) angiogenic processes at day 4. Scale bars, 100  $\mu\text{m}$ . (C) Angiogenic sprouts grown for 2 days. Scale bar, 50  $\mu\text{m}$ . (D) Higher

magnification image shows the F-actin-rich filopodia extensions of angiogenic tip cells.

Scale bar, 20  $\mu\text{m}$ .

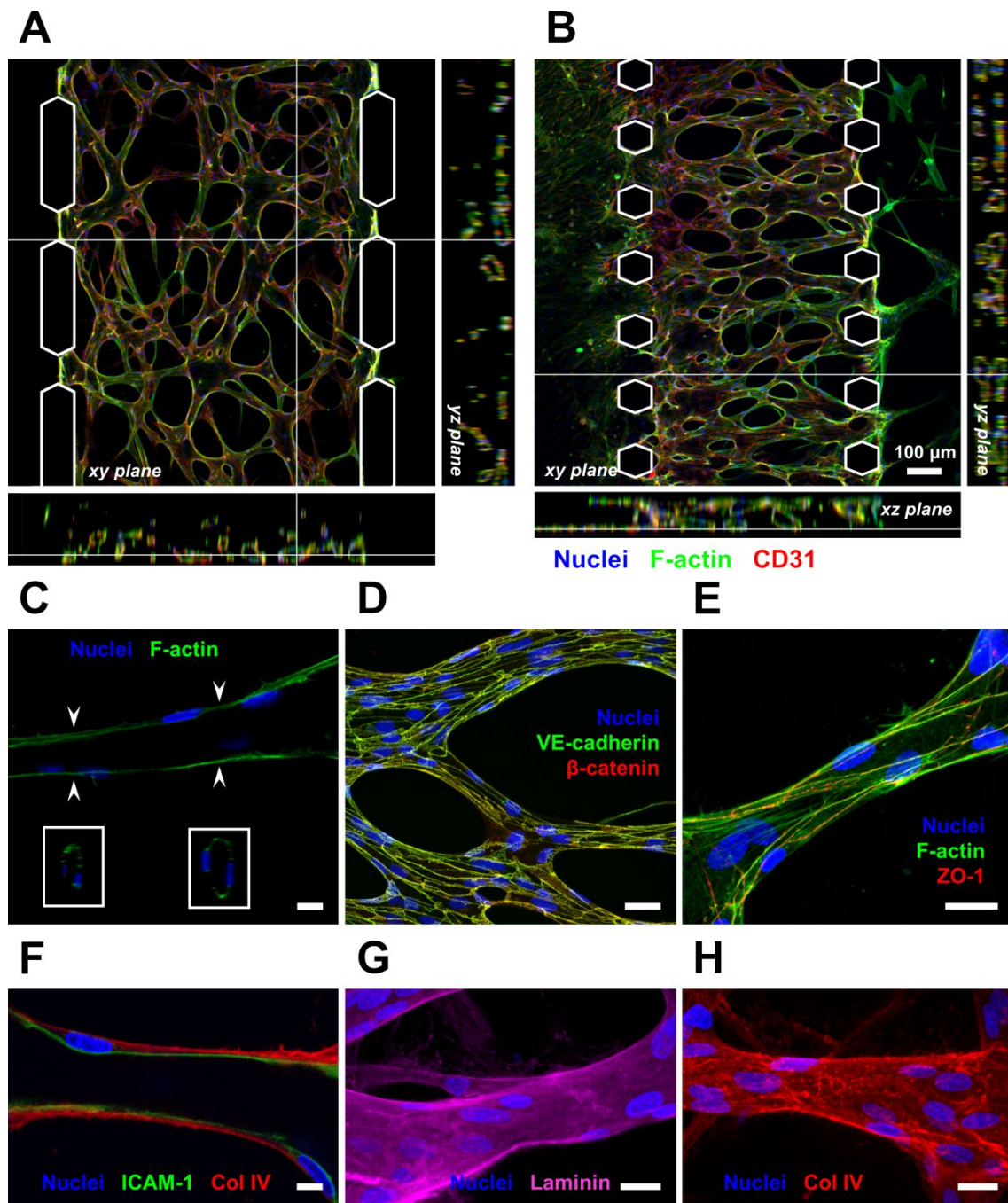


**Fig 2.7** Patency of 3D hollow lumens and biochemical characteristics of microvessels. Confocal sections of the vasculatures formed via vasculogenesis (A) and angiogenesis (B) exhibited presence of hollow lumens, forming well-interconnected networks. Scale bars, 100  $\mu\text{m}$ . (C) Cross-sectional images of a blood vessel showing a hollow lumen

enclosed by ECs. Scale bar, 10  $\mu\text{m}$ . (D) Microvascular network immunostained against adherens junction proteins, VE-cadherin (green) and  $\beta$ -catenin (red). Scale bar, 30  $\mu\text{m}$ . (E) Expression of tight junction protein ZO-1 at cell-cell contacts, displaying localization of continuous and intact intercellular connections. Scale bar, 20  $\mu\text{m}$ . (F) Longitudinal cross-section of a TNF- $\alpha$ -stimulated blood vessel stained for ICAM-1 (green) and collagen IV (red). Scale bar, 10  $\mu\text{m}$ . (G, H) Confocal micrographs of vessels stained for the major components of basement membrane, laminin (purple) or collagen IV (red). Scale bars, 20  $\mu\text{m}$ .

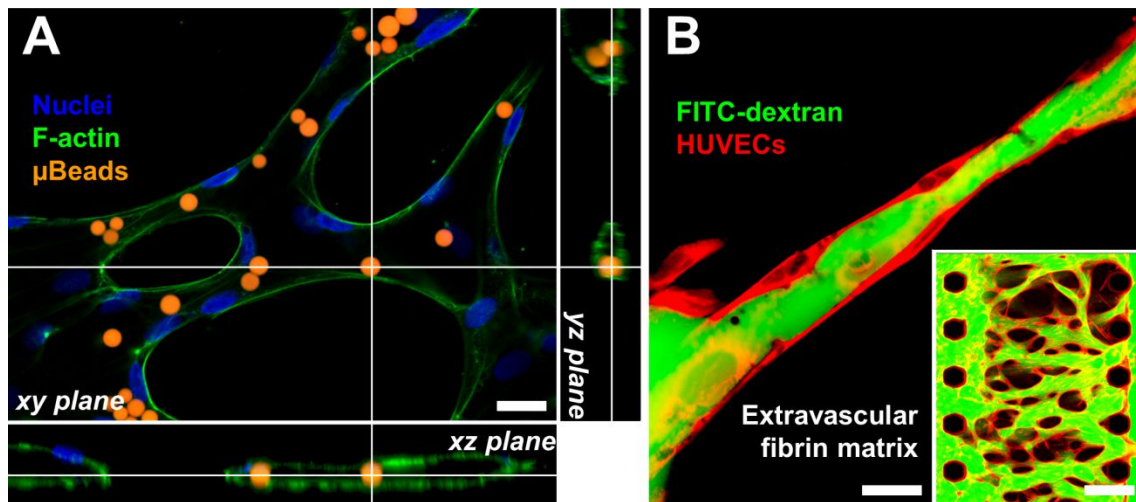


**Fig 2.8** Introduction of solutions containing microbeads or fluorescent dye into the perfusable microvessels. (A) Red fluorescent microbeads (7  $\mu\text{m}$ , red) introduced into the microvascular network exclusively localize within the luminal space of F-actin-labeled endothelium (green). (B) Intravascular introduction of FITC-dextran (70 kDa, green) into the blood vessel labeled with CellTracker red. Scale bar, 20  $\mu\text{m}$ . Inset scale bar, 200  $\mu\text{m}$ .

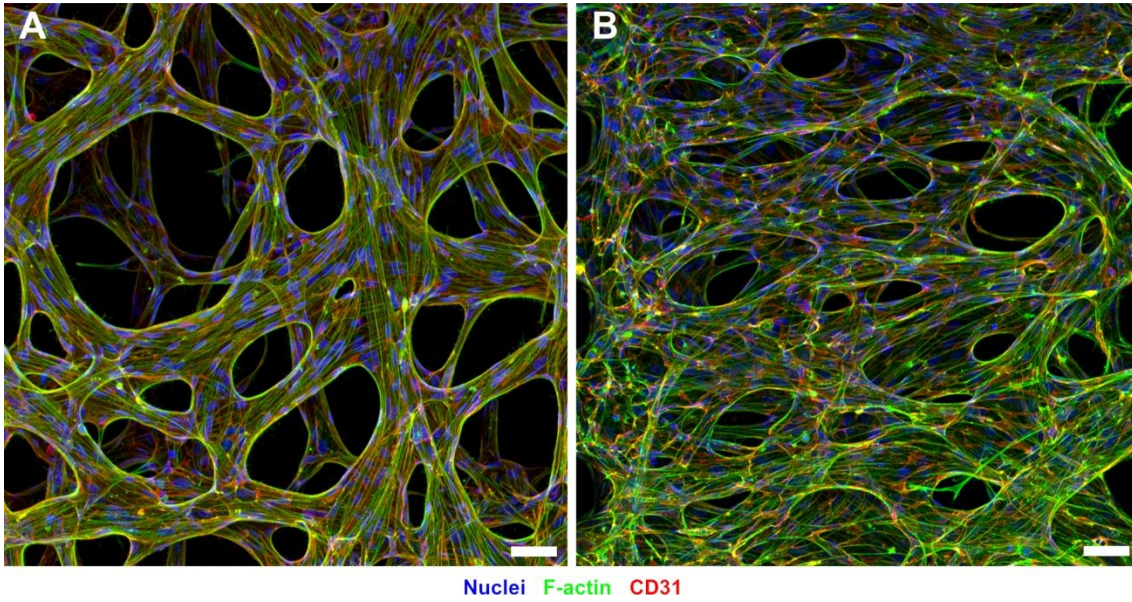


**Fig 2.9** Long-term stability of patent and perfusable lumens. Microvascular networks formed both by vasculogenesis (A) and angiogenesis (B) maintained perfusable and patent lumen for more than 7 days after perfusion had established, without discernible vessel regression or endothelial apoptosis. Scale bars, 50 μm.

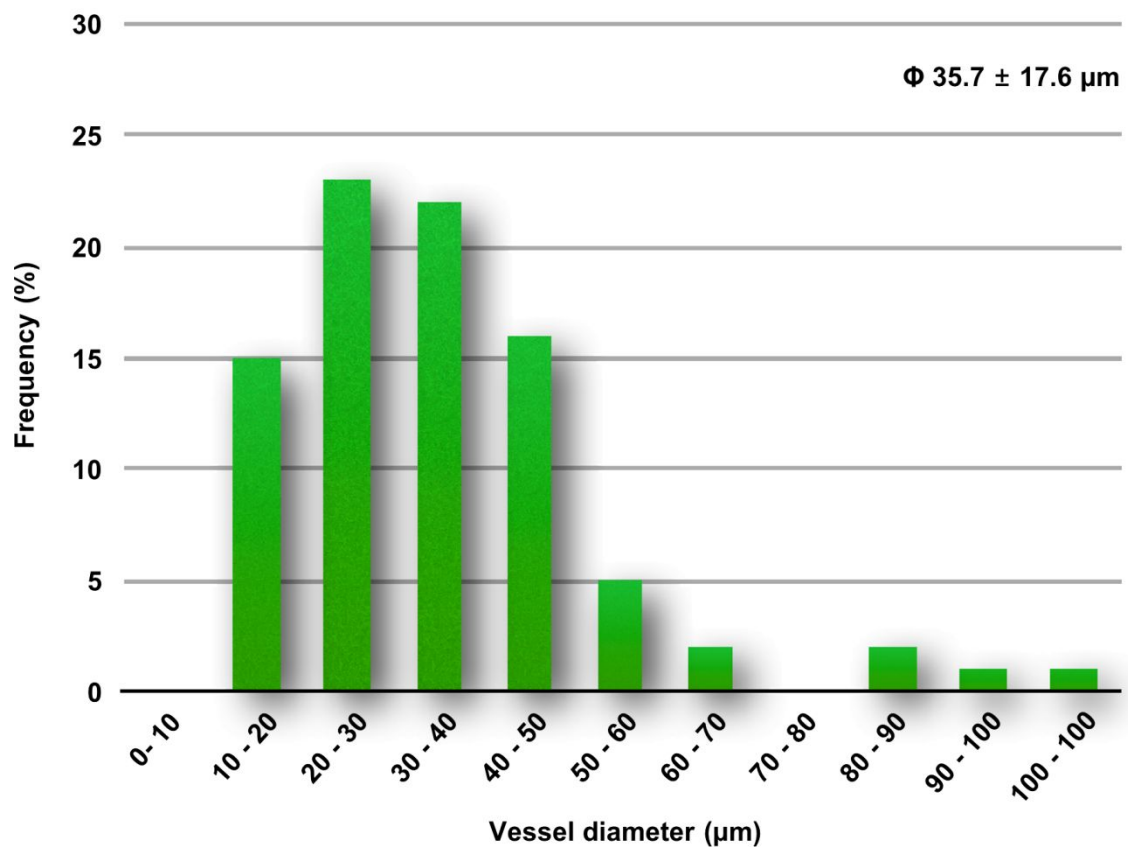


**Fig 2.10** Distribution of vessel diameter constituting perfusable microvascular network formed via angiogenic process.

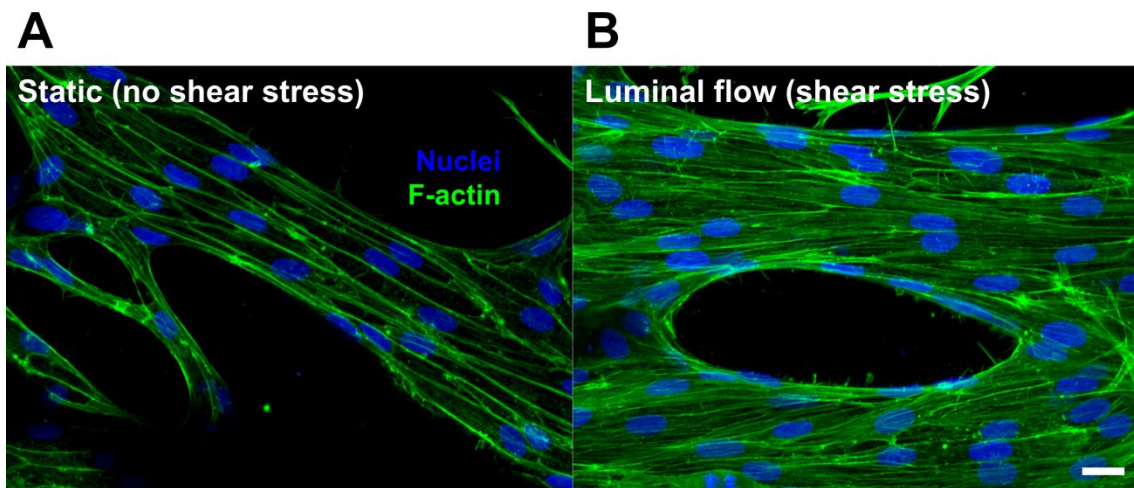


**Fig 2.11** F-actin cytoskeleton reorganization in response to luminal flow (A) F-actin (green) distribution of ECs under static conditions. Scale bar, 20  $\mu\text{m}$ . (B) Changes in F-actin distribution in response to luminal flow for 2 h. Scale bar, 20  $\mu\text{m}$ .

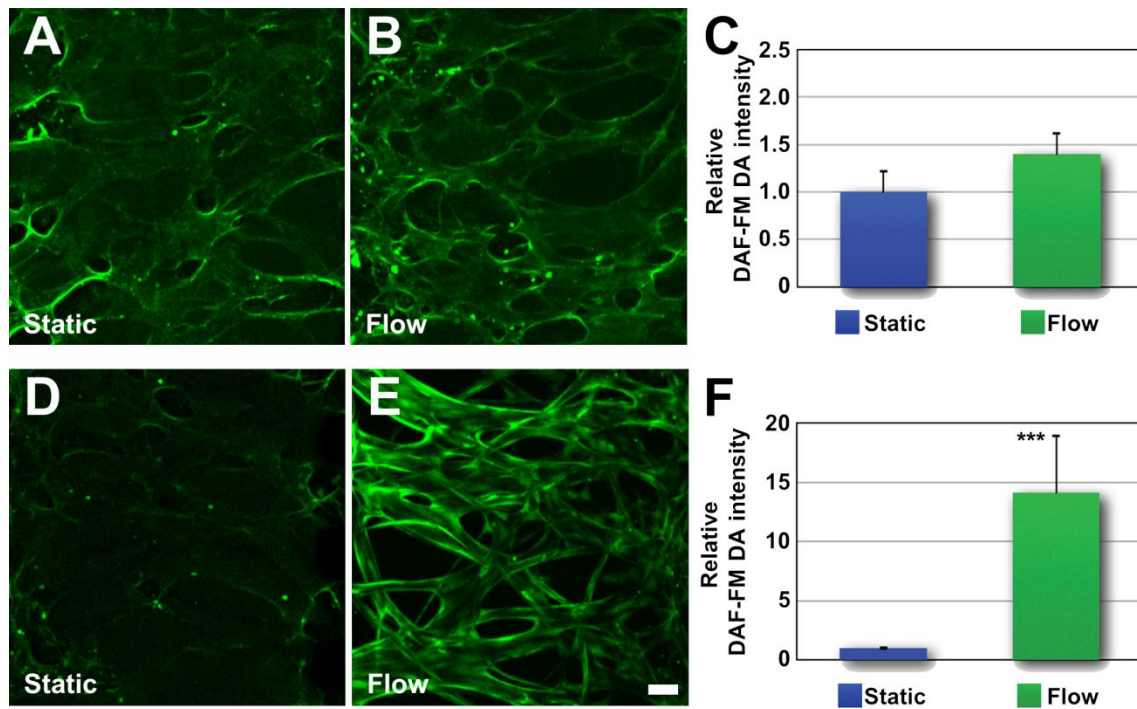


**Fig 2.12** Endothelial nitric oxide synthesis stimulated by presence of luminal flow. (A-C) Endothelial NO synthesis in the absence of L-arginine supplement in perfusate. Without L-arginine, NO synthesis quantitatively assessed by DAF-FM DA (green) fluorescence intensity showed only insignificant increase in response to luminal fluid flow ( $n=5$  for static,  $n=6$  for flow condition). (D-F) Significant increase in fluorescent intensity of DAF-FM DA after exposure to 1 h of luminal flow, with L-arginine supplement in perfusate. Quantitative analysis of the fluorescence intensity showing a 14-fold increase after flow exposure, compared to static conditions ( $n = 9$  for static,  $n = 7$  for flow condition,  $***p < 0.005$ ). For quantification of NO synthesis based on fluorescent intensity, images were obtained under identical conditions. Scale bar, 50  $\mu\text{m}$ . Error bars represent SEM.

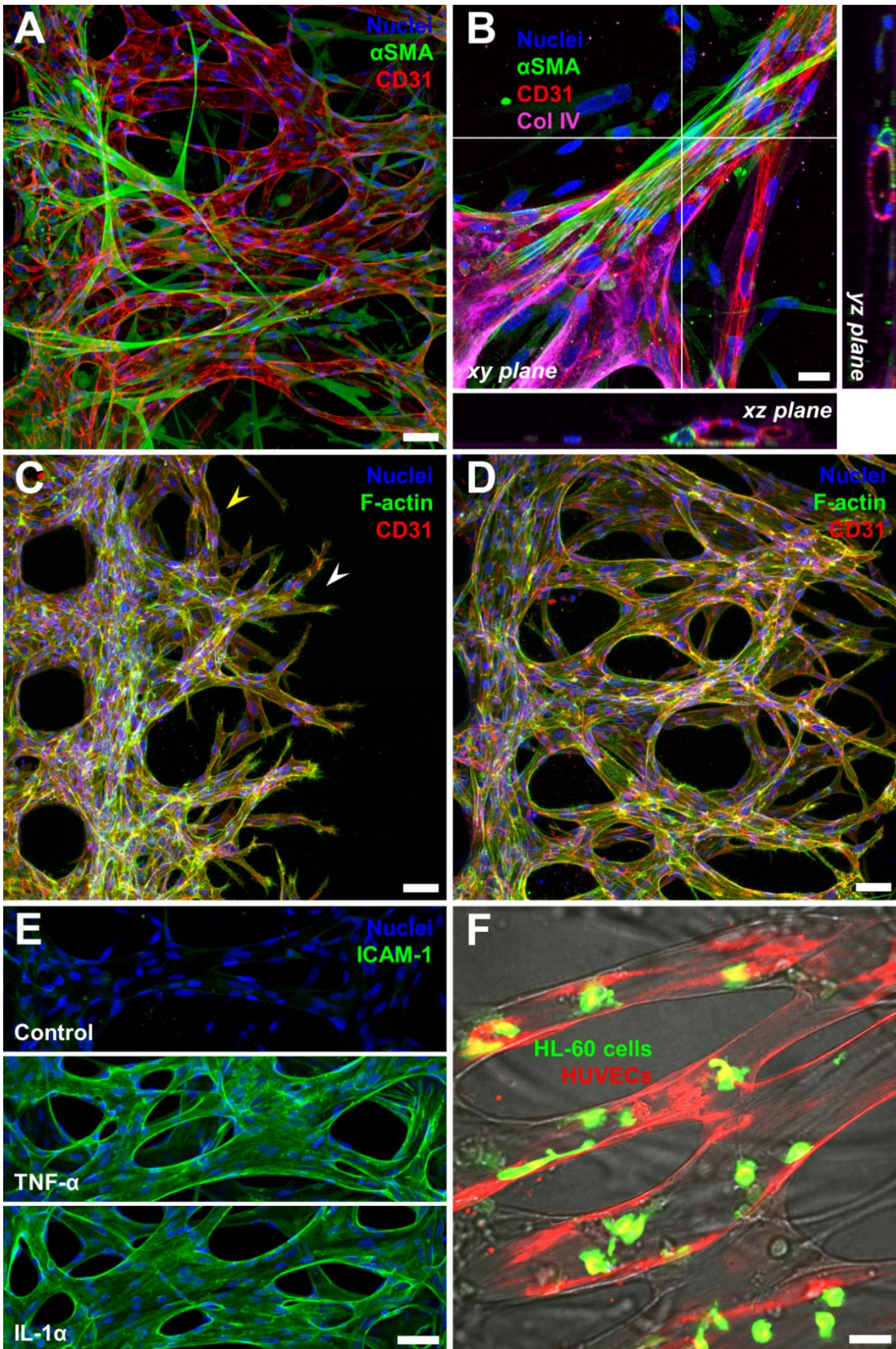


**Fig 2.13** Endothelial cell interactions with pericytes, cancer cells and leukocytes. (A) Microvascular network (CD31, red) covered with pericytes ( $\alpha$ -SMA, green). Scale bar, 50  $\mu$ m. (B) Higher magnification image and corresponding confocal sections of a pericyte-decorated blood vessel. Scale bar, 20  $\mu$ m. (C, D) Confocal micrographs of angiogenic sprouts grown for 2 and 4 days under co-culture with U87MG cancer cells. Scale bars, 20  $\mu$ m. (E) Expression of ICAM-1 (green) on the apical surface of blood vessels in response to inflammatory cytokines TNF- $\alpha$  (50 ng/mL) or IL-1 $\alpha$  (2 ng/mL). Scale bar, 50  $\mu$ m. (F) Adhesion of activated HL-60 neutrophils (green) on the inner surface of endothelium (red) promoted by endothelial stimulation with TNF- $\alpha$ . Scale bar, 20  $\mu$ m.

## **Chapter 3.**

# **Reconstituting lymphatic sprouting under combined biomolecular and mechanical stimuli**

### **3.1 Introduction**

Lymphatic vessels, together with blood vessels, form an intricate system of extensive, highly branched networks responsible for circulation and transport of fluid components within the body. Given the importance of the circulatory systems, functional abnormalities and aberrant growth of blood/lymphatic vessels are implicated in diverse diseases, including cancer, inflammation and parasite infection [3]. However, while intensive studies have been focused on the molecular mechanisms and the clinical implications of angiogenesis, lymphatic system has received considerably less attention from science and medicine until recent years, mainly due to the absence of specific markers discriminating lymphatic vessels in tissues. During the past decade, a series of seminal discoveries revealing specific markers of lymphatics [64, 65] and involvements of lymphangiogenesis in cancer metastasis [66, 67] prompted an upsurge of research interests and knowledge in this subject, whereas the large part of molecular mechanisms associated with lymphatic vessel growth still remain to be identified clearly.

Sophisticated models using experimental animals, such as implantation of VEGF-C or -A overexpressing tumor cells [66, 68] or growth factor-releasing pellets into transgenic mice or mouse corneal micropockets[69], and genetic modifications to

developing *Xenopus laevis* tadpole [69] have been used to discover mechanisms of lymphatic sprouting from pre-existing lymphatics and lymphatic vessel development. More recently, *ex vivo* model using fragment of lymphatic ring isolated from mouse thoracic duct was developed to observe outgrowth of lymphatic capillaries within 3D ECM [70]. *In vitro* models developed for angiogenesis studies including Matrigel tubulogenesis assay, endothelial cell-coated carrier bead- or embryoid body-based sprouting assay can be modified to be suitable for lymphangiogenesis studies by using endothelial cells from lymphatic origins [5, 71]. Of particular note, a series of studies performed by Melody Swartz and colleagues demonstrated unique *in vivo* and *in vitro* models identifying intriguing roles of interstitial flow in the process of lymphatic morphogenesis. In these studies, physiological level of interstitial flow, penetrating cell-laden 3D ECM [72] or regenerating skin of a mouse tail [73], was shown to promote tubular morphogenesis of lymphatic endothelial cells (LECs) in fibrin matrix, as well as provide directional guidance in regenerating lymphatic vessels, illustrating that involvement of interstitial flow could provide better simulation of lymphatic morphogenesis *in vitro*. However, currently available *in vitro* models still have limited abilities in reconstituting multistep cascades of sprouting morphogenesis of lymphatics, as these models partially integrate key environmental constituents essential for the corresponding phenomenon, and provide limited spatiotemporal control over cellular, biochemical and mechanical components at relevant length scales.

In this chapter, we describe a microfluidic-based experimental platform optimally designed to reconstitute sprouting morphogenesis of lymphatic vessels in 3D extracellular matrix (ECM). Our microfluidic platform is configured to be ideally suited

to integrate important constituents of cellular microenvironments surrounding lymphatic endothelial cells, which include 3D ECM, stromal fibroblasts, biochemical stimuli and interstitial fluid flow, all of which shown to synergize in morphogenesis of LECs. Especially, we focused on the role of fluid flow across 3D ECM, asking how presence, direction and magnitude of interstitial flow influence morphogenesis of LECs along with the soluble biochemical cues. Surprisingly, we found that lymphatic sprouting induced in response to pro-lymphangiogenic factors is greatly augmented when the lymphatic sprouts grow against the direction of interstitial flow with directional alignment along streamline of the flow, while the interstitial flow abrogated formation and growth of lymphatic sprouts along the flow direction. Further investigation with varying intensity of interstitial flow revealed that LECs not only exhibited distinct behaviors on the direction of flow, but also on the magnitudes with dramatic changes on the rates of protrusion formation, invasion into 3D ECM, and their morphological figures.

In a combined stimulation of pro-lymphangiogenic factors and interstitial flow, LECs exhibited robust and active cellular dynamics forming sprout-like multicellular structures morphologically characterized by numerous filopodial protrusions, hollow luminal structures, complex interconnections and branching patterns. These lymphatic sprouts uniformly expressed lymphatic-specific markers, including LYVE-1, Prox-1, VEGFR-3 and podoplanin, and displayed perforated basement membrane and continuous adherens junction protein characteristic of sprouting lymphatics. Based on robust, reproducible and physiologically relevant attributes of our platform, we also demonstrate the potential utility of our chip for testing pharmacological inhibitors of

lymphangiogenesis with quantitative evaluation of drug effects as well as high resolution observation of drug influences on phenotypes and processes of lymphatic sprouting.

## **3.2. Materials and methods**

### **3.2.1. Device Fabrication**

A master with positive relief structures of negative photoresist, SU-8 (MicroChem), on a 4-inch silicon wafer was made by photo-lithography. A 10:1 (w/w) mixture of polydimethylsiloxane (PDMS, Sylgard 184, Dow Corning) and curing agent was poured on the master and cured for 60 min on a hot plate at 90 °C. Polymerized PDMS was cut from the master, yielding negative replica-molded structures. Using 6 mm biopsy punch and sharpened blunt syringe needle, hydrogel injection ports and the reservoirs for the cell culture medium were punched out. After carefully removing dusts and PDMS cutting shreds using nitrogen gas air gun and residue-free tape, the device was assembled with the glass coverslip by treating oxygen plasma for 1 minute and then bringing them into contact, followed by the incubation in an 80 °C dry oven for 48 hours to restore hydrophobic characteristic of PDMS. Before the experiments, the devices were sterilized by UV irradiation.

### **3.2.2. Cell Culture and Seeding in Microfluidic Devices**

Human dermal lymphatic microvascular endothelial cells (HMVEC-dLyAd, Lonza) were cultured in endothelial basal medium-2 (EBM-2, Lonza) supplemented with EGM-2 MV BulletKit and passage 6~7 used for experiments. Normal human lung fibroblasts

(NHLF, Lonza) were cultured in fibroblast basal medium (FBM-2, Lonza) supplemented with FGM-2 BulletKit and used for experiments at passage 6~8. All cells were incubated at 37 °C in a humidified 5% CO<sub>2</sub> atmosphere.

The fibrinogen (Sigma) was dissolved in DPBS (Gibco) and filter-sterilized (0.22 μm pore), and then supplemented with aprotinin (0.15 U/mL, Sigma). After detached from the tissue culture plate, fibroblasts were centrifuged down and resuspended in the fibrinogen solution (2.5 mg/mL) at 10<sup>7</sup> cells/mL. The cell solution was mixed with thrombin (50 U/mL, 50:1 cell solution:thrombin ratio) and then immediately injected into fibroblast channels, followed by 5 minutes of polymerization at room temperature. The central channel was filled with acellular fibrin (2.5 mg/mL) and then left to clot for 5 min at room temperature. After fibrin gel polymerization, EGM-2 MV medium was introduced into the cell culture medium channels and loaded in the reservoirs. The devices were kept in the incubator to allow fibroblasts to be adapted within the fibrin gel. After 24 hours of incubation, ~ 5 μL of cell suspension with LECs concentrated at 10<sup>7</sup> cells/mL were introduced into one of the cell culture medium channels after aspirating culture medium from the reservoirs, and then the devices were tilted by 90 degrees and incubated for 30 min to allow gravity-assisted cell adhesion to the side wall of fibrin gel filling the central channel. Either plain EGM-2 MV or growth factor-cocktail-supplemented EGM-2 MV was immediately added to the reservoirs of the cell culture medium channels, establishing biomolecular environments as denoted in each experimental condition. Pro-lymphangiogenic cocktail including vascular endothelial growth factor-A (VEGF-A, R&D Systems), vascular endothelial growth factor-C (VEGF-C, R&D Systems), basic fibroblast growth factor (bFGF, Invitrogen) and

sphingosine-1-phosphate (S1P, Sigma) was used for the experiments with concentrations at 50 ng/mL for VEGF-A and bFGF, 100 ng/mL for VEGF-C, and 1  $\mu$ M for S1P except when otherwise denoted. In an alternate condition, pro-lymphangiogenic cocktail comprised of vascular endothelial growth factor-D (VEGF-D, R&D Systems), hepatocyte growth factor (HGF), insulin-like growth factor 1 (IGF-1) and platelet-derived growth factor BB (PDGF-BB) was used with concentration at 100 ng/mL for VEGF-D, HGF and IGF-1, and 50 ng/mL for PDGF-BB. In both cocktails, endocan (also called endothelial specific molecule-1(ESM-1), 100 ng/mL) was added to enhance proliferation and migration of LECs in response to the stimulation of pro-lymphangiogenic factors [74].

For the experiments where interstitial flow across the layer of LECs was applied, pressure gradient was induced by volume difference between two fluidic channel compartments. Then the devices were maintained in the incubator and the samples were fixed and stored after 2 days of culture for quantification and further analysis. In the conditions with interstitial flows, volume difference was adjusted twice a day as the pressure gradient may gradually dissipate over time. Unless otherwise noticed, speed of applied interstitial flow was  $\sim 1 \mu\text{m/s}$ , which corresponds to the measured value of interstitial flow of *in vivo* [75].

In an alternate experimental configuration, a microfluidic platform having two central channels was used to observed lymphatic sprout formation from the LECs comprising interconnected tubular networks formed via vasculogenesis-like endothelial assembly process, which allowed bi-directional interstitial flow either from RF to LF channel or LF to RF channel, contrast to the previous setting where LECs attached on the side wall

of fibrin matrix only allowed one-way direction of interstitial flow. In this modified microfluidic platform, lymphatic endothelial cells were introduced into one of central channels at a concentration of  $4 \times 10^6$  cells/mL, then filling acellular fibrin matrix at the juxtaposed channel. At both sides of fibroblast channels, fibroblasts were embedded within fibrin matrix at a concentration of  $10^7$  cells/mL. The cells introduced into the device were incubated overnight to allow cell attachment and spreading inside the fibrin matrix, and then interstitial flow of either direction was applied via hydrostatic pressure gradient.

### **3.2.3. Immunofluorescence Staining and Confocal Imaging**

For immunofluorescence staining, cells in the devices were washed once with PBS and fixed using paraformaldehyde (PFA, 4 % w/v in PBS) for 15 min, permeabilized with Triton X-100 (0.15 % v/v in PBS) for 15 min, and then blocked in 3 % (w/v in PBS) bovine serum albumin (BSA) for 1 hour at room temperature. Immunofluorescent staining was performed by incubating samples with primary antibodies overnight at 4 °C. For antibodies non-conjugated with fluorescent markers, samples were subsequently incubated with appropriated secondary antibodies at room temperature for 2 h. Antibodies used were rabbit polyclonal antibodies for human LYVE-1 (1:1000), Prox1 (1:1000) and VEGFR-3 (1:1000, all from Reliatech), rat monoclonal antibody for human podoplanin (1:200, clone NC-08, AlexaFluor488, BioLegend), and mouse monoclonal antibody specific for human CD31 (1:200, clone WM59, AlexaFluor647, BioLegend), and AlexaFluor647 goat anti-rabbit IgG (1:1000, Molecular Probes). For staining F-actin and DNA, samples were AlexaFluor488 or AlexaFluor594-conjugated phalloidin (2 units/mL, Molecular Probes) and Hoechst 33342 (10 µg/mL, Molecular

Probes) were added and incubated for 1 h and 30 min, respectively. After incubation with antibodies and cell staining reagents, the samples were washed three times with PBS and stored until confocal microscopic imaging.

#### **3.2.4. Quantitative validation of interstitial flow across 3D ECM**

Interstitial flow across the 3D ECM and the LECs was generated by applying hydrostatic pressure gradient with defined volume difference between the reservoirs connected to each fluidic channel, and verified by measurement of flow velocity using FRAP (fluorescent recovery after photobleaching) technique, as described previously [76].

#### **3.2.5. Treatment of anti-lymphangiogenic factors**

In experiments testing and quantifying lymphangiogenic sprouting in the presence of anti-lymphangiogenic factors, pro-lymphangiogenic factors including VEGF-C (100 ng/mL), VEGF-A (50 ng/mL), bFGF (50 ng/mL) and S1P (1  $\mu$ M) were added to the opposite channel of LEC-seeded cell culture medium channel, and interstitial flow directed from RF to LF channel was applied. Small molecule inhibitors including Axitinib, Cabozantinib, PD173074, SAR131675 (all from Selleckchem), FTY720 (S)-P (Caymanchem), Sunitinib malate (R&D Systems) were dissolved according to the manufacturers' instruction and administered to both RF and LF channels. For each inhibitor, three doses were tested at concentrations of 0.01, 0.1 and 1  $\mu$ M for Axitinib and FTY720 (S)-P, and 0.1, 1 and 10  $\mu$ M for Cabozantinib, Sunitinib malate, PD173074 and SAR131675 along with the corresponding vehicle-treated controls. B-A interstitial flow induced by hydrostatic pressure difference were reset twice a day and the lymphangiogenic sprouts after 2 days of growth were fixed with 4 % PFA and stored for

further analysis. To obtain dose-dependent responses, experiments were performed at least three times per each condition.

### **3.2.6. Quantification and statistical analysis.**

To quantify area of invasion, each confocal images of f-actin-stained sprouts were processed to obtain Z-projections of the 3D stacks using IMARIS (Bitplane), and the background fluorescent of each image was eliminated with Image J (NIH). Statistical analysis was obtained from Student's *t*-test analysis.

## **3.3. Results**

### **3.3.1. Microfluidic platform for lymphatic sprouting under stimulation of pro-lymphangiogenic factors and interstitial flow**

To investigate lymphangiogenic sprouting *in vitro*, we adapted a microfluidic platform which offers physiologically relevant sprouting morphogenesis of endothelial cells, as previously described [62]. The device is consists of three independent hydrogel channels (FIG 3.1A), which are in parallel and interconnected via two fluidic channels, each termed RF (right-side fluidic) channel and LF (left-side fluidic) channel, respectively. The central channel, which is filled with fibrin matrix, serves as a scaffold for formation and growth of lymphangiogenic sprouts by human microvascular lymphatic endothelial cells (referred as LECs hereafter). An interface formed between LF channel and the central ECM channel is uniformly coated with LECs, and then subsequently applied with gradients of pro-lymphangiogenic factors and/or interstitial flow driven by hydrostatic pressure gradient. Human stromal fibroblasts were cultured

in outermost hydrogel channels embedded within fibrin matrix to support sprouting morphogenesis of LECs, via contact-independent and paracrine cell-cell interactions.

In order to model pathological cellular microenvironments of LECs where tissue-derived pro-lymphangiogenic factors and lymphatic drainage-induced interstitial flow simultaneously present, we configured our chip to enable combinatorial stimulation of LECs with soluble pro-lymphangiogenic factors and interstitial flow (FIG 3.1B, C). To clearly distinguish each experimental condition, the conventions conditions of pro-lymphangiogenic factor gradients and interstitial flow were used as shown in Table 3.1.

### **3.3.2. Sprouting of lymphatic endothelial cells in response to gradients of pro-lymphangiogenic factor**

Using the microfluidic chip, we first examined the effects of spatial gradients of pro-lymphangiogenic factors in sprouting morphogenesis of LECs, with no interstitial flow applied. Pro-lymphangiogenic factors that include vascular endothelial growth factor-C (VEGF-C), vascular endothelial growth factor-A (VEGF-A), basic fibroblast growth factor (bFGF) and sphingosine 1-phosphate (S1P) were chosen from factors shown to directly induce proliferation, migration and differentiation of LECs *in vitro* [77-79], and reported to be associated with lymphatic vessel development and sprouting morphogenesis *in vivo* [66, 80-82]. Besides this defined soluble factors, stromal fibroblasts were introduced in the cell culture system to support pro-lymphangiogenic factor-induced sprout growth.

When each individual factor was added to the RF channel, increasing gradient of pro-lymphangiogenic factor induced directed invasion of LECs into the 3D ECM (Fig 3.2G), while rarely exhibiting multicellular structures with hollow lumen. Addition of the

cocktail containing these pro-lymphangiogenic factors promoted collective cell migration into the matrix in greater extent compared to the single factor-added conditions, with some of sprouts exhibited lumenized structures as early as 2 days of growth, suggesting cooperative contributions of these factors in forming multicellular sprouts. Addition of higher concentration of pro-lymphangiogenic factors induced much significant number and length extension of lymphatic sprouts (Fig 3.2H). In contrast, negative gradient of the cocktail failed to induce lymphatic sprouts, as LECs preferentially remained in the LF channel without apparent invasion into the 3D ECM (Fig 3.3A). Interestingly, LECs formed multicellular sprouts even when both LF and RF channel were added with identical concentration of the cocktail Fig 3.2H).

### **3.3.3. Presence, direction and magnitude of interstitial flow determine activity of pro-lymphangiogenic factor-induced lymphatic sprouting.**

To investigate the influence of interstitial flow across the 3D ECM and layer of LECs, we next tested whether the presence of interstitial flow affect pro-lymphangiogenic factor-induced sprouting of LECs in our chip. The cocktail of pro-lymphangiogenic factors (VEGF-A and C, bFGF and S1P) were identically added to both RF and LF channel to minimize the influence that may present due to differences of biochemical milieu of LECs between the conditions, while applying higher hydrostatic pressure either to the RF or the LF channel to induce pressure gradient across the matrix and the LECs.

Surprisingly, presence of interstitial flow (1  $\mu\text{m/s}$ ) with direction simulating lymphatic drainage (from the RF channel to the LF channel) significantly increase sprouting activity of LECs in response to pro-lymphangiogenic factors compared to the

static condition, with increased density of sprouts and length extensions (Fig 3.2B, C, E and F). To further test whether this observation is restricted to these factors, we examined a distinct cocktail of factors comprised of vascular endothelial growth factor-D (VEGF-D), hepatocyte growth factor (HGF), insulin-like growth factor 1 (IGF1) and platelet-derived growth factor BB (PDGF-BB), all of which were reported to prompt proliferation and differentiation of LECs *in vitro* [77, 83-85]. Similarly, LECs tested with combined stimulation of the cocktail and interstitial flow exhibited marked increase in sprouting activity compared to the static condition (Fig 3.4). Interstitial flow-enhanced sprouting activity was also observed in the conditions where LECs were stimulated with each individual factor comprising the cocktail (Fig 3.2G), suggesting that the influence of interstitial flow was not dependent on the specific ligand-mediated activation of corresponding downstream signals. On the contrary, G=F- condition, negative pressure gradient for lymphatic drainage, almost completely abrogated the sprouting activity of LECs, with rare protrusions and cellular invasions into the matrix (Fig 3.3B). Active sprouting activity observed in interstitial flow conditions were not induced by the presence of interstitial flow itself, as the flow condition tested with no pro-lymphangiogenic factors (G0F+) resulted in inactive sprouting (Fig 3.2D). These results suggest that interstitial flow dictates pro-lymphangiogenic factor-induced lymphatic sprouting either by augmenting or suppressing the activity in a context dependent manner. Furthermore, although the presence of fibroblasts alone did not promote lymphatic sprouting, absence of fibroblasts in the culture system also exhibited relatively inactive and less organized lymphatic vessels (Fig 3.5), suggesting facilitative role of fibroblast-secreted factors in our fibrin-based 3D culture model.

Biophysical stimuli, such as flow-induced shear stress or mechanical strain elicit rapid activation of cellular signal transduction pathways, including Rho family of GTPases, phosphorylation of tyrosine kinase receptors and upregulation of cell-surface receptors [86-89]. To examine whether the magnitude of interstitial flow influences lymphatic sprouting, we observed the early processes of sprouting in chosen time domains, 6 hours and 12 hours of stimulation, where mechanical stimuli-mediated signaling pathways are strongly activated. Under the presence of pro-lymphangiogenic cocktail and interstitial flow ranging from 0.5  $\mu\text{m/s}$  to 4  $\mu\text{m/s}$ , the rate of protrusion and cellular invasion into the matrix were progressively promoted as the magnitude of interstitial flow increased, accompanying morphological transition on the cellular protrusions, from sharp spindle shapes to filopodia-rich pro-migratory phenotypes (Fig 3.6A). Interestingly, length of cellular protrusion was maximal at the 2  $\mu\text{m/s}$  condition among the magnitude tested (Fig 3.6B), while higher magnitude exhibited slightly less extended protrusions but significantly larger number of invasive cells (Fig 3.6C). These results illustrates pro-lymphangiogenic factor-induced lymphatic sprouting is not only influenced by the presence and the direction of interstitial flow, but also by its magnitudes, suggesting the role of interstitial flow as important morphoregulator of sprouting morphogenesis of LECs *in vitro*.

#### **3.3.4. Interstitial flow regulates lymphatic capillary network formation and directional expansion of network into avascular 3D ECM**

To further investigate the regulatory roles of interstitial flow during lymphatic morphogenesis *in vitro*, we adapted our microfluidic platform and modified the experimental procedure to enable us to observe capillary network formation of LECs,

which is in a fashion reminiscent of vasculogenesis of blood endothelial cells. Furthermore, modified design of the platform also allows us to investigate influence of interstitial flow on the directional guidance for the expansion of lymphatic capillary network into adjacent avascular ECM space (Fig 3.7F).

Under stimulation of pro-lymphangiogenic factors, LECs embedded in fibrin matrix developed into vacuolized, protrusion-extending morphology, subsequently assembled to form interconnected networks of lymphatic capillaries during 3 days of culture. In the presence of interstitial flow, progression of network development was significantly promoted (Fig 3.7D), resulting in well-lumenized and interconnected structures at day 3, compared to the capillary networks formed under static condition with relatively less interconnections and coverage area. Formation of lymphatic capillary networks by LECs did not show discernable differences in the structural feature as well as quantified coverage area depending on the direction of interstitial flow. However, expansion of the pre-formed lymphatic capillary network into the adjacent ECM channel was largely dictated by the direction of interstitial flow (Fig 3.7E). We found that migration of LECs into the acellular channel was significantly facilitated when LECs were stimulated with interstitial flow with opposite direction of lymphatic capillary growth. In this condition, LECs actively organized into multicellular structures with hollow lumens and filopodia extensions, showing marked differences in both morphological characteristics and extents of growth compared to the sprouts observed in the static condition (Fig 3.7B). In contrast, migration of LECs was significantly reduced in the presence of interstitial flow directed toward the avascular channel (Fig 3.7C), which showed even less migration compared to the static condition. These results clearly show that interstitial flow readily

provides morphoregulatory stimulus as well as directional guidance to expansion of lymphatic capillary networks according to its flowing direction.

### **3.3.5. Interstitial flow drives directional sprouting growth and filopodia formation**

We further analyze the influence of interstitial flow on morphological characteristics of lymphatic sprouts, specifically their directional orientation and filopodia extension. Of noted, lymphatic sprouts observed in the static and the interstitial flow condition displayed marked differences in their morphological characteristics (Fig 3.8A,B). Where LECs were subjected to the interstitial flow, the sprouts were abundant with filopodial protrusions and tip cell projections (Fig 3.8B), while the sprouts grown under static condition displayed relatively smooth outlines devoid of filopodia projections (Fig 3.8A). Cellular protrusions extended into the matrix under interstitial flow condition displayed increased incidence of branched structures and F-actin-rich filopodia. Formation and extension of filopodia was not restricted to the cells at the growing fronts, but continuously observed along the entire length of sprouts as shown in Fig 3.8C. Furthermore, the lymphatic sprouts in the interstitial flow condition were characterized by continuous and well-developed lumens, which was in apparent discrimination against the sprouts in static condition with less developed lumens and sparse interconnections between them.

We then compared the angle of orientation of lymphatic sprouts grown at three different conditions to compare the influence of biomolecular gradient and interstitial flow in directional alignment during growth of lymphatic sprouts. In the comparison of static conditions,  $G+F0$  and  $G=F0$ , the lymphatic sprouts showed slightly narrower

distributions in the presence of increasing concentration gradient of the cocktail (Fig 3.8D, E). Notably, LECs subjected to interstitial flow (G=F+) exhibited even further efficient directional growth toward the higher hydrostatic pressure, exhibiting clear alignment along the streamline of interstitial flow with large fraction of the sprouts distributed between -5 to +5 degree angles relative to the flow direction (Fig 3.8F). Taken together, these results illustrate that interstitial flow, with the direction reminiscence of lymphatic drainage, plays instructive role for sprouting morphogenesis of LECs by directionally guiding their growth, augmenting filopodia extension and lumenization.

### **3.3.6. Lymphatic sprouts exhibit structural and biochemical characteristics of *in vivo* lymphatics**

Integration of key features of lymphangiogenesis-inductive cellular microenvironments, this experimental model reconstitutes complex cellular dynamics that lead to formation of multicellular structures in 3D ECM. Figure 3.9A presents the confocal sections of lymphatic sprouts at day 2 formed under combined stimulation of pro-lymphangiogenic factors and interstitial flow, showing 3D structures with well-developed hollow lumens enclosed by lymphatic endothelial cells. To further examine structural and biochemical characteristics of lymphatic sprouts formed in our model, we performed microscopic observation of lymphatics immunostained against lymphatic specific markers (LYVE-1, Prox-1 and VEGFR-3), basement membrane (collagen IV and laminin) and intercellular adherens junction protein (VE-cadherin).

When examined with specific markers of lymphatic endothelial lineage, which include LYVE-1, Prox-1, podoplanin (D2-40) and VEGFR-3, all lymphatic sprouts in

the platform uniformly expressed these lymphatic specific markers, obtaining a clear, positive identification of lymphatic vessels (Fig 3.9B-D). Recent studies indicate that perilymphatic basement membrane of lymphatic capillaries exhibit discontinuous and perforated in contrast to continuous basement membrane of blood vessels. In agreement with the characteristic of *in vivo* lymphatics, lymphatic sprouts in our model also displayed discontinuous basement membrane revealed by collagen IV (Fig 3.10A) and laminin immunostaining (Fig 3.10B). These were also in sharp contrast to our previous observation of perfused human blood vascular networks formed in a 3D co-culture model of endothelial cells and stromal fibroblasts, which exhibited continuous and intact basement membrane [62]. Initial lymphatics present functionally specialized intercellular junctions, which is discontinuous button-like junctions, while collecting lymphatics and newly formed immature lymphatic sprouts are joined by continuous zipper-like junctions [90]. Observation of VE-cadherin pattern of the lymphatic vessels in our platform revealed the presence of continuous zipper-like junctions in resemblance with sprouting lymphatics *in vivo* (Fig 3.10C).

### **3.3.7. Inhibition of lymphangiogenesis by small molecular inhibitors and inflammatory cytokine**

By incorporating key elements of the tumor microenvironments harboring diverse cell types that secrete pro-lymphangiogenic factors and increased lymphatic drainage into our chip, we demonstrated that combined stimulation of biomolecules and interstitial flow leads to sprouting morphogenesis of human LECs in close resemblance with *in vivo* lymphatics in morphological and biochemical characteristics. The phenotypic similarities found in our chip lead us to use it as a test platform to evaluate the effects of

inhibitors of lymphangiogenesis. To address this aim, we performed the experiments using the cocktail of pro-lymphangiogenic factors, which includes VEGF-C, VEGF-A, bFGF and S1P, in the presence of interstitial flow and small molecule inhibitors that target receptors of the factors comprising the cocktail. Selected small molecule inhibitors include a VEGFR-3 inhibitor SAR131675, a multi-target inhibitor of VEGFR-2 and VEGFR-3; Axitinib and Sunitinib malate, a VEGFR-2 inhibitor XL184, a FGFR1 inhibitor PD173074 (FGFR1) and S1P1 selective antagonist W146. Considering the IC50 value reported for these inhibitors (Table 3.2), we tested 3 doses for each inhibitor, added to both fluidic channels from the initiation of sprouting experiments.

Notably, lymphatic sprouts grown in the presence of small molecule inhibitor exhibited dose-dependent growth inhibition (Fig 3.11A). In particular, multi-target inhibitors of VEGF receptors, Axitinib and Sunitinib malate, exhibited strong inhibition of lymphatic sprouting from the lowest dose treatments (Fig 3.11D, E), confirming the indispensable roles of VEGFRs, which were intensively studied for their primary importances in angiogenesis, also in lymphangiogenesis. One common feature of lymphatic sprouts treated with highest dose of inhibitor was loss of the filopodial protrusions, which was the characteristic feature of sprout morphology observed with combined stimulation of pro-lymphangiogenic factors and interstitial flow. These results demonstrated that our model is well-suited as a testing platform for potential inhibitors on sprouting morphogenesis of lymphatics. Interestingly, the samples treated with FTY720 (S)-P exhibited non-impaired, rather significantly promoted growth of lymphatic vessels regardless of the doses tested, while showing gradual inhibition of

filopodial extensions as the dose increased.

### **3.4. Discussion**

Mechanical stress induced from blow flow has been shown to be an important mediator of vascular system, regulating early embryonic vascular patterning[47, 89], functional homeostasis of quiescent blood vessels [91] as well as dynamic vessel remodeling in physiological and pathological processes. Owing to its importance in vascular physiology, molecular mechanisms by which endothelial cells sense the fluid flow and subsequently transduce the signals are extensively studied, reporting participation of numerous flow sensing machineries including integrins [92, 93], ion channels [94], glycocalyx [95], G protein-coupled receptors [96], interendothelial adherens junctions and VEGF receptor [19]. However, compared to blood endothelial cells, history of researches on lymphatic endothelial cells is relatively short, leaving large parts of mechanisms, including the role of mechanical stimuli, to be elucidated. Furthermore, *in vitro* examination of lymphatic endothelial morphogenesis still relies on macro-scale cell-culture models which are not able to precisely control the cellular microenvironments in a high spatiotemporal resolution. While it has been suggested that lymphatic drainage and interstitial flow may provide morphoregulatory roles in lymphatic morphogenesis [97], the role of these mechanical stimuli on the behaviors of LECs during initiation and progression of sprouting lymphangiogenesis remain elusive mainly due to a lack of practical experimental platforms. Considering a growing list of disorders that can be treated by targeting aberrant lymphatic growth and functions, there remains urgent demand for appropriate *in vitro* platform that satisfies the criteria of

physiological relevancy, control over the relevant parameters such as cellular, biochemical and mechanical properties while not compromising simplicity and reproducibility of experiments. The use of microfluidic-based platform has brought improved *in vitro* models of angiogenesis [98, 99], function of endothelium [100] as well as transendothelial migration of tumor cells [30], there is no single platform optimized for the investigation of lymphangiogenesis with precise control over parameters involved.

Using microscale engineering approaches, we designed a microfluidic assay which allows 3-dimensional culture of human microvascular LECs under paracrine interactions with stromal fibroblasts and co-stimulation with biochemical cues and interstitial flow, all of which shown to have synergistic roles in sprouting morphogenesis of LECs. By integrating these lymphatic-relevant microenvironmental cues, we found that interstitial flow either augments or abrogates initiation and directional growth of lymphatic sprouts in a context-dependent manner, and demonstrated that the lymphatic sprouts formed under combined stimulation exhibited close mimicry of structural, biochemical and morphological characteristics of *in vivo* lymphatic capillaries.

High interstitial pressure and subsequent elevation of interstitial flow velocity correspond to one of the hallmarks of tumor microenvironments [101]. In line with this, tumor-secreted growth factors such as VEGF promote leaky blood vessels, and enlargement of collecting lymphatic vessels, leading to increased interstitial flow across the tissue space and fluid drainage into the initial lymphatics. It has been suggested that changes of fluidic environments observed within tumor microenvironments may

promote dissemination of tumor cells through autologous chemotaxis mechanism [102, 103] and morphogenesis of endothelial cells using sophisticated microfluidic models [29]. The influences of interstitial flow observed in these systems are two-fold. First, interstitial flow bias the distribution of cytokines secreted from cells or liberated by matrix metalloproteinases. Second, mechanical stresses induced by interstitial flow directly activate mechanosensors on the cell surface, triggering downstream signaling pathways, while exact mechanisms associated with cellular mechanotransduction still require extensive investigations. Recent studies using *in vivo* models also revealed an imperative role of interstitial pressure-driven tension during lymphatic vessel development in mouse embryo through activation of integrins [104], as well as interstitial flow across the tissues during lymphatic regeneration in wound site through MMP-mediated fluid channeling [105]. The study of Polachech *et al.* demonstrated that the influences of interstitial flow on the directional migration of tumor cells may provide competing signals, such as autologous gradient generation causing downstream migration and tensions exerted to integrins inducing upstream migration [106]. In our study, the distribution of soluble pro-lymphangiogenic factors, which is exogenously added to the culture system, is largely dictated by the presence of interstitial flow, while forming almost uniform concentration of these factors across the fibrin matrix. In this condition, the influences of interstitial flow on the lymphatic sprouting observed in our results may be induced by the activation of mechanosensing machineries on the LECs, rather than extracellular biochemical gradients created by interstitial flow. In tumor microenvironments and developing embryos, lymphatic sprouting should be directed toward the upstream of interstitial flow or location of higher fluidic pressures, which

correspond to the directional growth of lymphatic sprouting observed in our chip.

While we demonstrated that interstitial flow can greatly augment initiation and growth of lymphatic sprouting *in vitro*, interstitial flow per se do not exert pro-lymphangiogenic stimuli to the LECs in our model. Rather than working as a stimulant of lymphatic morphogenesis, a study of Miteva *et al.* suggest that transmural flow corresponding to the level of physiological state promoted fluid transport function and characteristic intercellular junction expression of lymphatic endothelium [107], meanwhile Lin *et al* reported that VEGF-C/VEGFR-3 signaling is not prerequisite for the maintenance of the lymphatic vasculature [108]. Along with our experimental data presented in this chapter, it can be suggested that interstitial flow works as a strong inducer of lymphatic sprouting only in the presence of pro-lymphangiogenic factors, while it promotes physiological lymphatic functions in a normal health state.

Filopodia projections expressed by tip cells at the distal edge of angiogenic sprouts cells are important machinery responsible for sensing surrounding environments, such as VEGF-A concentration gradient [41]. In general, expression of filopodia extensions exhibits spatially restricted to tip cells in angiogenic sprouts through Notch-dependent suppression of filopodia extensions at the stalk cells [109, 110], allowing sustained, directional elongation toward a source of angiogenic factors. One of interesting observations made in this study is that lymphatic sprouts, under combined stimulation of pro-lymphangiogenic factors and interstitial flow, exhibit spatially non-restricted filopodia projections along the entire length of sprouts as observed *in vivo*. However, LECs treated with pharmacological compound FTY720 (S)-P revealed almost complete loss of filopodia protrusions, while the directional guidance and growth sprouts were

non-impaired and even promoted. While large body of information regarding mechanisms by which LECs probe local microenvironment during sprouting lymphangiogenesis is still elusive, absence of strict tip-stalk specifications and filopodia-independent growth of lymphatic sprouts observed in our chip may raise the hypothesis that there might be still unknown, but distinct mechanism of guiding lymphatic endothelial cells. Moreover, our observation that the lymphatic sprouts displayed directional alignment along the streamline of interstitial flow suggests that interstitial flow play instructive roles during lymphatic sprout growth.

Notation	Definition	Symbols
G	Concentration gradient of pro-lymphangiogenic cocktail	0 indicates no pro-lymphangiogenic factors added to the both fluidic channel, + and – indicates factors added either to RF or LF channel, = indicates cocktail added to both fluidic channels.
F	Interstitial flow	0 indicates static condition, + and - indicates higher liquid volume applied either at the RF channel or LF channel.

**Table 3.1** Notation for gradient of pro-lymphangiogenic factors and interstitial flow

	Molecular weight	Target	IC50
SAR131675	358.39	VEGFR-3	20 nM
XL184	501.51	VEGFR-2	0.035 nM
PD173074	523.67	FGFR1	25 nM
		VEGFR-2	100~200 nM
Axitinib	386.47	VEGFR-2	0.2 nM
		VEGFR-3	0.1~0.3 nM
Sunitinib malate	532.56	VEGFR-2	80 nM
		VEGFR-3	48 nM
W146	342.37	S1P1	
FTY720 (S)-P	387.5	S1P1	2.1 nM
		S1P3	5.9 nM
		S1P4	23 nM
		S1P5	2.2 nM

**Table 3.2** Small molecule inhibitors tested for anti-lymphangiogenic activity

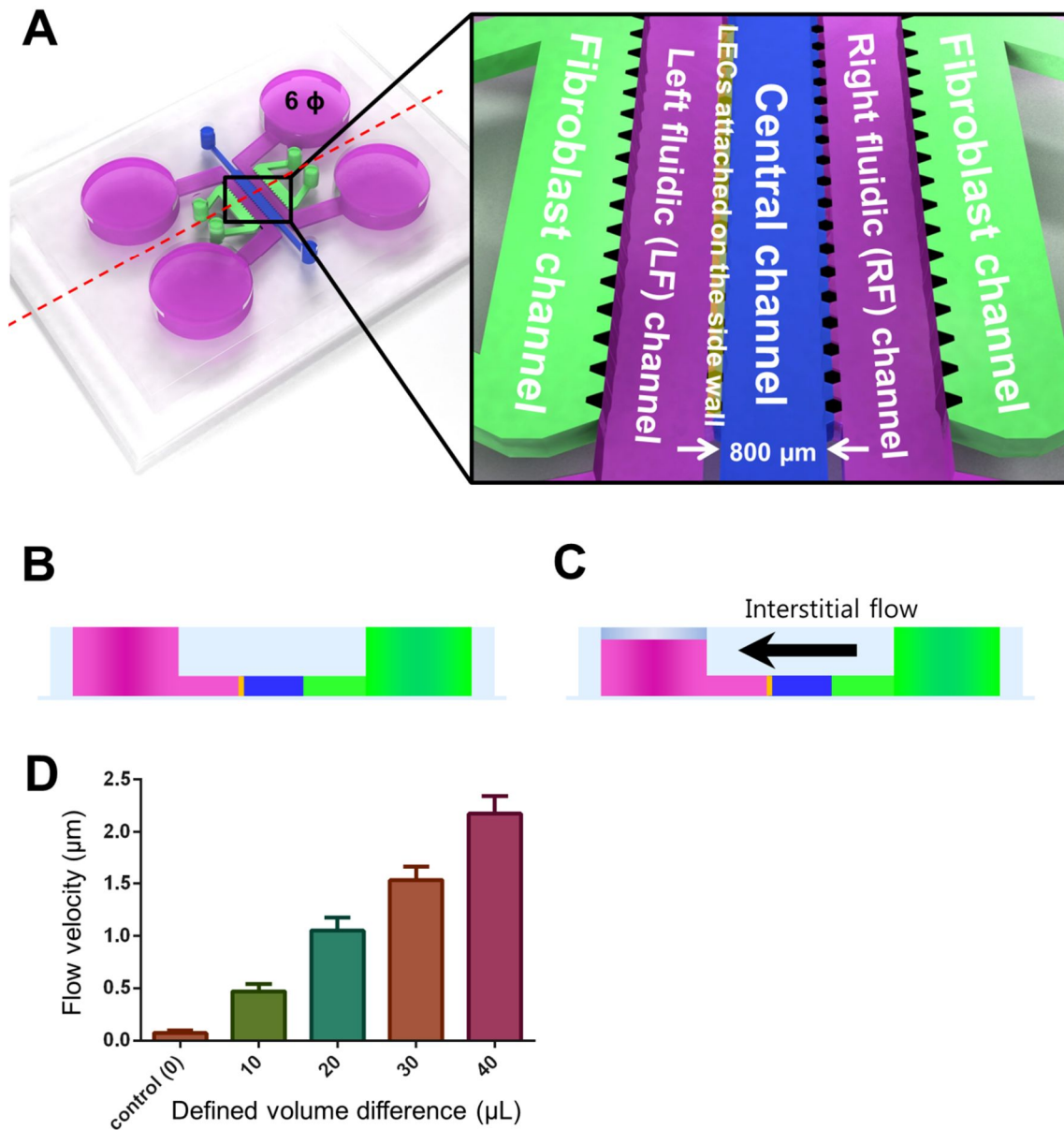


**Fig 3.1** Microfluidic chip for investigation of lymphatic sprouting under combined stimulation biochemical stimulants and interstitial flow. (A) A schematic diagram of microfluidic chip comprised of three independent hydrogel channels and two fluidic channels. (B, C) Schematics of experimental configuration for pro-lymphangiogenic factor gradient formation and application of interstitial flow. Addition of pro-lymphangiogenic factors either to LF or RF channel (RF channel in the figure) develops

diffusion based concentration gradient over time. Applying defined volume difference to the reservoirs connected to RF and LF channel resulted in pressure gradient that drives interstitial flow. (D) Quantitative validation of interstitial flow with direction from RF to LF channel with varying hydrostatic differential applied via define volume differences, showing interstitial flow level proportional to the applied volume differences.

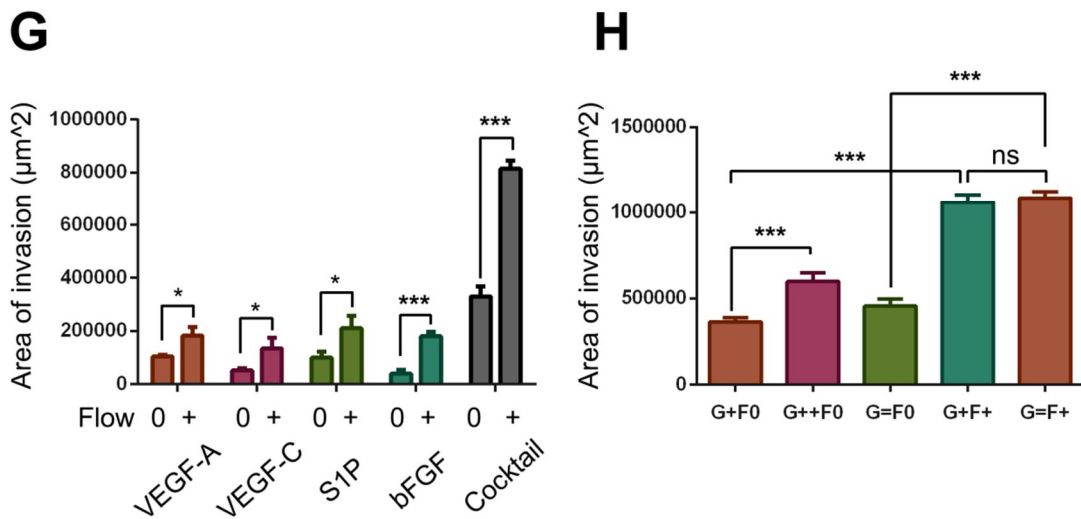
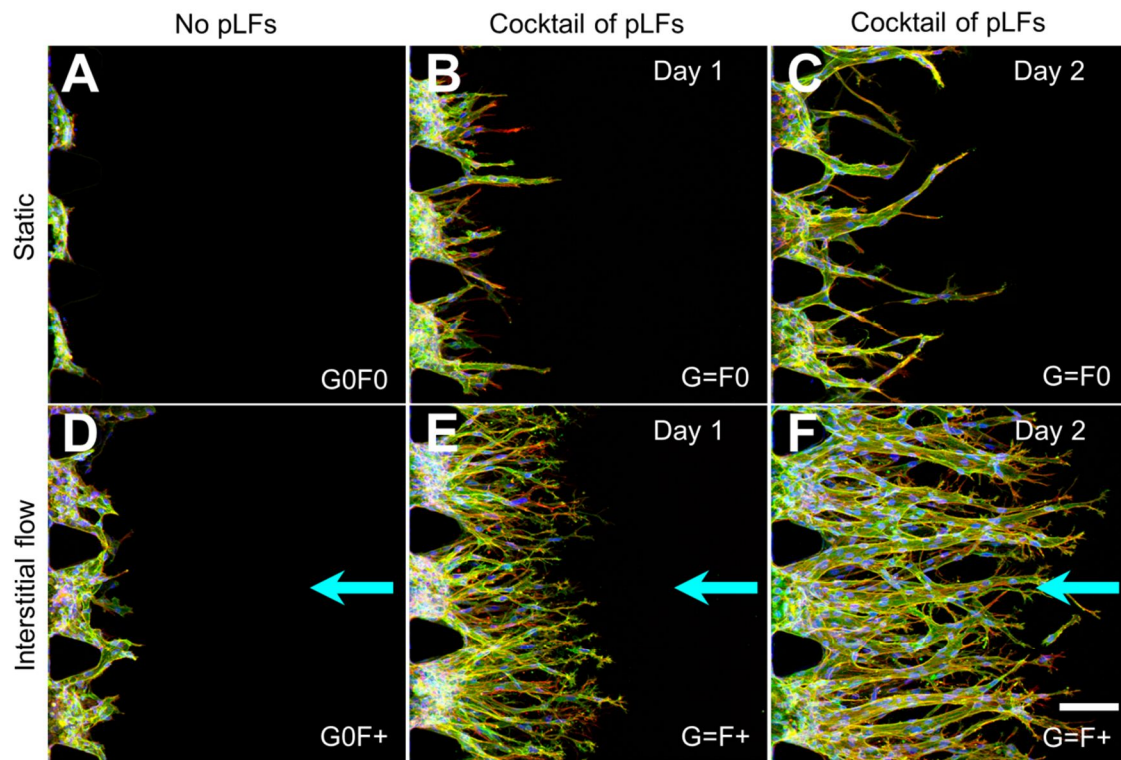


**Fig 3.2** Pro-lymphangiogenic factors and interstitial flow synergistically induced lymphatic sprout formation and growth. (A) With no pro-lymphangiogenic factors, LECs showed no invasion into the fibrin matrix. (B, C) LECs stimulated with cocktail of pro-lymphangiogenic factors (VEGF-A, VEGF-C, bFGF and S1P) invaded into the fibrin matrix to form sprout-like multicellular structures during 2 days of culture. (D) Application of interstitial flow with no pro-lymphangiogenic factors, invasion of LECs

were rarely observed. (E, F) In the presence of the cocktail and interstitial flow, LECs exhibited greater sprout formation and growth against the direction of flow, showing multicellular collective migration forming well-defined lumens. Scale bar, 100  $\mu\text{m}$ . (G, H) Quantification of LEC invasion into fibrin matrix. \* $P < 0.05$ , \*\*\* $P < 0.0005$ .  $n = 4$  chips per each condition for Fig 3.2G, and at least 10 chips for Fig 3.2H.

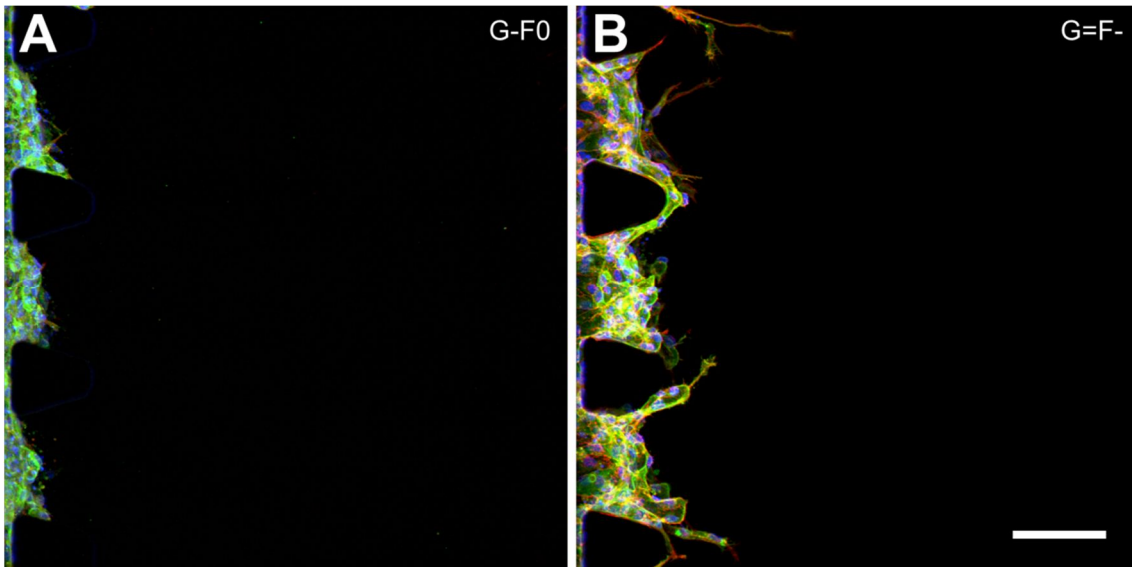


**Fig 3.3** LECs tested with negative concentration gradient (A), and higher hydrostatic pressure at the LF channel (B) resulted in inactive lymphatic sprout formation and growth. Scale bar, 100  $\mu\text{m}$ .

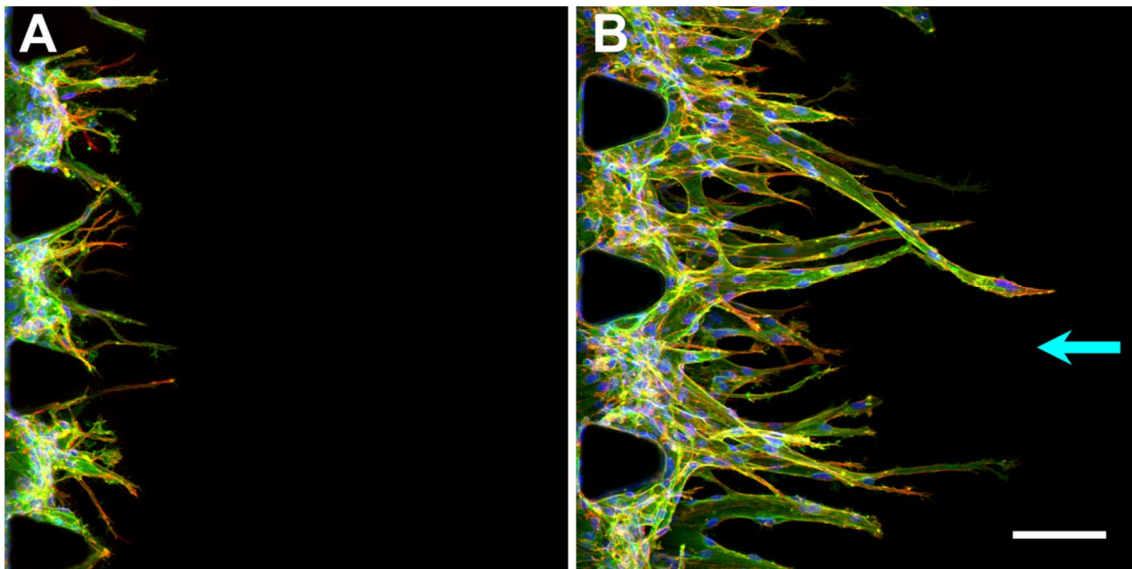
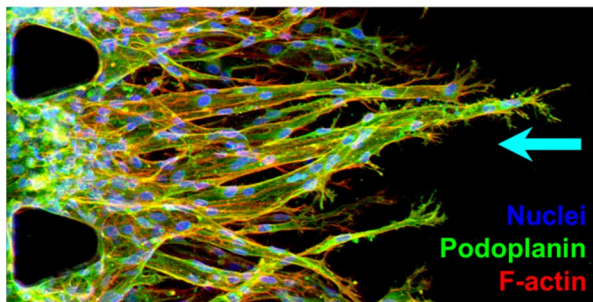
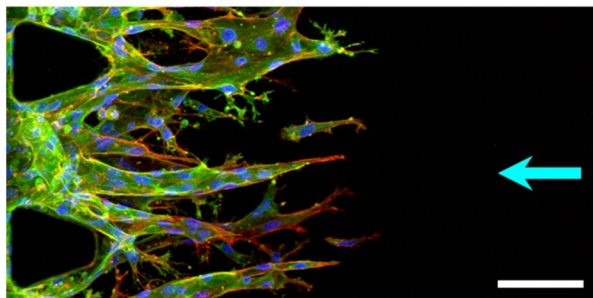


**Fig 3.4** LECs stimulated with cocktail of pro-lymphangiogenic factors comprised of VEGF-D, HGF, IGF-1 and PDGF-BB either in static (A) or interstitial flow condition (B), also revealing flow-enhanced sprouting activity. Scale bar, 100  $\mu\text{m}$ .

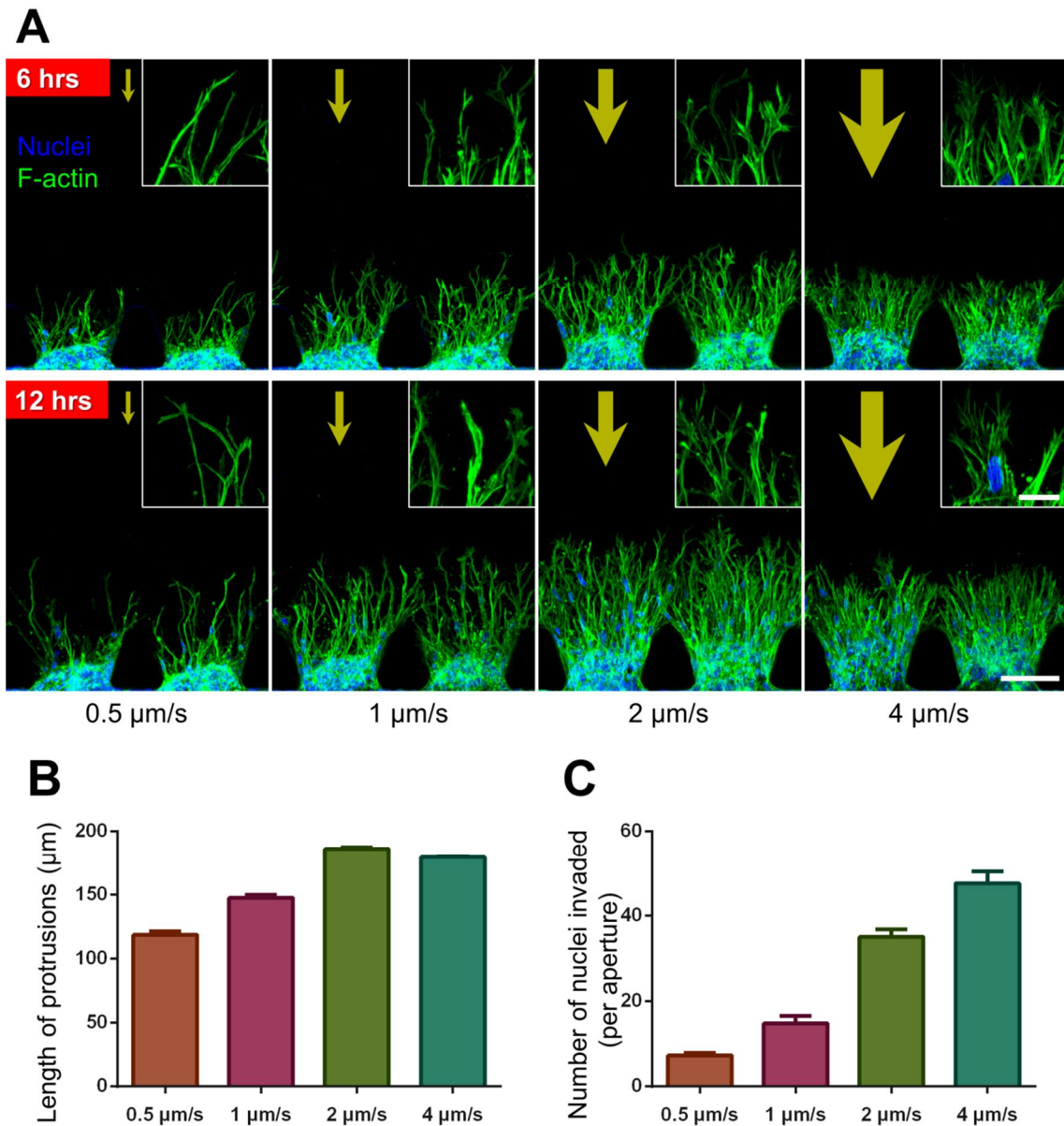
Day 2, Co-culture w/ stromal fibroblasts



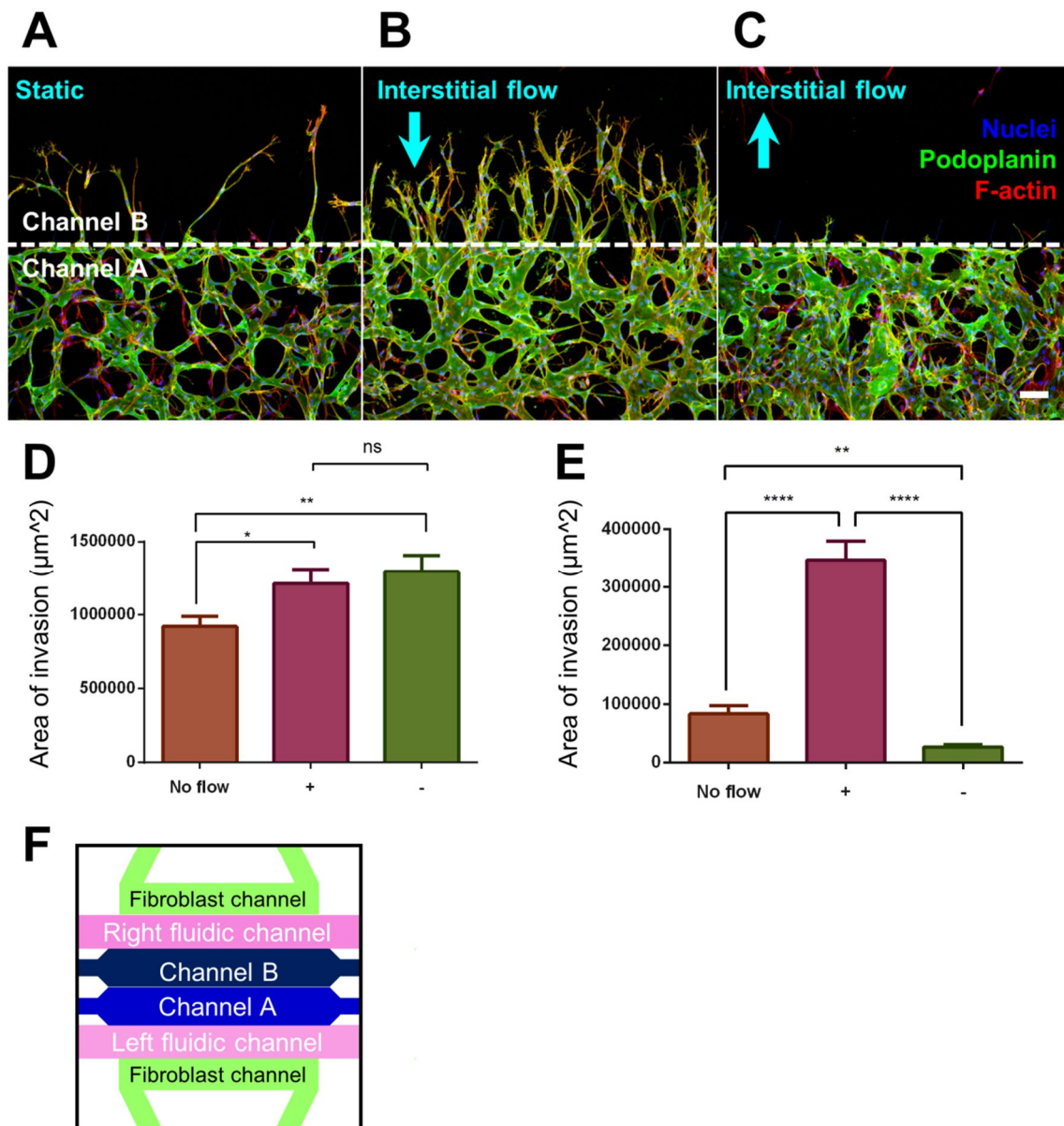
Day 2, Monoculture w/o stromal fibroblasts



**Fig 3.5** Comparison of presence and absence of co-culturing stromal fibroblasts. Scale bar, 100  $\mu\text{m}$ .

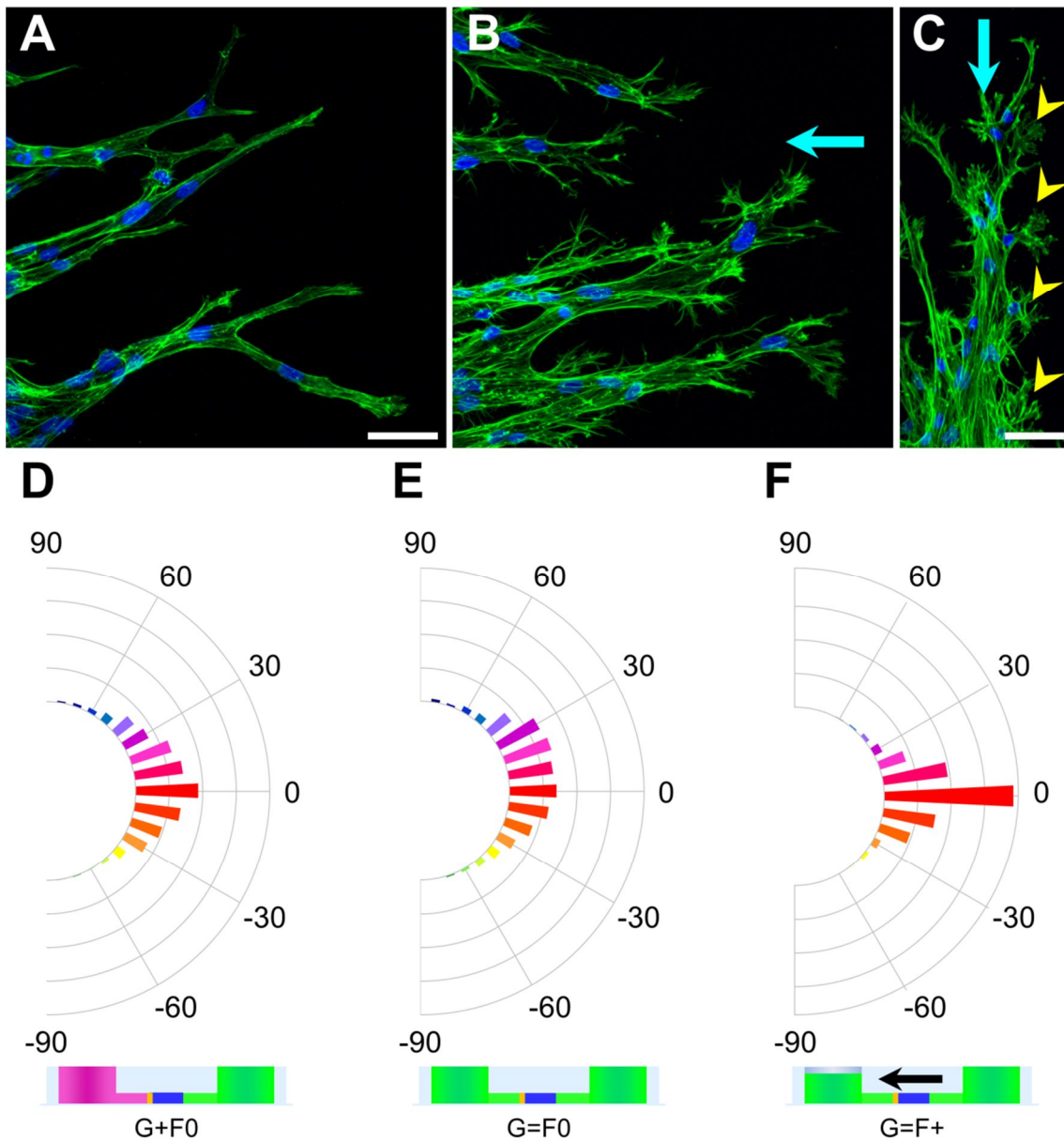


**Fig 3.6** Magnitude of interstitial flow modulates morphology of cellular protrusions and cellular invasion. (A) LECs tested with varying magnitudes of interstitial flow for 6 and 12 h. Insets display enlarged image of protrusions. Scale bar, 100  $\mu\text{m}$  (20  $\mu\text{m}$  for insets). (B) Quantification of the length of protrusions and (C) Quantification of cell nuclei invaded into fibrin matrix. Error bars represent SEM. For quantifications, at least 3 chips ( $\sim 200$  cellular protrusions and 9 apertures) per each condition were analyzed.



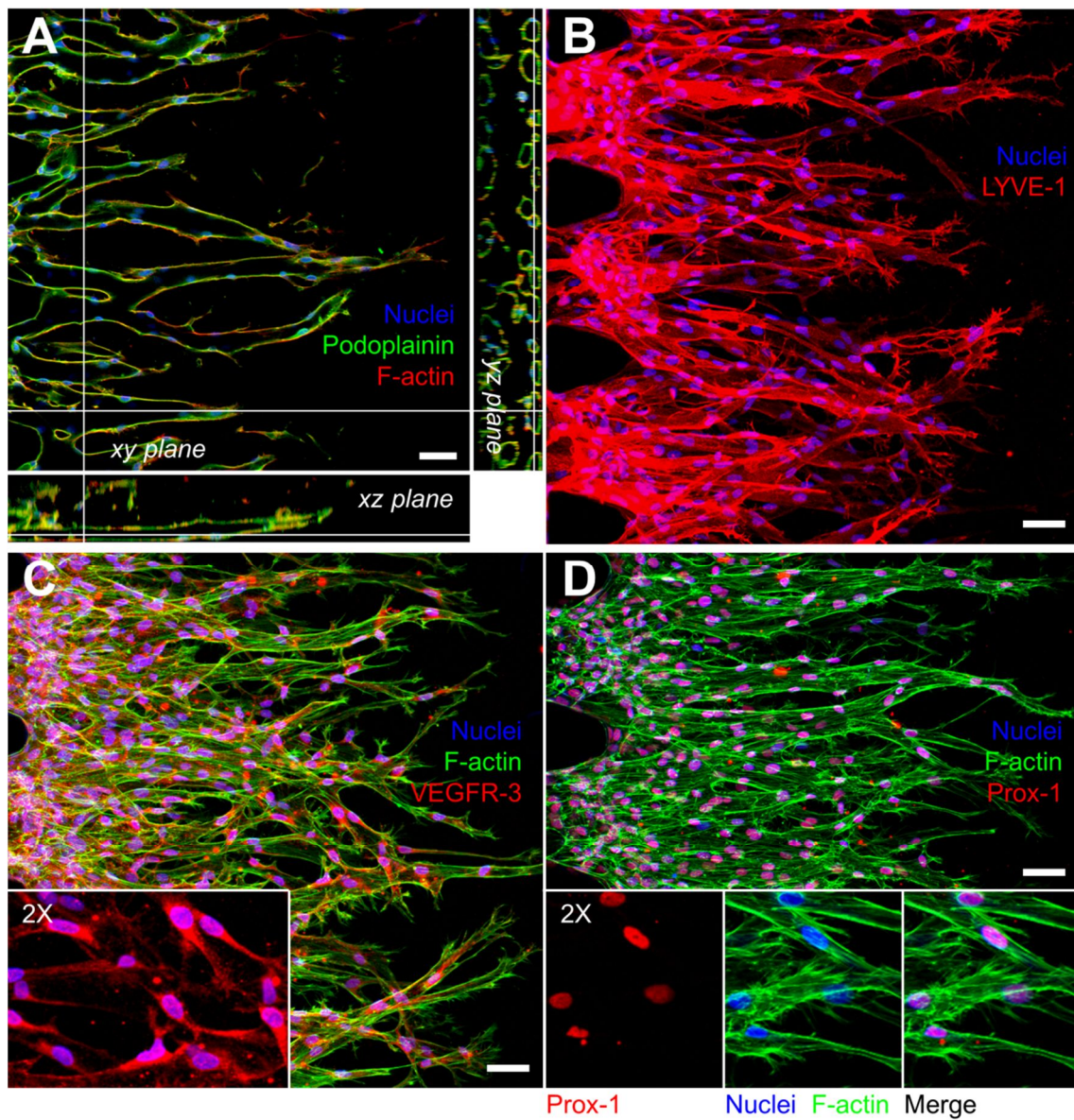
**Fig 3.7** Interstitial flow regulates lymphatic capillary network formation and directional expansion of network. (A-C) images showing lymphatic network formation at channel A and subsequent expansion into the adjacent acellular fibrin matrix in channel B in the presence of pro-lymphangiogenic factors and either static (A) or different flow conditions with direction indicated with arrows (B, C). Presence of interstitial flow, regardless of the direction, significantly enhanced organization of LECs into the interconnected capillary networks in the channel A as quantified in the graph (D). In the

static condition, LECs moderately migrated into the channel B, while the migration can be either greatly enhanced or largely suppressed depending on the presence and direction of interstitial flow as quantified in the graph (E). n = 6 chips per condition. \*P < 0.05, \*\*P < 0.005, \*\*\*P < 0.0005. (F) A schematic of the chip having two central channels, allowing investigation of interstitial flow-driven lymphatic capillary network formation and expansion. Scale bar, 100  $\mu$ m.

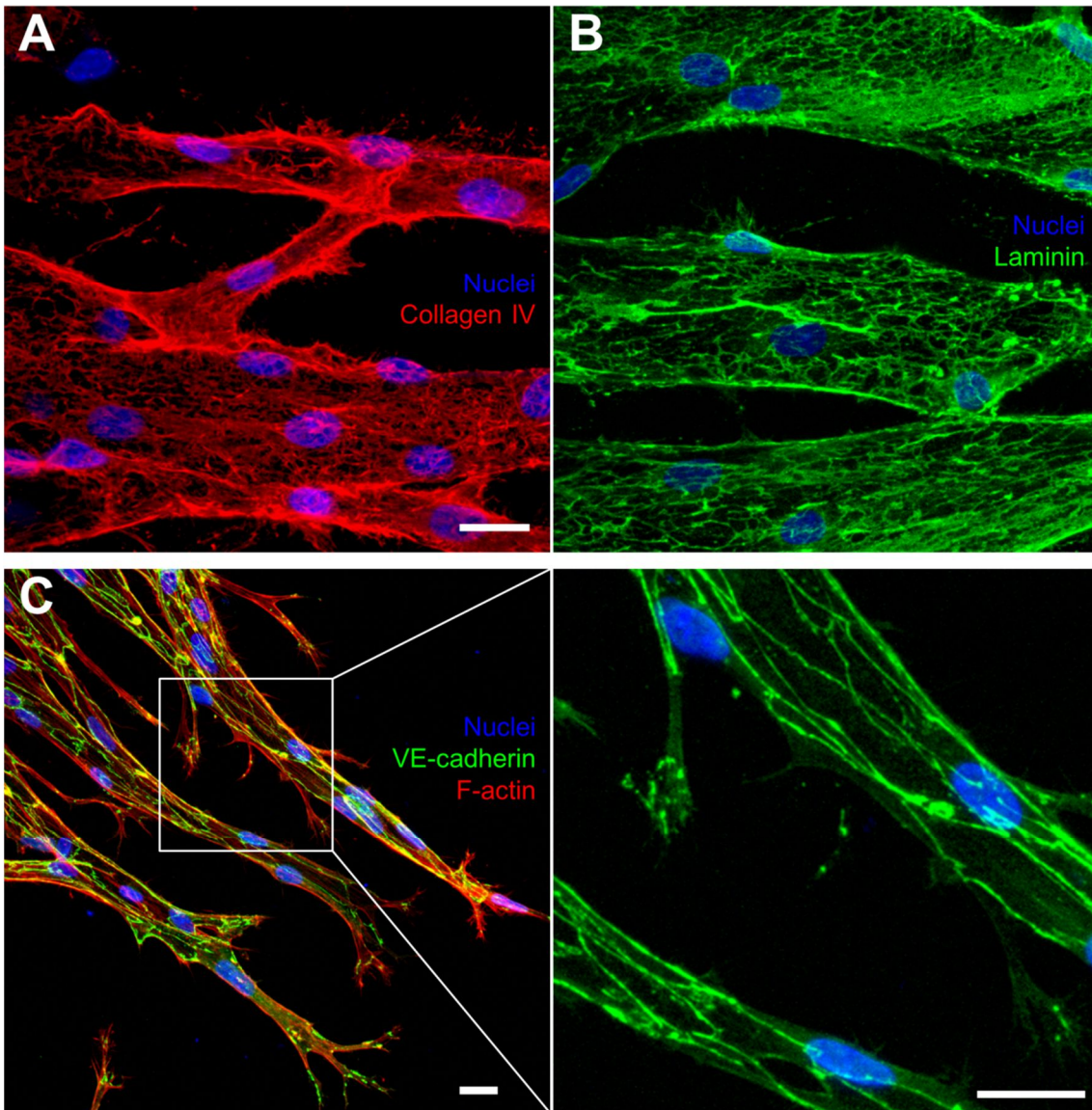


**Fig 3.8** Interstitial flow regulates filopodia formation and directional alignment of lymphatic sprouts. (A) Under static conditions (G+F0 and G=F0), the lymphatic sprouts exhibited relatively smooth outlines with rare filopodia projections. (B) In the presence of interstitial flow (G=F+), numerous filopodia protrusions were observed at the LECs of distal tip positions as well as behind following positions, with marked difference with static condition. (C) A representative of characteristic morphological figure of lymphatic

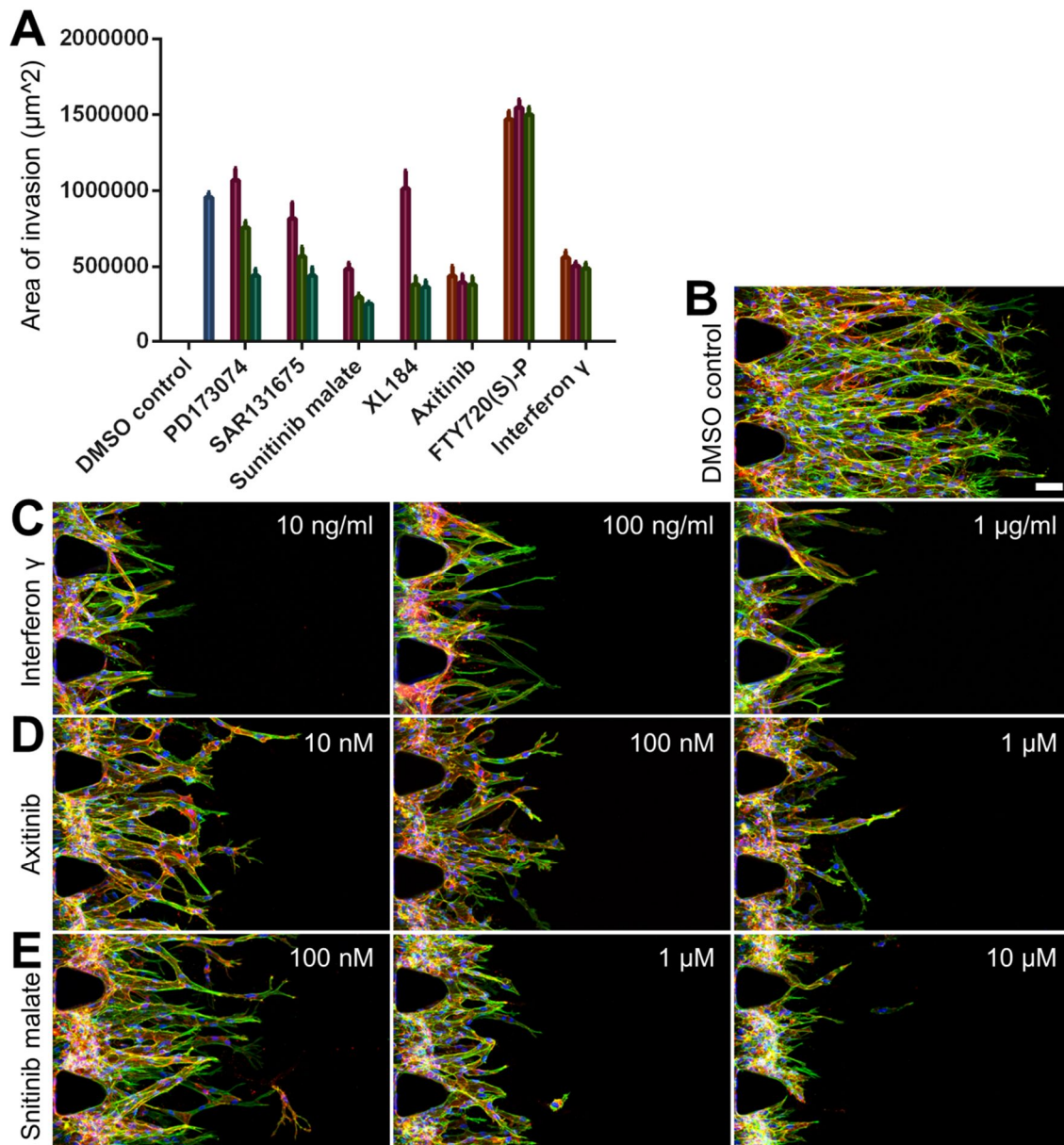
sprouts under combined stimulations (G=F+), displaying numerous filopodia protrusions along the entire length of sprouts as indicated with yellow arrowheads. (D-F) Semicircular polar histograms demonstrating distribution of angles of lymphatic sprouts relative to the horizontal axis. At least 9 chips per condition were analyzed. Length of each bar indicates percentage of sprouts aligned to the corresponding angle; (D, E) Lymphatic sprouts formed under G+F0 condition displayed relatively narrower distribution compared to the lymphatic sprouts formed G=F0 condition. (F) In the presence of interstitial flow, lymphatic sprouts were well-aligned along the streamline of flow. Scale bars, 50  $\mu\text{m}$ .



**Fig 3.9** Patency of hollow lumens and lymphatic-specific marker expression. (A) Confocal sections of lymphatic sprouts showing continuous and hollow lumens enclosed by LECs. (B-D) Expression of lymphatic specific markers confirmed via immunofluorescence analysis against LYVE-1 (B), VEGFR-3 (C) and Prox-1 (D). Scale bars, 50  $\mu$ m.



**Fig 3.10** Immunofluorescent images for characteristic basement membrane and adherens junction expression. A part of lymphatic sprouts stained against collagen IV (A) and laminin (B) confirm presence of perforated, discontinuous basement membrane around the lymphatic vessels. (C) Growing lymphatic sprouts display “zipper-like” VE-cadherin pattern. Scale bars, 20  $\mu\text{m}$



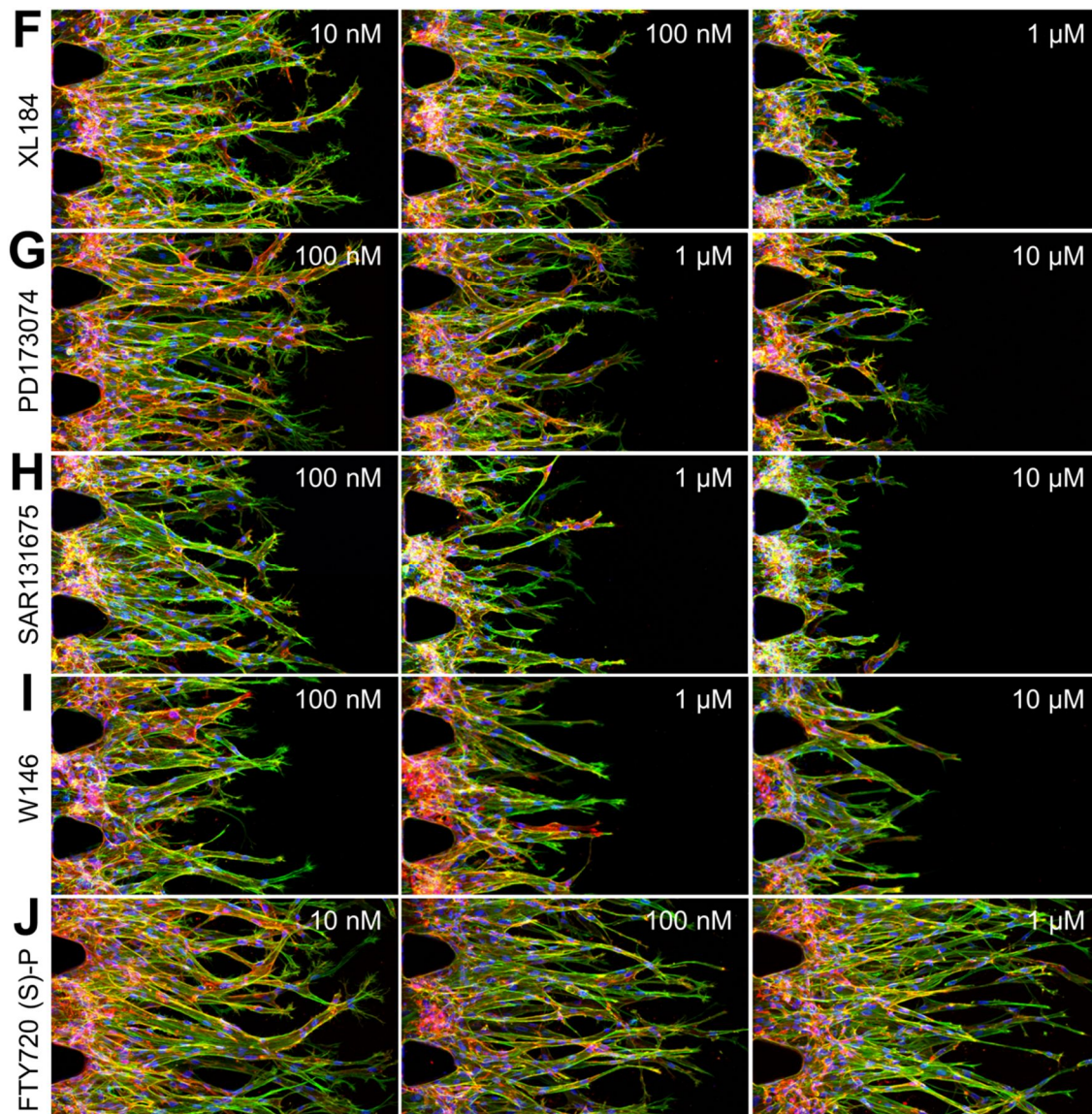


**Fig 3.11** Lymphatic sprouts grown with small molecule inhibitors. (A) Quantification of invasion area of lymphatic sprouts.  $n = 9$  chips per each dose of small molecule inhibitor. (B-J) Representative images of lymphatic sprouts showing dose-dependent inhibition of lymphatic sprout growth. Scale bars,  $50 \mu\text{m}$ .

## Chapter 4.

### Conclusions

In this thesis, novel and versatile *in vitro* model of blood/lymphatic vessels is presented. The model presented is built upon the microfluidics and microfabrication technologies, which enable optimization of the assay to be suited for *in vivo*-like morphogenesis of blood and lymphatic endothelial cells with simple experimental procedures. In this model, we successfully combined four key elements imperative for endothelial morphogenesis, which include cell-ECM interactions, EC-stromal cell type interactions, biochemical and mechanical stimuli in a single *in vitro* platform. Rather than simple addition of relevant components in one place, we considered spatiotemporal regulation and properties of each factors involved, providing appropriate stimulants and signals to endothelial cells that allowed close reconstitution of cascade of events observed during *in vivo* blood/lymphatic vessel morphogenesis.

In Chapter 2, we used the microfluidic platform to engineering functional, perfusable microvascular networks in 3D ECM. Close paracrine communication between endothelial cells and stromal fibroblasts activated endothelial cells to undergo natural cellular programs found during normal development and angiogenesis, forming perfusable networks of intact 3D microvessels. A major attribute of our chip was that it allows formation of readily perfusable vascular networks through *in vivo*-like morphogenesis processes, without needs of artificial structural templates that predefine the outlines of vasculatures. Therefore, the resulting microvessels possess the characteristic morphological and biochemical markers of *in vivo* blood vessels, and

exhibit strong barrier function, long-term stability, and flow-regulated cytoskeleton organization and nitric oxide synthesis.

In Chapter 3, we further expanded the utility of our chip by demonstrating sprouting morphogenesis of lymphatic endothelial cells. With capability of flexible and precise configuration of cellular microenvironments, we investigated how combinatorial stimulation of pro-lymphangiogenic factors and interstitial flow affects extents and phenotypes of lymphatic sprouting. In a combined stimulation of pro-lymphangiogenic factors and interstitial flow with direction reminiscent of lymphatic drainage, lymphatic endothelial cells showed active migration into the fibrin matrix in a manner of forming multicellular sprout-like structures. These sprouts also exhibited close resemblance with *in vivo* lymphatic capillaries, including expression of lymphatic specific biochemical markers, VEGFR-3, LYVE-1, Prox-1 and podoplanin, discontinuous basement membrane and numerous filopodia protrusions. Reproducible and robust attributes of our chip as an assay made it as a useful drug testing platform as we demonstrated by dose-dependent inhibition of lymphatic sprouting treated with pharmacological inhibitors of cell-surface receptors.

Taken together, we developed a microfluidic-based assay that closely reconstitutes morphogenesis processes and characteristic function of blood vessels as well as lymphatic sprouting *in vitro*. With continued improvements, we anticipate that this multifunctional, physiologically relevant model would replace conventional cell culture systems in pharmaceutical industry as they provide highly precise prediction of cellular behaviors and responses toward pharmacological administrations while reducing costs and labors required.

## References

1. Adams, R.H. and K. Alitalo, *Molecular regulation of angiogenesis and lymphangiogenesis*. Nature Reviews Molecular Cell Biology, 2007. **8**(6): p. 464-478.
2. Carmeliet, P. and R.K. Jain, *Angiogenesis in cancer and other diseases*. NATURE-LONDON-, 2000: p. 249-257.
3. Alitalo, K., T. Tammela, and T.V. Petrova, *Lymphangiogenesis in development and human disease*. Nature, 2005. **438**(7070): p. 946-953.
4. Auerbach, R., et al., *Angiogenesis assays: a critical overview*. Clinical chemistry, 2003. **49**(1): p. 32-40.
5. Bruyère, F. and A. Noël, *Lymphangiogenesis: in vitro and in vivo models*. The FASEB Journal, 2010. **24**(1): p. 8-21.
6. Kim, S., H.J. Kim, and N.L. Jeon, *Biological applications of microfluidic gradient devices*. Integrative Biology, 2010. **2**(11-12): p. 584-603.
7. Beebe, D.J., G.A. Mensing, and G.M. Walker, *Physics and applications of microfluidics in biology*. Annual review of biomedical engineering, 2002. **4**(1): p. 261-286.
8. Huh, D., G.A. Hamilton, and D.E. Ingber, *From 3D cell culture to organs-on-chips*. Trends in cell biology, 2011. **21**(12): p. 745-754.
9. Huh, D., et al., *Reconstituting organ-level lung functions on a chip*. Science, 2010. **328**(5986): p. 1662.
10. Kim, H.J., et al., *Human gut-on-a-chip inhabited by microbial flora that experiences intestinal peristalsis-like motions and flow*. Lab on a Chip, 2012.

- 12(12): p. 2165-2174.
11. Jang, K.-J. and K.-Y. Suh, *A multi-layer microfluidic device for efficient culture and analysis of renal tubular cells*. Lab on a Chip, 2010. **10**(1): p. 36-42.
  12. Zheng, Y., et al., *In vitro microvessels for the study of angiogenesis and thrombosis*. Proceedings of the National Academy of Sciences, 2012. **109**(24): p. 9342-9347.
  13. Vickerman, V., et al., *Design, fabrication and implementation of a novel multi-parameter control microfluidic platform for three-dimensional cell culture and real-time imaging*. Lab Chip, 2008. **8**(9): p. 1468-1477.
  14. Song, J.W., D. Bazou, and L. Munn, *Anastomosis of endothelial sprouts forms new vessels in a tissue analogue of angiogenesis*. Integrative Biology, 2012.
  15. Bischel, L.L., et al., *Tubeless microfluidic angiogenesis assay with three-dimensional endothelial-lined microvessels*. Biomaterials, 2012.
  16. Wong, K.H., et al., *Microfluidic models of vascular functions*. Annual review of biomedical engineering, 2012. **14**: p. 205-230.
  17. Carmeliet, P. and R.K. Jain, *Principles and mechanisms of vessel normalization for cancer and other angiogenic diseases*. Nature Reviews Drug Discovery, 2011. **10**(6): p. 417-427.
  18. Gavard, J. and J.S. Gutkind, *VEGF controls endothelial-cell permeability by promoting the  $\beta$ -arrestin-dependent endocytosis of VE-cadherin*. Nature cell biology, 2006. **8**(11): p. 1223-1234.
  19. Tzima, E., et al., *A mechanosensory complex that mediates the endothelial cell response to fluid shear stress*. Nature, 2005. **437**(7057): p. 426-431.

20. Carman, C.V. and T.A. Springer, *A transmigratory cup in leukocyte diapedesis both through individual vascular endothelial cells and between them*. The Journal of cell biology, 2004. **167**(2): p. 377-388.
21. Tremblay, P.L., J. Huot, and F.A. Auger, *Mechanisms by which E-selectin regulates diapedesis of colon cancer cells under flow conditions*. Cancer research, 2008. **68**(13): p. 5167.
22. Ingber, D.E., *Mechanical signaling and the cellular response to extracellular matrix in angiogenesis and cardiovascular physiology*. Circulation research, 2002. **91**(10): p. 877-887.
23. Raines, E.W., *The extracellular matrix can regulate vascular cell migration, proliferation, and survival: relationships to vascular disease*. International journal of experimental pathology, 2000. **81**(3): p. 173-182.
24. Ingber, D.E. and J. Folkman, *How does extracellular matrix control capillary morphogenesis?* Cell, 1989. **58**(5): p. 803-805.
25. Stupack, D.G. and D.A. Cheresh, *ECM remodeling regulates angiogenesis: endothelial integrins look for new ligands*. Science Signalling, 2002. **2002**(119): p. pe7.
26. Chrobak, K.M., D.R. Potter, and J. Tien, *Formation of perfused, functional microvascular tubes in vitro*. Microvascular research, 2006. **71**(3): p. 185-196.
27. Chung, S., et al., *Cell migration into scaffolds under co-culture conditions in a microfluidic platform*. Lab chip, 2008. **9**(2): p. 269-275.
28. Price, G.M., et al., *Effect of mechanical factors on the function of engineered human blood microvessels in microfluidic collagen gels*. Biomaterials, 2010.

- 31(24): p. 6182-6189.
29. Song, J.W. and L.L. Munn, *Fluid forces control endothelial sprouting*. Proceedings of the National Academy of Sciences, 2011. **108**(37): p. 15342-15347.
  30. Zervantonakis, I.K., et al., *Three-dimensional microfluidic model for tumor cell intravasation and endothelial barrier function*. Proceedings of the National Academy of Sciences, 2012. **109**(34): p. 13515-13520.
  31. Yeon JH, R.H., Chung M, Hu QP, Jeon NL., *In vitro formation and characterization of a perfusable three-dimensional tubular capillary network in microfluidic devices*. Lab on a Chip, 2012.
  32. Cuchiara, M.P., et al., *Integration of Self-Assembled Microvascular Networks with Microfabricated PEG-Based Hydrogels*. Advanced Functional Materials, 2012.
  33. Carrion, B., et al., *Recreating the perivascular niche ex vivo using a microfluidic approach*. Biotechnology and bioengineering.
  34. Chan, J.M., et al., *Engineering of In Vitro 3D Capillary Beds by Self-Directed Angiogenic Sprouting*. PloS one, 2012. **7**(12): p. e50582.
  35. Newman, A.C., et al., *The requirement for fibroblasts in angiogenesis: fibroblast-derived matrix proteins are essential for endothelial cell lumen formation*. Molecular Biology of the Cell, 2011. **22**(20): p. 3791-3800.
  36. Zhou, X., et al., *Peptide-Induced Inflammatory Increase in Vascular Permeability Improves Photosensitizer Delivery and Intersubject Photodynamic Treatment Efficacy*. 2009.

37. Huang, C.P., et al., *Engineering microscale cellular niches for three-dimensional multicellular co-cultures*. Lab chip, 2009. **9**(12): p. 1740-1748.
38. Nakatsu, M.N., et al., *Angiogenic sprouting and capillary lumen formation modeled by human umbilical vein endothelial cells (HUVEC) in fibrin gels: the role of fibroblasts and Angiopoietin-1*. Microvascular research, 2003. **66**(2): p. 102-112.
39. Chen, X., et al., *Prevascularization of a fibrin-based tissue construct accelerates the formation of functional anastomosis with host vasculature*. Tissue Engineering Part A, 2008. **15**(6): p. 1363-1371.
40. Dvorak, H., et al., *Fibrin containing gels induce angiogenesis. Implications for tumor stroma generation and wound healing*. Laboratory investigation; a journal of technical methods and pathology, 1987. **57**(6): p. 673.
41. Gerhardt, H., et al., *VEGF guides angiogenic sprouting utilizing endothelial tip cell filopodia*. The Journal of cell biology, 2003. **161**(6): p. 1163.
42. He, P. and R. Adamson, *Visualization of endothelial clefts and nuclei in living microvessels with combined reflectance and fluorescence confocal microscopy*. Microcirculation, 1995. **2**(3): p. 267-276.
43. Davis, G.E. and D.R. Senger, *Endothelial extracellular matrix biosynthesis, remodeling, and functions during vascular morphogenesis and neovessel stabilization*. Circulation Research, 2005. **97**(11): p. 1093-1107.
44. Yuan, W., et al., *Non-invasive measurement of solute permeability in cerebral microvessels of the rat*. Microvascular research, 2009. **77**(2): p. 166-173.
45. Vickerman, V. and R. Kamm, *Mechanism of a flow-gated angiogenesis switch:*

- Early signaling events at cell-matrix and cell-cell junctions*. Integrative Biology, 2012.
46. Lipowsky, H.H., *Microvascular rheology and hemodynamics*. Microcirculation, 2005. **12**(1): p. 5-15.
  47. Hahn, C. and M.A. Schwartz, *Mechanotransduction in vascular physiology and atherogenesis*. Nature Reviews Molecular Cell Biology, 2009. **10**(1): p. 53-62.
  48. Sheikh, S., et al., *Exposure to fluid shear stress modulates the ability of endothelial cells to recruit neutrophils in response to tumor necrosis factor- $\alpha$ : a basis for local variations in vascular sensitivity to inflammation*. Blood, 2003. **102**(8): p. 2828-2834.
  49. Dimmeler, S., et al., *Activation of nitric oxide synthase in endothelial cells by Akt-dependent phosphorylation*. Nature, 1999. **399**(6736): p. 601-605.
  50. Pacher, P., J.S. Beckman, and L. Liaudet, *Nitric oxide and peroxynitrite in health and disease*. Physiological reviews, 2007. **87**(1): p. 315-424.
  51. Joshi, M.S., et al., *Receptor-mediated activation of nitric oxide synthesis by arginine in endothelial cells*. Proceedings of the National Academy of Sciences, 2007. **104**(24): p. 9982.
  52. Armulik, A., A. Abramsson, and C. Betsholtz, *Endothelial/pericyte interactions*. Circulation research, 2005. **97**(6): p. 512-523.
  53. Kerbel, R.S., *Tumor angiogenesis*. New England Journal of Medicine, 2008. **358**(19): p. 2039-2049.
  54. Abbott, N.J., L. Rönnbäck, and E. Hansson, *Astrocyte–endothelial interactions at the blood–brain barrier*. Nature Reviews Neuroscience, 2006. **7**(1): p. 41-53.

55. Papetti, M. and I.M. Herman, *Mechanisms of normal and tumor-derived angiogenesis*. American Journal of Physiology-Cell Physiology, 2002. **282**(5): p. C947-C970.
56. Carlos, T.M. and J.M. Harlan, *Leukocyte-endothelial adhesion molecules*. Blood, 1994. **84**(7): p. 2068-2101.
57. Alajati, A., et al., *Spheroid-based engineering of a human vasculature in mice*. Nature methods, 2008. **5**(5): p. 439-445.
58. Dekker, R.J., et al., *KLF2 provokes a gene expression pattern that establishes functional quiescent differentiation of the endothelium*. Blood, 2006. **107**(11): p. 4354-4363.
59. Chien, S., *Mechanotransduction and endothelial cell homeostasis: the wisdom of the cell*. American Journal of Physiology-Heart and Circulatory Physiology, 2007. **292**(3): p. H1209-H1224.
60. Galbraith, C., R. Skalak, and S. Chien, *Shear stress induces spatial reorganization of the endothelial cell cytoskeleton*. Cell motility and the cytoskeleton, 1998. **40**(4): p. 317-330.
61. Miller, J.S., et al., *Rapid casting of patterned vascular networks for perfusable engineered three-dimensional tissues*. Nature Materials, 2012.
62. Kim, S., et al., *Engineering of functional, perfusable 3D microvascular networks on a chip*. Lab Chip, 2013. **13**(8): p. 1489-1500.
63. Jeon, J.S., et al., *In Vitro Model of Tumor Cell Extravasation*. PloS one, 2013. **8**(2): p. e56910.
64. Kaipainen, A., et al., *Expression of the fms-like tyrosine kinase 4 gene becomes*

- restricted to lymphatic endothelium during development.* Proceedings of the National Academy of Sciences, 1995. **92**(8): p. 3566-3570.
65. Banerji, S., et al., *LYVE-1, a new homologue of the CD44 glycoprotein, is a lymph-specific receptor for hyaluronan.* The Journal of cell biology, 1999. **144**(4): p. 789-801.
66. Skobe, M., et al., *Induction of tumor lymphangiogenesis by VEGF-C promotes breast cancer metastasis.* Nature medicine, 2001. **7**(2): p. 192-198.
67. Stacker, S.A., et al., *VEGF-D promotes the metastatic spread of tumor cells via the lymphatics.* Nature medicine, 2001. **7**(2): p. 186-191.
68. Björndahl, M.A., et al., *Vascular endothelial growth factor-a promotes peritumoral lymphangiogenesis and lymphatic metastasis.* Cancer research, 2005. **65**(20): p. 9261-9268.
69. Cao, R., et al., *Mouse corneal lymphangiogenesis model.* Nature protocols, 2011. **6**(6): p. 817-826.
70. Bruyère, F., et al., *Modeling lymphangiogenesis in a three-dimensional culture system.* Nature methods, 2008. **5**(5): p. 431-437.
71. Schulz, M.M.P., et al., *Phenotype-based high-content chemical library screening identifies statins as inhibitors of in vivo lymphangiogenesis.* Proceedings of the National Academy of Sciences, 2012. **109**(40): p. E2665-E2674.
72. Helm, C.-L.E., et al., *Synergy between interstitial flow and VEGF directs capillary morphogenesis in vitro through a gradient amplification mechanism.* Proceedings of the National Academy of Sciences of the United States of America, 2005. **102**(44): p. 15779-15784.

73. Rutkowski, J.M., K.C. Boardman, and M.A. Swartz, *Characterization of lymphangiogenesis in a model of adult skin regeneration*. American Journal of Physiology-Heart and Circulatory Physiology, 2006. **291**(3): p. H1402-H1410.
74. Shin, J.W., R. Huggenberger, and M. Detmar, *Transcriptional profiling of VEGF-A and VEGF-C target genes in lymphatic endothelium reveals endothelial-specific molecule-1 as a novel mediator of lymphangiogenesis*. Blood, 2008. **112**(6): p. 2318-2326.
75. Wiig, H. and M.A. Swartz, *Interstitial fluid and lymph formation and transport: physiological regulation and roles in inflammation and cancer*. Physiological Reviews, 2012. **92**(3): p. 1005-1060.
76. Bonvin, C., et al., *A multichamber fluidic device for 3D cultures under interstitial flow with live imaging: development, characterization, and applications*. Biotechnology and bioengineering, 2010. **105**(5): p. 982-991.
77. Mäkinen, T., et al., *Isolated lymphatic endothelial cells transduce growth, survival and migratory signals via the VEGF-C/D receptor VEGFR-3*. The EMBO journal, 2001. **20**(17): p. 4762-4773.
78. Podgrabinska, S., et al., *Molecular characterization of lymphatic endothelial cells*. Proceedings of the National Academy of Sciences, 2002. **99**(25): p. 16069-16074.
79. Yoon, C.M., et al., *Sphingosine-1-phosphate promotes lymphangiogenesis by stimulating SIP1/Gi/PLC/Ca<sup>2+</sup> signaling pathways*. Blood, 2008. **112**(4): p. 1129-1138.
80. Karkkainen, M.J., et al., *Vascular endothelial growth factor C is required for*

- sprouting of the first lymphatic vessels from embryonic veins.* Nature immunology, 2003. **5**(1): p. 74-80.
81. Chang, L.K., et al., *Dose-dependent response of FGF-2 for lymphangiogenesis.* Proceedings of the National Academy of Sciences of the United States of America, 2004. **101**(32): p. 11658-11663.
82. Hirakawa, S., et al., *VEGF-A induces tumor and sentinel lymph node lymphangiogenesis and promotes lymphatic metastasis.* The Journal of experimental medicine, 2005. **201**(7): p. 1089-1099.
83. Kajiyama, K., et al., *Hepatocyte growth factor promotes lymphatic vessel formation and function.* The EMBO journal, 2005. **24**(16): p. 2885-2895.
84. Björndahl, M., et al., *Insulin-like growth factors 1 and 2 induce lymphangiogenesis in vivo.* Proceedings of the National Academy of Sciences of the United States of America, 2005. **102**(43): p. 15593-15598.
85. Cao, R., et al., *PDGF-BB induces intratumoral lymphangiogenesis and promotes lymphatic metastasis.* Cancer cell, 2004. **6**(4): p. 333-345.
86. Gudi, S.R., C.B. Clark, and J.A. Frangos, *Fluid Flow Rapidly Activates G Proteins in Human Endothelial Cells Involvement of G Proteins in Mechanochemical Signal Transduction.* Circulation Research, 1996. **79**(4): p. 834-839.
87. Wojciak-Stothard, B. and A.J. Ridley, *Shear stress-induced endothelial cell polarization is mediated by Rho and Rac but not Cdc42 or PI 3-kinases.* The Journal of cell biology, 2003. **161**(2): p. 429-439.
88. Jin, Z.-G., et al., *Ligand-independent activation of vascular endothelial growth*

- factor receptor 2 by fluid shear stress regulates activation of endothelial nitric oxide synthase.* Circulation research, 2003. **93**(4): p. 354-363.
89. Jung, B., et al., *Flow-regulated endothelial SIP receptor-1 signaling sustains vascular development.* Developmental cell, 2012. **23**(3): p. 600-610.
90. Baluk, P., et al., *Functionally specialized junctions between endothelial cells of lymphatic vessels.* The Journal of experimental medicine, 2007. **204**(10): p. 2349-2362.
91. Dekker, R.J., et al., *Prolonged fluid shear stress induces a distinct set of endothelial cell genes, most specifically lung Krüppel-like factor (KLF2).* Blood, 2002. **100**(5): p. 1689-1698.
92. Tzima, E., et al., *Activation of integrins in endothelial cells by fluid shear stress mediates Rho-dependent cytoskeletal alignment.* The EMBO journal, 2001. **20**(17): p. 4639-4647.
93. Shyy, J.Y.-J. and S. Chien, *Role of integrins in endothelial mechanosensing of shear stress.* Circulation research, 2002. **91**(9): p. 769-775.
94. Nilius, B. and G. Droogmans, *Ion channels and their functional role in vascular endothelium.* Physiological Reviews, 2001. **81**(4): p. 1415-1459.
95. Weinbaum, S., et al., *Mechanotransduction and flow across the endothelial glycocalyx.* Proceedings of the National Academy of Sciences, 2003. **100**(13): p. 7988-7995.
96. Chachisvilis, M., Y.-L. Zhang, and J.A. Frangos, *G protein-coupled receptors sense fluid shear stress in endothelial cells.* Proceedings of the National Academy of Sciences, 2006. **103**(42): p. 15463-15468.

97. Planas-Paz, L. and E. Lammert, *Mechanical forces in lymphatic vascular development and disease*. Cellular and Molecular Life Sciences, 2013: p. 1-14.
98. Nguyen, D.-H.T., et al., *Biomimetic model to reconstitute angiogenic sprouting morphogenesis in vitro*. Proceedings of the National Academy of Sciences, 2013. **110**(17): p. 6712-6717.
99. Chung, S., et al., *Microfluidic platforms for studies of angiogenesis, cell migration, and cell–cell interactions*. Annals of biomedical engineering, 2010. **38**(3): p. 1164-1177.
100. Shao, J., et al., *Integrated microfluidic chip for endothelial cells culture and analysis exposed to a pulsatile and oscillatory shear stress*. Lab on a Chip, 2009. **9**(21): p. 3118-3125.
101. Heldin, C.-H., et al., *High interstitial fluid pressure—an obstacle in cancer therapy*. Nature Reviews Cancer, 2004. **4**(10): p. 806-813.
102. Shields, J.D., et al., *Autologous chemotaxis as a mechanism of tumor cell homing to lymphatics via interstitial flow and autocrine CCR7 signaling*. Cancer cell, 2007. **11**(6): p. 526-538.
103. Haessler, U., et al., *Migration dynamics of breast cancer cells in a tunable 3D interstitial flow chamber*. Integrative Biology, 2012. **4**(4): p. 401-409.
104. Lara Planas-Paz, B.S., et al., *Mechanoinduction of lymph vessel expansion*. The EMBO journal, 2011. **31**(4): p. 788-804.
105. Boardman, K.C. and M.A. Swartz, *Interstitial flow as a guide for lymphangiogenesis*. Circulation research, 2003. **92**(7): p. 801-808.
106. Polacheck, W.J., J.L. Charest, and R.D. Kamm, *Interstitial flow influences*

- direction of tumor cell migration through competing mechanisms*. Proceedings of the National Academy of Sciences, 2011. **108**(27): p. 11115-11120.
107. Miteva, D.O., et al., *Transmural flow modulates cell and fluid transport functions of lymphatic endothelium*. Circulation research, 2010. **106**(5): p. 920-931.
108. Lin, J., et al., *Inhibition of lymphogenous metastasis using adeno-associated virus-mediated gene transfer of a soluble VEGFR-3 decoy receptor*. Cancer research, 2005. **65**(15): p. 6901-6909.
109. Hellström, M., et al., *Dll4 signalling through Notch1 regulates formation of tip cells during angiogenesis*. Nature, 2007. **445**(7129): p. 776-780.
110. Phng, L.-K. and H. Gerhardt, *Angiogenesis: a team effort coordinated by notch*. Developmental cell, 2009. **16**(2): p. 196-208.

## 국문 초록

암의 성장과 전이, 당뇨 망막병증, 노인성 황반변성 등 70여종 이상의 다양한 질병은 혈관 혹은 림프관의 비정상적 성장 및 기능에 의해 유발 혹은 악화된다. 따라서 혈관 및 림프관의 형성과 기능을 조절함으로써 이러한 질병을 극복하고자 하는 노력이 의학분야 전반에 걸쳐 활발히 이루어지고 있다. 혈관의 형성과 기능에 관련된 기초 의학 연구와 신약의 효과 평가에는 필연적으로 세포배양을 통한 체외 모델을 필요로 한다. 내피세포의 미세환경은 3차원 세포외기질(extracellular matrix), 다양한 세포군 사이의 상호작용, 혈류 및 혈장의 유동에 의한 생물리적 자극 등 복합적인 인자들의 결합으로 이루어져 있다. 이러한 인자들은 혈관의 형성 과정에서 복합적인 영향을 미칠 뿐 아니라 형성된 혈관의 기능과 항상성 유지에 있어서도 중요한 역할을 수행한다. 기존의 혈관모델에서는 이러한 인자들이 부분적으로 결여되어 있거나 정밀 제어되지 못하는 취약점을 지녀, 이를 통해 관찰된 세포반응이 생체현상을 이해하는데 제한적인 정보만을 제공한다는 한계를 가진다. 본 연구에서 제안하는 미세소자(microdevice)는 혈관의 형성과 기능에 관련된 주요 인자들, 다양한 세포군 사이의 상호 신호전달, 세포-세포외기질 상호작용, 그리고 혈관 고유의 생화학, 생물리적 신호분자를 3차원 배양환경에서 결합하여 체내에서 관찰되는 혈관 형성의 단계적인 과정을 높은 유사성을 통해 구현하였다. 특히 혈관내피세포와 섬유아세포의 공간적인 배치와 배양 형태를 제어함으로써 배아의 발생 단계에서 관찰되는 혈관형성 과정(vasculogenesis)와 기존 혈관에서 생혈관이 성장하는 과정(angiogenesis)이 정밀 모사하였다. 또한 이러한 과정을 통해 형성되는 혈관망은 성장의 최종 단계에서 자발적으로 혈관 내부로의 접근을 가능토록 하는 입, 출구를 형성하도록 유도됨으로써 3차원 체외 혈관에서도 혈류 유동을 모사할 수 있는 실험적 기법을 제공, 기존 기술의 한계점을 극복하였다. 이 방법은 3차원 세포배양, 생리적인 혈관의 성장, 혈관 특이적인 미세 환경의 정밀 모사, 혈류 유동을 통한 혈관 기능의 발현이라는 기술적 과제들을 하나의 모델에서 통합적으로 구축함으로써 기존의 방식에 비해 높은 생체 유사성과 신뢰성을 지닌 혈관 모델을 제안하였다.

또한 혈관의 신생과 형태적으로 유사한 성장 과정을 보여주는 림프관 신생의 연구를 통해 개발된 모델 시스템의 활용 범위를 확대하였다. 림프관의 신생은 암의 전이 과정에서 관찰되는 주요 세포거동이며 염증반응이나 자가면역질환 등 다양한 병리적 현상에서 주요한 단계에 해당한다. 본 연구에서 개발된 플랫폼은 성장인자와 조직액의 흐름(interstitial flow)이라는 두 가지 주요 자극을 결합적으로 세포에 전달함으로써 기존의 모델에 비해 높은 생체 유사성을 가능케 하였다. 미세유체소자 내에서 배양된 림프관 내피세포는 혈관성장인자(vascular endothelial growth factor, VEGF), 섬유아세포 성장인자(basic fibroblast growth factor, bFGF), 스피핑고신 1-인산(sphingosine 1-phosphate) 등의 다양한 생화학 분자들의 농도구배에 반응하여 림프관을 형성하였다. 하지만 여기에 유체의 유동에 의한 기계적인 자극을 동시에 인가했을 때 림프관의 성장에 통계적으로 유의미한 향상이 관찰되었으며, 유체 유동의 속도와 그 방향에도 민감한 세포거동의 차이를 나타냈다. 가장 높은 림프관의 성장이 관찰된 조건은 성장인자의 과발현과 높은 림프액 유동량이라는 암 주변 미세환경의 전형적인 특징과 일치하는 것으로 나타났다. 특히 이러한 조건에서 형성된 림프관은, 생체 내에서 관찰되는 림프관과 조직학적 표지, 형태학적 특징 등 다양한 면에서 유사성을 보였다. 또한 실험적으로 간편하면서도 높은 생체 유사성을 보이는 모델을 통해 다양한 약물에 따른 림프관 형성 양상을 관찰하고 이를 정량화 함으로써 본 연구에서 개발한 모델이 신약의 개발과정에서도 유용한 특성을 지님을 입증하였다.

본 연구는 3차원 세포배양, 생리적인 혈관과 림프관의 성장, 혈관의 특이적인 미세 환경의 정밀 모사, 혈류 유동을 통한 혈관 기능의 발현이라는 기술적 과제들을 하나의 모델에서 통합적으로 구축함으로써 기존의 방식에 비해 높은 생체 유사성과 신뢰성을 지닌 체외 모델을 제공하였다. 이러한 미세소자는 실험의 효율성, 재현성, 신뢰성 측면에서 장점을 지닌 미세소자의 병렬화를 통한 신약개발, 의약학과 세포생물학 분야의 기초연구를 대상으로 한 폭넓은 활용이 기대된다.

주요어: 혈관, 림프관, 혈관신생, 림프관신생, 내피세포, 유체전단응력,  
미세유체소자

학번: 2009-30161